Optical and γ-ray studies of pulsars with VERITAS

Samantha Wong, Department of Physics
McGill University, Montreal

August 15, 2023

A thesis submitted to McGill University in partial fulfillment of the requirements of the degree of

Master of Physics

"We're almost there & nowhere near it. All that matters is that we're going!"

- Gilmore Girls

Abstract

Though there are thousands of pulsars detected either in radio, X-ray, or GeV γ-rays (or a combination thereof), fewer than ten have been confirmed to pulse in optical wavelengths and only two at very high energy (VHE; > 100 GeV) γ-ray energies. Pulsar emission models are currently unable to explain X-ray and soft γ-ray emission, so optical and VHE γ-ray detections or limits are critical to constrain emission mechanisms at non-radio wavelengths. Furthermore, the environments surrounding pulsars, known as pulsar wind nebulae (PWNe) or TeV halos, are known to be sites of extreme particle acceleration within the Milky Way. VHE observations of PWNe/TeV halos can provide new insights into fundamental physics at energies that are unattainable by the particle accelerators on Earth. The Very Energetic Radiation Imaging Telescope Array System (VERITAS) is an array of four telescopes capable of both VHE γ-ray and rapid ($\approx$ millisecond) optical photometric observations. In this thesis, the VERITAS observations of the Crab nebula and pulsar, along with millisecond pulsar PSR B1937+21 will be presented. The analysis of these observations will be described, along with predictions as to which known pulsars may show optical pulsations that are visible to VERITAS' optical instrument. In VHE γ-rays, a statistically significant detection of the Crab nebula and the Crab pulsar interpulse are obtained, with strong evidence for the Crab pulsar main pulse. A statistically significanct detection of the Crab pulsar is also obtained in optical wavelengths. PSR B1937+21 is neither detected to pulse optically nor in VHE γ-rays, but insufficient observations were obtained to expect a detection in either wavelength. Several more pulsars are likely de-

tectable by VERITAS in optical wavelengths, and future observations will be requested to validate these predictions.

Abrégé

Bien qu'il y ait des milliers de pulsars détectés soit dans les rayons radio, les rayons X ou les rayons γ du GeV (ou une combinaison de ceux-ci), moins de dix ont été confirmés comme pulsant dans des longueurs d'onde optiques et seulement deux à très haute énergie (VHE; > 100 GeV) rayons γ. Les modèles d'émission de pulsars sont actuellement incapables d'expliquer l'émission de rayons X et de rayons γ, alor des détections ou limites optiques et VHE γ sont essentielles pour contraindre les mécanismes d'émission à des longueurs d'onde hors radio. De plus, les environnements entourant les pulsars, connus sous le nom de nébuleuses de vent de pulsar (PWNe) ou halos de TeV, sont connus pour être des sites d'accélération extrême des particules dans la Galaxie. Les observations VHE des PWNe/halos TeV peuvent fournir de nouvelles informations sur la physique fondamentale à des énergies inaccessibles aux accélérateurs de particules sur Terre. Le système VERITAS (Very Energetic Radiation Imaging Telescope Array System) est un ensemble de quatre télescopes capables d'observations photométriques et rapides ($\approx$ milliseconde) et de rayons γ VHE. Dans cette thèse, les observations VERITAS de la nébuleuse et du pulsar du Crabe, ainsi que du pulsar milliseconde PSR B1937+21 seront présentées. L'analyse de ces observations sera présentée, ainsi que des prédictions sur les pulsars connus qui peuvent montrer des pulsations optiques visibles par l'instrument optique de VERITAS. Dans les rayons γ VHE, une détection statistiquement significative de la nébuleuse du Crabe et de l'interpulse du pulsar du Crabe est obtenue, avec évidence pour l'impulsion principale du pulsar du Crabe. Une détection statistiquement significative du pulsar du Crabe est également obtenue dans les longueurs d'onde optiques. Le PSR B1937+21 n'est

pas détecté comme pulsant optiquement ni dans les rayons VHE γ, mais des observations insuffisantes ont été obtenues pour s'attendre à une détection dans chaque band d'onde. Plusieurs autres pulsars sont probablement détectables par VERITAS dans des longueurs d'onde optiques, et des observations futures seront demandées pour valider ces prédictions.

Acknowledgements

Firstly, I would like to thank my supervisor, Ken Ragan, for his support through this thesis and timeless support of this project. Though there were some hiccups during this project and many others, he helped me get to the end of this M.Sc., and I'm looking forward to continuing to work together for the next few years.

I would like to thank the VERITAS group at McGill for helping me throughout the course of this project and for teaching me so much about VERITAS and γ-ray astrophysics. In particular, I'd like to thank my fellow graduate student, Matthew Lundy for all of his expertise with both the ECM and statistics aspects of this project. Thank you for your patience with me as I tried to learn my first stats. You've been the best friend and colleague I could've asked for, and I could not have done any of this without you. I'd also like to thank Ste O'Brien for sharing his expertise with γ-ray analysis with me. Thank you for your patience in helping me actually get Eventdisplay to work and always being there to help me debug.

I owe a lot of gratitude to my parents for supporting me though graduate school. Thank you for understanding that this was a good use of the last two years of my life. Thank you for being there for me and for sending me the best care packages at the best times.

Many thanks as well to all the members of the VERITAS collaboration for helping with this project, whether it be direct advice on how to improve this project, taking observations of my data, maintaining the instrument and software packages, and most of all, for believing that this project has the possibility to do good science and continuing to give me the opportunity to do this work.

I would also like to thank the CHIME/pulsar collaboration for providing me with a PSR B1937+21 ephemeris, which allowed the entire PSR B1937+21 analysis to be possible.

Finally, I would like to thank my office mates in 060 as well as all the wonderful friends I've made in the physics department and the TSI. Thank you for your support during classes, everyday frustrations, and the writing of this thesis. I wouldn't have found the motivation to come in every day this summer to write this thesis without summer 10 AMs.

There are many others who have helped me through these past two years whom I have probably forgotten from this list. If you knew me and put up with me during this process, I am incredibly grateful.

Statement of Original Contributions

During the course of the author's M.Sc., the following items were contributed to both this project and to other VERITAS projects:

- The author participated in multiple observing shifts at the VERITAS site to collect data for both this project and for other VERITAS work.
- The author initiated and continues to run the VERITAS optical pulsar program, which includes source selection, source proposals, and all analysis.
- The author developed the OOPS-E pulsar analysis pipeline used in this work (outlined in Section 3.2).
- The author identified the ECM settling time issue (discussed in Section 2.3) and continues to try and identify where it originates.
- Finally, the author has participated in or is currently participating in several other VERITAS analyses, including: a pre-analysis algorithm to filter for high energy events, analysis of active galactic nuclei (AGN) H 1722+119 and B3 2247+381, searches for Lorentz Invariance Violation (with other IACTs MAGIC, H.E.S.S., and LST-1), and LHAASO source archival analyses.

List of Abbreviations

ATNF	**A**ustralia **N**ational **T**elescope **F**acility
AXP	**A**nomolous **X**-ray **P**ulsar
CCD	**C**harge **C**oupled **D**evice
CHIME	**C**anadian **H**ydrogen **I**ntensity **M**apping **E**xperiment
CMB	**C**osmic **M**icrowave **B**ackground
CR	**C**osmic **R**ay
CS	**C**urrent **S**heet
CTA	**C**herenkov **T**elescope **A**rray
DACQ	**D**ata **Acq**uisition system
ECM	**E**nchanced **C**urrent **M**onitor
FADC	**F**lash **A**nalog-to-**D**igital-**C**onverters
FOV	**F**ield **O**f **V**iew
GRP	**G**iant **R**adio **P**ulse
HAWC	**H**igh **A**ltitude **W**ater **C**herenkov
HE	**H**igh **E**nergy (Roughly 100 MeV to 100 GeV)
IACT	**I**maging **A**tmospheric **C**erenkov **T**elescope
IR	**I**nfrared
LAT	**L**arge **A**rea **T**elescope
LC	**L**ight **C**ylinder
LED	**L**ight **E**mitting **D**iode
LHAASO	**L**arge **H**igh **A**ltitude **A**ir **S**hower **O**bservatory

LMXB	**L**ow **M**ass **X**-ray **B**inary
MSP	**M**illi**s**econd **P**ulsar
NSB	**N**ight **S**ky **B**ackground
OG	**O**uter **G**ap
PC	**P**olar **C**ap
PIC	**P**article-**i**n-**C**ell
PMT	**P**hoto**m**ultiplier **T**ube
PWN(e)	**P**ulsar **W**ind **N**ebula(**e**)
RRAT	**R**otating **R**adio **T**ransient
SG	**S**lot **G**ap
SGR	**S**oft **G**amma-ray **R**epeater
S/N	**S**ignal to **N**oise **R**atio
SNR	**S**uper**n**ova **R**emnant
tMSP	**t**ransitional **M**illisecond **P**ulsar
VERITAS	**V**ery **E**nergetic **R**adiation **I**maging **T**elescope **A**rray **S**ystem
VHE	**V**ery **H**igh **E**nergy (Roughly 100 GeV to 100 TeV)

Contents

List of Figures

List of Tables

Chapter 1

Introduction

1.1 Pulsars

When first discovered by Jocelyn Bell Burnell in 1967 [1], pulsars were observed to be extremely accurate repeating signals in radio at a fixed right ascension and declination, originating outside of the solar system. Originally thought to be signals from extraterrestrial civilizations, pulsars are now thought to be a subclass of neutron stars; compact remnants from the collapse of massive stars. Pulsars are highly magnetized, rotating neutron stars that emit beams of radiation at short, regular intervals, corresponding to their rotation period.

All known pulsars are born from the collapse of massive ($\approx 10\mathrm{M}_{\odot} - 20\mathrm{M}_{\odot}$) stars into small radius, dense neutron stars. During collapse, the magnetic flux of the star is conserved, such that an initial stellar magnetic field of $B \approx 100$ G will result in a neutron star magnetic field of $B \approx 10^{12}$ G due to the significantly lower surface area of the neutron star. The rapid rotation of the pulsar originates from conservation of angular momentum during collapse, which increases rotation speed by a factor of 10^{10}, resulting in typical pulsar birth periods of ≈ 0.6 - 2.6 ms [2]. There are perhaps other pulsar formation channels, such as white dwarf mergers [3] or the collapse of massive white dwarfs [4], among others. At the time of writing, these formation mechanisms lack concrete observational evidence, so we will focus only on the core collapse supernova formation channel.

Pulsars can be broadly classified into three groups: magnetically powered (magnetars), rotation powered, or accretion powered. The focus of this work will be rotation powered pulsars, where emission is generated by converting rotational energy to electromagnetic winds. This dissipation of rotational energy leads to a gradual slowing down of pulsars as they age.

At the time of writing, there are over 3000 pulsars cataloged in radio wavelengths [5], ≈ 6 in optical, ≈ 150 in X-ray, 278[1] in high energy γ-ray, and 2 in VHE γ-ray [6, 7], though these populations are not strictly overlapping. These numbers include young, magnetic, and rapidly spinning pulsars, often associated with supernova remnants, old pulsars that have radiated away most of their energy, and recycled millisecond pulsars (MSPs) that have low surface magnetic fields but have spun back up to fast periods, likely through accretion in a binary system.

The diversity of the observed pulsar populations can be represented on a $P - \dot{P}$ diagram (e.g., Figure 1.1) that shows the pulsar period, P, plotted against the period derivative, $\dot{P}$. $\dot{P}$ is expected to be relatively constant for "regular" pulsars[4], while P is expected to decrease with age, as the pulsar 'brakes' by converting its rotational kinetic energy to electromagnetic radiation from the dipolar magnetic field. Assuming a spinning dipole model, $\dot{\nu}$ (the spin-down frequency) can be expressed as

$$\dot{\nu} = -\frac{8\pi^2}{3c^2}\frac{M^2 sin^{\alpha}}{I}\nu^3, \tag{1.1}$$

where M is the dipole moment, I is the moment of inertia, α is the inclination angle between the magnetic and rotation axes, and P is the measured rotation period. For constant M, I, and α, we can approximate $\dot{\nu}$ (where $\nu = 1/P$) as

[1]https://confluence.slac.stanford.edu/display/GLAMCOG/Public+List+of+LAT-Detected+Gamma-Ray+Pulsars

[4]The term "regular" pulsar typically refers to rotation-powered, non-accreting pulsars that do not experience nulling events (where the pulsar appears to turn off for significant time periods).

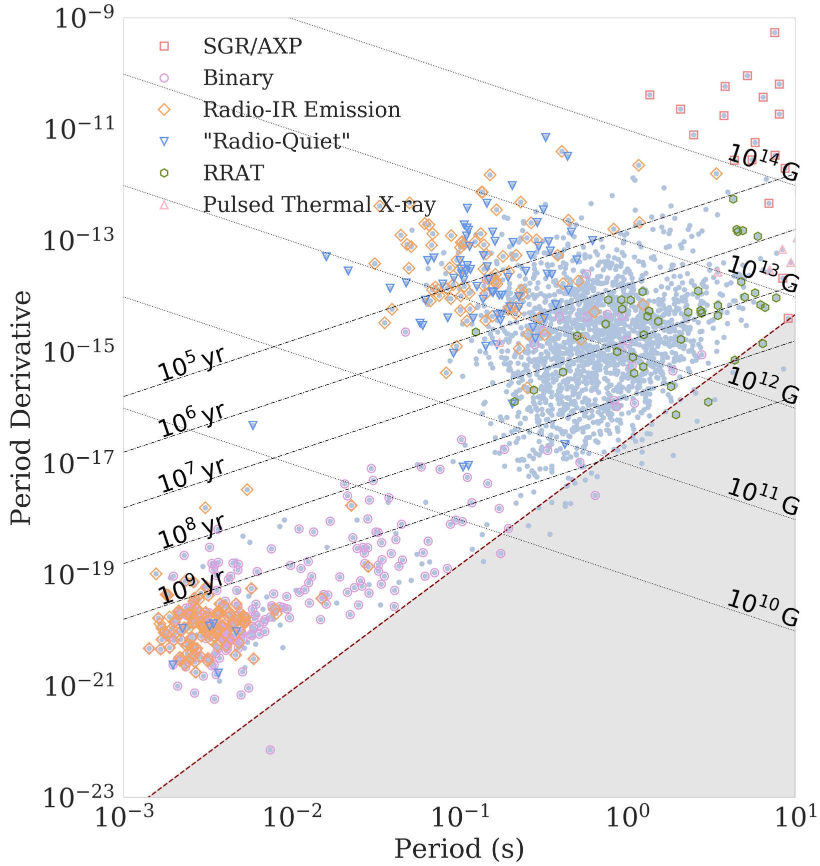

Figure 1.1: $P - \dot{P}$ diagram for all radio pulsars catalogued in the Australia National Telescope Facility (ATNF) catalog, magnetars[2], and rotating radio transients (RRATs)[3]. The data for this plot were obtained and plotted using `psrqpy` [8]. Diagonal dashed lines represent characteristic ages and magnetic fields. Pulsar populations are denoted by different markers, but can generally be categorized into "regular" pulsars in the upper right and millisecond pulsars in the lower left. The red dashed line is the so-called "death line" and the grey shaded region is the pulsar "graveyard", where pulsars are no longer expected to produce much radiation at any wavelength.

$$\dot{\nu} = -\kappa\nu^n, \tag{1.2}$$

where κ is a scaling constant and n is the braking index, which for dipolar magnetic torque is 3. For measured values of $\dot{P}$ and higher order derivatives, if $n \neq 3$, we can be determine if other braking mechanisms (e.g., pure particle outflow [9], changing I values over time [10], or magnetic quadropole dominated braking [11]) are present.

To observationally determine n, a long-term second derivative of the spin frequency is needed. n is defined as

$$n = \frac{\nu \ddot{\nu}}{\dot{\nu}^2}. \tag{1.3}$$

Although few pulsars have $\ddot{\nu}$ measured reliably (since $\ddot{\nu}$ is very small and therefore hard to measure) and precisely enough to measure n, it has been found in almost all cases that $n < 3$. See [12] for a review of braking index studies.

When pulsars spin down, they move to the right in the $P - \dot{P}$ diagram on a line with slope $2 - n$. Therefore, for pulsars with $n = 3$, we expect them to move along a line of constant slope -1, with a more realistic pulsar population moving more steeply to the right. There exists a "death line" , the red dashed line in Figure 1.1, where pulsars are no longer detectable. The line shown in Figure 1.1 corresponds to Eq. 4 of [13], which is based on polar cap models where radio emission is thought to originate (see Section 1.2). Pulsar "death" is thought to be due to the electric fields generated by the pulsar's magnetic dipole becoming too weak to draw charges from the neutron star surface, meaning that nothing can be accelerated to produce emission at any wavelength. However, the "death line" is known to be model-dependent and can vary significantly based on the NS environment; in [13] it is suggested that the death line should instead be a "death valley", in order to accommodate variations in electric field, pulsar geometry, and pulsar emission mechanisms.

There is, however, a sort of escape route that pulsars can take to come back from beyond (or near) the death line. If a pulsar is in a binary system with a low-mass stellar companion (likely low-mass X-ray binary systems; LMXBs), the pulsar can spin up by accreting mass from its companion, which carries with it angular momentum. This process re-adds angular momentum to the pulsar itself and spins the rotation period back up to millisecond periods (similar to the neutron star's initial spin period [14]). Though only about 7% of all known pulsars are in binary systems, most MSPs ($\approx 80\%$) have identified binary companions. This leads to the idea that MSPs spin up to millisecond periods through accretion from the binary companion. MSPs generally have periods in the range $1.4 - 30$ ms, giving them high spin-down power, ($\dot{E}$) but especially low surface magnetic fields (B_{surf}), leading to the idea that these are old pulsars. Transitional millisecond pulsars (tMSPs) are millisecond pulsars in binaries that alternate between states of accretion and rotation power, providing evidence that MSPs can be produced in binary systems.

For this study, we will generally consider MSPs that are no longer accreting (i.e., are fully rotation-powered again) and whose optical observability is not inhibited by the companion's optical brightness or orbit perturbations. For the systems that are considered in this study, the companions are typically absent or dim compact objects such as white dwarfs. However, in Section 4.1, a tMSP [15] (PSR J1023+0038) is considered for study, because its rotation-powered pulses increase in intensity during accretion high states. Further observations of PSR J1023+0038 source and similar sources will be needed to determine if PSR J1023+0038 is a unique source or if looking for optical pulses accretion high states is a good technique for optical pulse searches.

1.2 Pulsar Emission Mechanisms

Rotation-powered pulsars convert their rotational kinetic energy to energy injected into their surrounding plasma at the energy loss rate, $\dot{E}$ or luminosity, L [16]. This relation is described by

$$\dot{E} = L = 4\pi^2 I \frac{\dot{P}}{P^3}. \tag{1.4}$$

In this work, pulsar emission is separated into two categories; radio and high energy (HE), where high energy spans from optical to very high energy (VHE; $E > 100$ GeV) wavelengths. The major difference between these two categories is that radio emission is coherent[5], while HE emission is incoherent. Because of the coherence differences between radio and HE emission, and because most pulsars show different pulse profiles and relative pulse time lags across the electromagnetic spectrum, it is thought that radio and HE emission originate from different emission regions in the pulsar magnetosphere.

Before the pulsed emission from the Crab pulsar was detected in VHE by VERITAS [17], several pulsar models were established based on the characteristics of the X-ray and HE γ-ray emission. These models included polar cap models (PC models; [18]), outer-gap models (OG models; [19], [20]), and slot gap models (SG models; [21]).

All of these models consider accelerated charges from the e+/e- plasma in the pulsar magnetosphere. Goldreich et al. [22] found that a rotating magnetic field induces an extremely strong electric field that exerts a larger force on charged particles (e.g., e+ and e-) than the gravitational force of the NS, pulling charges away from the NS surface. This plasma co-rotates with the NS at distances up to the light cylinder (LC) radius, R_{LC}. The LC marks the distance at which the speed of co-rotating plasma reaches the speed of light, c. Field lines within the LC are able to travel in a frame with velocity $v < c$ and can remain closed but outside the LC, field lines cannot remain in a frame where $v < c$ and are swept back to become open field lines (see Figure 1.2). The LC radius is defined by

$$R_{LC} = \frac{c}{\Omega}, \tag{1.5}$$

where $\Omega = \frac{2\pi}{P}$ with P being the pulsar's rotation period.

Polar cap emission originates from electrons near the NS surface that travel along small-radius magnetic field lines, undergoing curvature radiation. These electrons pair-produce to form photons up to $\approx$ GeV-scale γ-rays. This model predicts a super-exponential energy spectrum of photons (described by Eq. 2 and Eq. 3 in [23]), due to the need for extremely high surface magnetic fields ($B > 10^9 G$) for non-negligible rates of pair production to produce photons more energetic than the electron rest mass [24]. The PC model

[5] Coherent emission means that all photons arrive in the same phase, implying relativistic boosting of the photons.

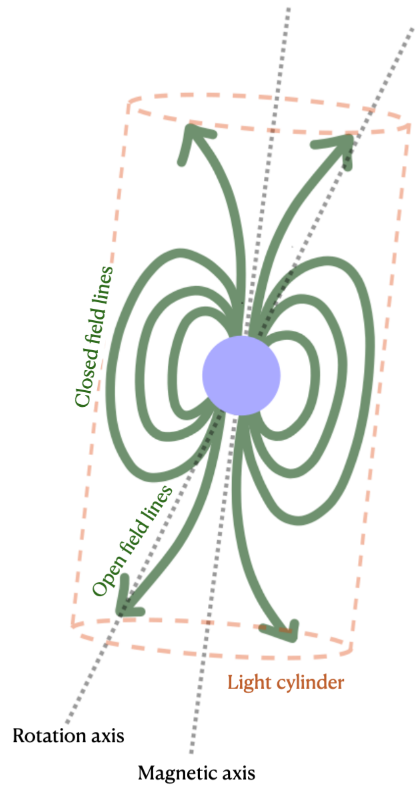

Figure 1.2: Sketch of a pulsar with the main components that are relevant to pulsar emission mechanisms labelled.

first came into question when *Fermi*-LAT found a super-exponential cutoff could be ruled out for the Vela pulsar's spectral shape [25].

The SG model is a correction to the PC model and adds a boundary condition of zero electric field at the last open field line, with pair production occurring at higher altitudes closer to this boundary. Pair production creates e+/e- pairs that can be accelerated near the pulsar's light cylinder (LC), where the e+/e- plasma in the magnetosphere co-rotates with the pulsar at the speed of light.

The OG model predicts emission from vacuum gaps due to a potential drop in the pulsar's outer magnetosphere. OG models predict exponential spectral cutoffs at GeV energies, which agree with *Fermi*-LAT observations [26]. The PC, SG, and OG models are all considered "vacuum gap" models, since these three models describe vacuum voids within a charge separated magnetosphere [27].

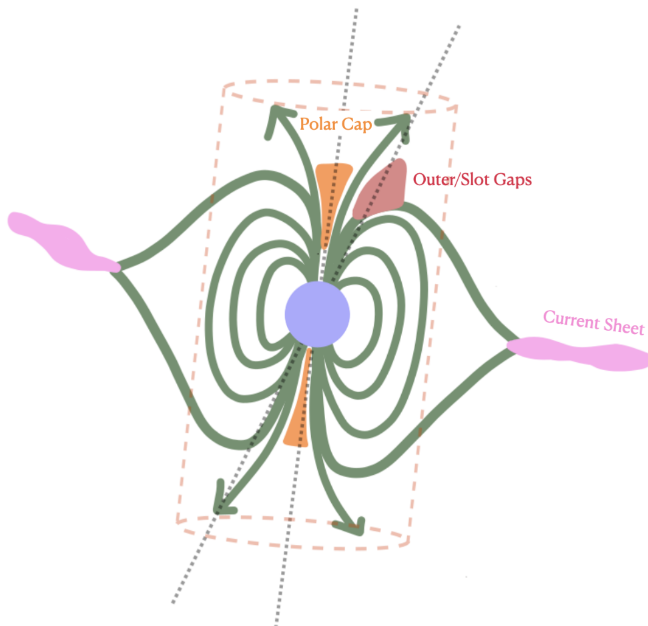

Figure 1.3: Pulsar diagram showing the polar cap (PC), outer gap (OG)/slot gap (SG), and current sheet (CS) models.

Due to the cutoffs at GeV or lower energies, the VERITAS discovery of pulsed VHE ($>$ 100 GeV) emission from the Crab pulsar [6] was completely unexpected. Though follow-up observations of other *Fermi*-LAT detected pulsars with VHE instruments yielded null results, it remains important to find emission models that allow the emission of VHE photons. It is now believed that emission originates near the current sheet [28], formed by currents flowing along open field lines (pulsar winds) rather than in a vacuum gap. This creates a strong electric field that accelerates particles (mostly e+), which can pair produce to create photons up to TeV energies. Amendments to previous models have been attempted, such as the inclusion of secondary and tertiary e+/e- pairs in the OG model [29] and a synchrotron self-Compton process in the SG model [30], but neither accurately predicts the Crab pulsar's TeV spectrum, leaving the current sheet model as the currently preferred model. Figure 1.3 shows the location of these regions with respect to a typical pulsar and its magnetic field lines.

Substantial progress has been made to develop models that accurately describe the observed HE pulsar emission, thanks to instruments like *Fermi*-LAT and simulation developments like particle-in-cell (PIC) simulation codes (e.g., [31]). However, there is no model that fits well to all HE wavelengths and pulsar types (i.e., both MSPs and "regular" pulsars). Obtaining pulse profiles and spectral points at all HE wavelengths is something that will greatly help constrain which models are acceptable. Though HE γ-ray and X-ray wavelengths are well covered by observations from instruments like *NICER* and *Fermi*-LAT, pulsar detections are still largely missing in optical and MeV wavelengths, mostly due to either lack of instruments or instrumental limitations for rapid time series recording. This thesis aims to introduce the VERITAS VHE γ-ray telescopes as tools that will likely be able to better constrain optical and VHE emission properties in the near future.

1.2.1 Pulse Profiles

The shape and timing of the pulses from pulsars can provide insight into the emission mechanisms, emission regions, and geometry of the pulsar. A pulse profile is the integration of all the pulses collected during a given exposure (see Figure 1.4), which gives observations that are stable with time, whereas single pulses have been observed to be highly variable due to both stochastic and systematic effects. Further discussion of single pulse variability can be found in [32].

Most integrated pulses consist of a main pulse, which occurs when the pulsar's light beam sweeps across the Earth's line of sight. For pulsars that are inclined such that their magnetic poles face the Earth, an interpulse may be visible as the other pole's light beam sweeps across Earth's line of sight. Only a small minority of pulsars have an observable interpulse, which are primarily young pulsars, indicating that there may be alignment between the pulsar's magnetic and rotational axes as the pulsar ages [34]. Generally, the pulsar is undetectable outside of the pulsed emission, indicating that the radiation is confined to a narrow beam, originating from a small region in the magnetosphere.

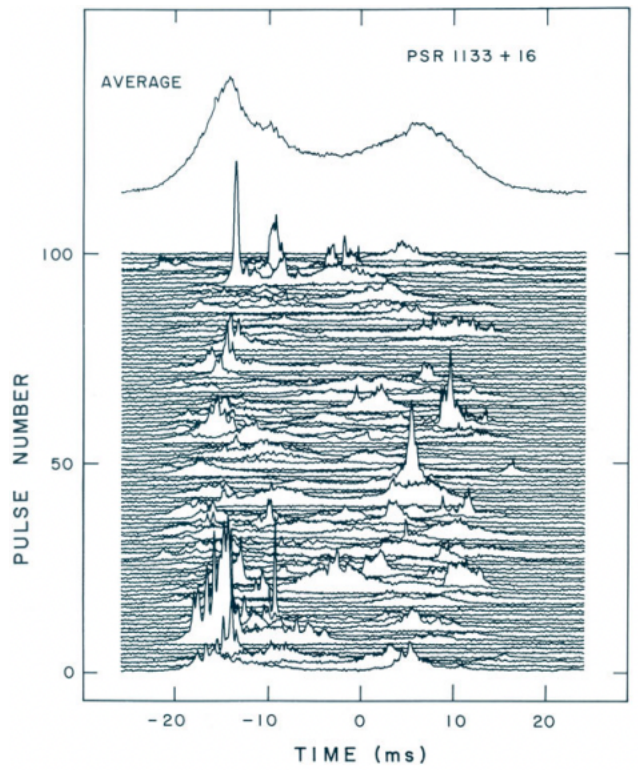

Figure 1.4: Example of an integrated pulse (top) and individual pulses (bottom). From [33].

Differences in pulse profile widths are understood to come from differences in the pulsar beam's radial profile. Pulsar beams consist of both conal [35] and core [36] components and the angle at which the beam intersects our line of sight will allow different components to be seen (see Figure 1.5). The effect of the cone/core structure on the pulse width, sharpness, and pulsed fraction can explain the diversity seen in observed pulsars across the electromagnetic spectrum (see Figure 8 of [37] for radio pulse examples).

Additionally, the diversity in pulse profiles does not just exist within single wavelengths, but most pulsars show different pulse profiles and pulse timing at different wavelengths[6] (see Figure 1.6). Timing and shape differences indicate that pulses of different wavelengths must be originating from different regions of the pulsar magnetosphere. It is therefore important to understand the pulse profiles of different pulsars and pul-

[6]Generally these differences are between radio and high energy (optical, X-ray, HE γ-ray, and VHE γ-ray) wavelengths, whereas all HE wavelengths tend to show phase alignment with each other.

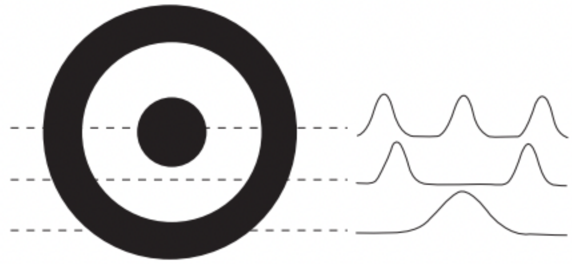

Figure 1.5: A sketch of the cross-section of a pulsar beam showing core (central circle) and cone (outer ring) of the beam. The pulse profiles expected from observations at lines of sight represented by the dashed lines are shown. From [33].

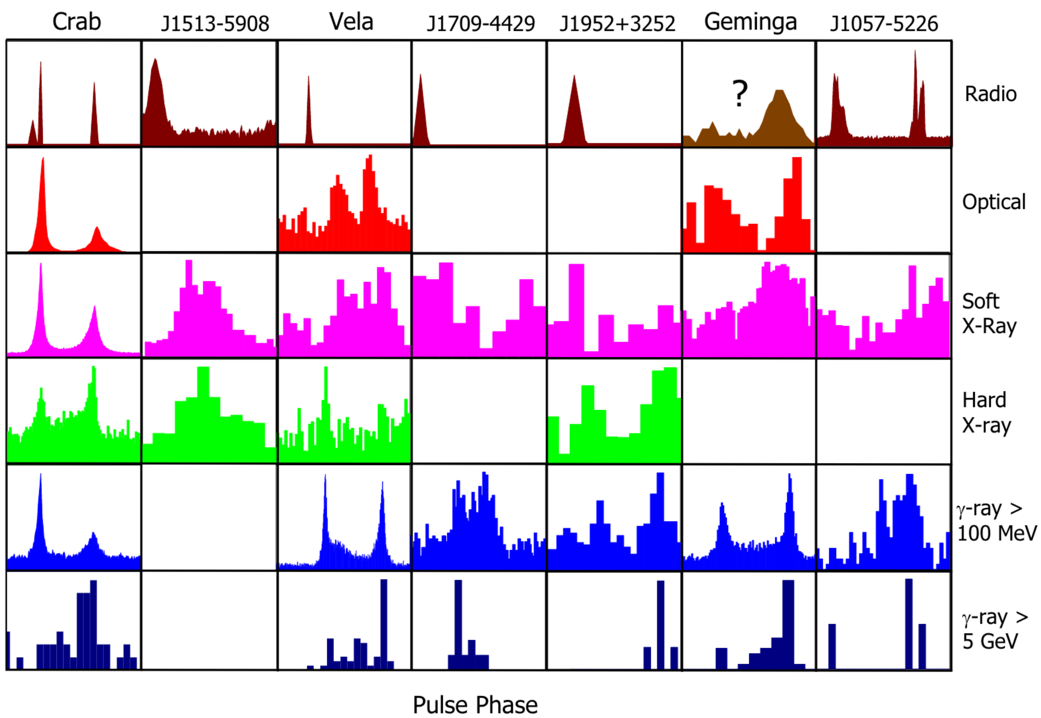

Figure 1.6: The multiwavelength pulse profiles of selected pulsars as known in 2007. Geminga radio emission is labelled with a question mark because radio emission had not yet been confirmed when this figure was made. From [38].

sar populations in order to better constrain pulsar emission mechanisms. Particularly, since only ≈ 6 pulsars are known to pulse in optical wavelengths, learning more about the shapes of optical pulses may be able to determine if there is any connection between radio and X-ray/γ-ray emission mechanisms.

1.3 Non-Pulsed Emission from Pulsars

Since pulsars are energetic sources with strong magnetic, particle-driven winds and are often born in supernova remnants that offer rich environments for particle interaction, it is expected that the region surrounding the pulsar is also of interest in high energy astrophysics. In fact, most of the pulsar energy (Eq. 1.4) is converted into pulsar winds, rather than pulsed emission. At least two types of systems are seen in VHE that are coincident with pulsars: pulsar wind nebulae (PWNe) surrounding young pulsars and TeV halos which are known to surround middle-aged pulsars and may be present around pulsars of all ages.

1.3.1 Pulsar Wind Nebulae

The most famous and first example of a VHE γ-ray detection, the Crab nebula [39], is a PWN (see Figure 1.7). These energetic systems are powered by highly relativistic (Lorentz factor $\Gamma_w >> 1$) magnetic and particle winds that blow out cold plasma left over from the pulsar's progenitor star out through open magnetic field lines. Radio, optical and X-ray nebula emission are produced by e+/e- pairs that spiral along magnetic field lines, producing synchrotron radiation. γ-ray emission originates from synchrotron self-Compton (SSC) processes, as the syncrotron-produced pairs up-scatter background photons[7] to GeV and often higher energies.

At the time of writing, 111[8] PWNe have been identified [41], most of which are seen across the high energy spectrum from keV to TeV (and now higher) energies.

PWNe As PeVatrons

The spectrum of PWNe is thought to extend up to hundreds of TeV before being cut off by Klein-Nishina suppression [42]. The cutoff in the Klein-Nishina regime originates from repeated up-scattering of e+/e- pairs as they approach the rest-mass energy of the

[7]These are other synchrotron photons, CMB photons, or extragalactic background light photons
[8]http://snrcat.physics.umanitoba.ca/index.php?

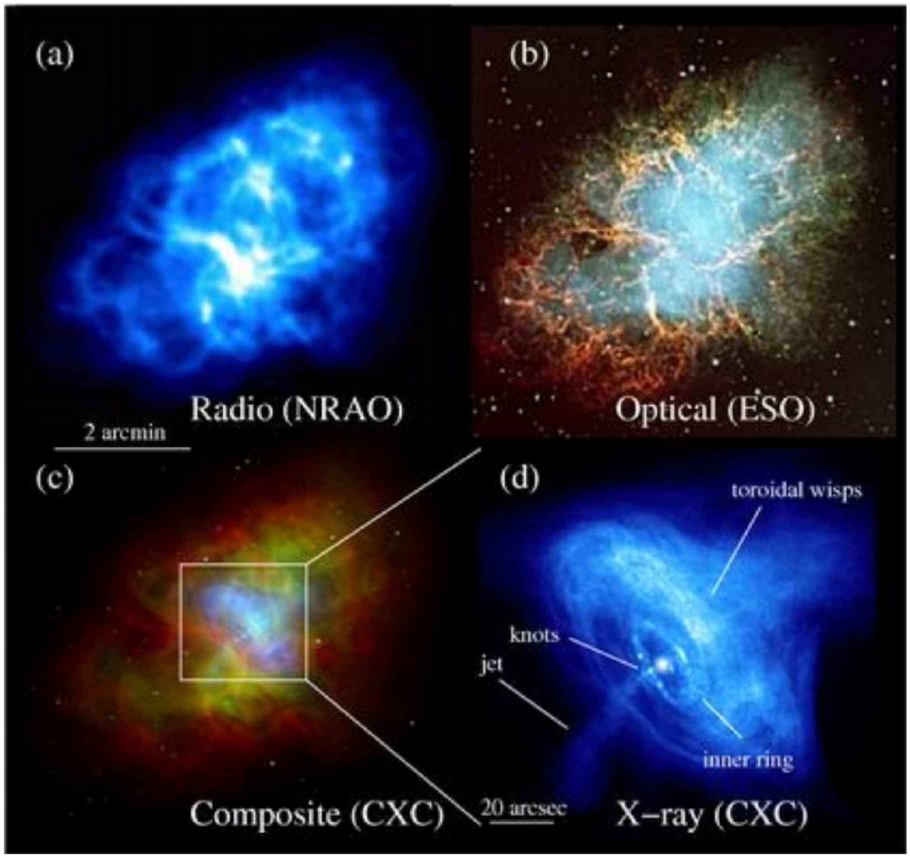

Figure 1.7: The Crab nebula as seen in radio (a), optical (b), composite radio/optial/X-ray (c), and X-ray (d) wavelengths. The PWN corresponds to the emission seen in the X-ray image. From [40].

electron $E = m_e c^2$ and the interaction cross-section becomes inversely proportional to the energy of the photon produced at each scattering. This decreasing interaction cross-section makes it difficult for photons above several hundred TeV to be produced, creating a spectral cutoff. Recently, ultra high energy (UHE) photons above 1 PeV have been detected from the Crab nebula by the LHAASO γ-ray detector [43], indicating continuation of the spectrum for young, nearby sources to the UHE regime.

LHAASO's Crab detection helps corroborate the idea that PWNe may be PeVatrons - extremely energetic Galactic systems capable of accelerating particles to PeV energies. The search for PeVatrons is motivated by the extension of the charged particle cosmic ray (CR) spectrum up to PeV energies, despite no evidence of other particles, previously including photons, up to those energies. Since CRs are charged particles whose trajectories are deviated by Galactic magnetic fields, it is difficult, if not impossible to trace them back to their birth places. On the contrary, particles such as neutrinos and γ-rays can be produced in hadronic processes alongside CRs but are electromagnetically neutral and therefore arrive at Earth directly from their sources. Identifying PeVatron γ-ray sources is critical for finally determining the origin of the flux of cosmic rays (see Figure 1.8) that has remained a mystery for over a century [44].

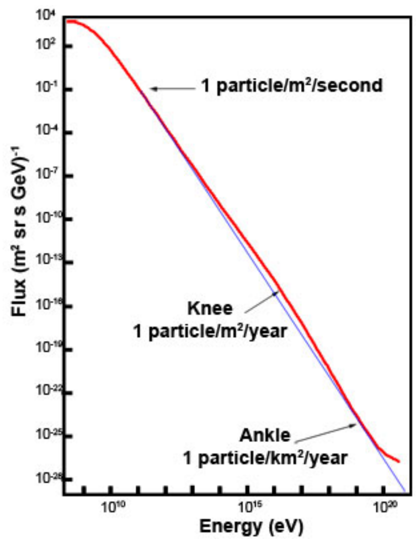

Figure 1.8: Energy spectrum of the observed charged particle cosmic ray flux. The blue line is an exponential fit to the observed data, which is denoted by the red line. From Swinburne University of Technology[9].

PWN Evolution

The following section makes use of [45].

Young PWNe are especially bright due to their rich supernova remnant (SNR) environments for particle interaction and their powerful central pulsar engines. The structure of the SNR itself plays a large role in determining the evolution of the PWN. While the pulsar age can indicate the energetics of the pulsar winds being injected, the character-

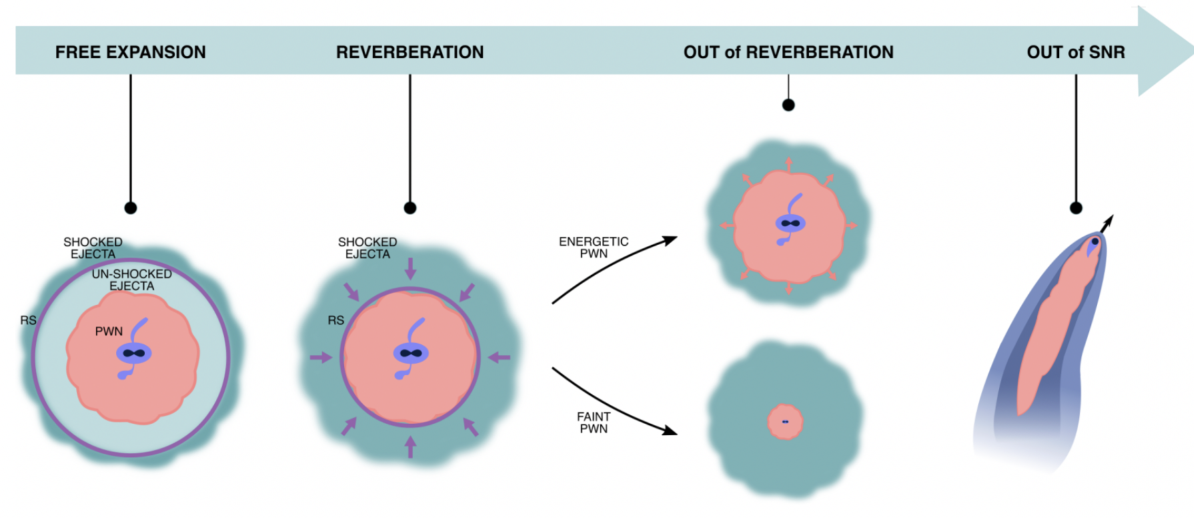

Figure 1.9: Evolutionary stages of a PWN. The central pulsar is the black dumbell shape, the PWN is the purple central nebula, the SNR is light red, and the shocked and unshocked interstellar medium (ISM) are light and dark blue, respectively. From [45].

istic age of the supernova remnant (as determined by [46]) has proven to much more accurately model PWNe. Characteristic age is determined with

$$t_{ch} = E_{sn}^{-1/2} M_{ej}^{5/6} \rho_{ISM}^{-1/3}, \tag{1.6}$$

where E_{SN} is the SN explosion energy ($\approx 10^{53}$ erg)[10], M_{ej} is the mass of the SN ejecta, and ρ_{ISM} is the number density of hydrogen in the surrounding interstellar medium.

The first evolutionary stage of PWNe is free expansion into the cool surrounding SNR, which is freely expanding itself (leftmost diagram in Figure 1.9). At this stage, there is thought to be no interaction between the PWN and SNR [47].

The next stage occurs when the PWN expands into the reverse shock of the SNR; a reflection of the initial, forward shock wave sent out by the SN as the forward shock wave interacts with the interstellar medium (ISM) (see the middle-left diagram in Figure 1.9). This is the first time that interaction occurs between the PWN and the SNR. The

[10] This is only 1% of the total supernova energy, since the other 99% has already been radiated away as neutrinos.

SNR exerts pressure on the PWN, causing an increase in both the energy and the magnetic field within the PWN. The pressure difference eventually subsides, leaving a much higher pressure PWN that can continue to expand into the SNR, for cases when the PWN is sufficiently energetic (see the middle-right diagram in Figure 1.9). However, when the PWN is not sufficiently energetic, it becomes compressed by the SNR and contracts, leading to large increases in particle energetics. Bandiera et al. [48] find through numerical simulations that the latter seems to be the case for most observationally studied pulsars.

Furthermore, it is important to note that pulsars do not remain stationary at the center of their associated SNRs and are moving at high velocities ($v \approx 152$ km/s for "regular" pulsars and $v \approx 54$ km/s for MSPs [49]). Pulsars are born with initial velocities or natal kicks due to the momentum imparted on them during the supernova explosion of their progenitor. Along with velocity boosts from gravitational interactions with other bodies, the natal kick constitutes the proper motion of a pulsar. Post-reverberation, the PWN morphology becomes difficult to model because of pulsar proper motion effects and mixing of the PWN with its surrounding medium due to gradients in the ambient medium density. During the post-reverberation stage, PWN are expected to strongly depart from spherical symmetry, which agrees with observations of asymmetric emission around middle-aged pulsar systems, such as Geminga Aharonian et al. [50]. From here, the pulsar is expected to undergo subsonic expansion into the surrounding medium for $\approx 20\ t_{ch}$[51].

After the post-reverberation phase, the proper motion of the pulsar begins to dominate the evolution of the PWN. The pulsar (and its accompanying PWN) will eventually leave the SNR (see the right diagram in Figure 1.9) and will subsequently only interact with the ISM. The pulsar travels at supersonic speeds through the ISM [52], shocking the ISM at the head (where the pulsar is located), called a bow shock PWN. The bow shock PWN is the final known evolutionary stage of the PWN, which will continue speeding through space as a PWN until the pulsar crosses the death line and can no longer power pulsar winds.

1.3.2 TeV Halos

Discoveries by Milagro [53] and the High Altitude Water Cherenkov Observatory (HAWC) [54] of diffuse, non-thermal TeV γ-ray emission surrounding the middle-aged pulsars Geminga (see Figure 1.10) and Monogem beyond the radius of the observed X-ray PWN motivated a new source class, dubbed TeV halos. These sources are particularly interesting as PeVatron candidates, because their energetics and extension indicate that CR acceleration to PeV energies could be possible [55]. It is currently not known whether TeV halos have independent origin, morphology and evolution to PWN. Survey instruments, like HAWC, Milagro, and now LHAASO [56] detect large regions of extended emission and are better suited to detecting TeV halos than pointing γ-ray telescopes, called Imaging Atmospheric Cherenkov Telescopes (IACTs; see 2.1). IACTs, however, are capable of higher angular resolution observations that can better constrain the morphology of these systems.

The authors of [55], argue that TeV halos are a separate morphological class from SNRs and PWNe. The TeV halos of young pulsars are notably less radially extended than SNRs but much more than PWNe (see Figure 1.11), especially in the case of middle-aged pulsars in the bow shock PWN evolutionary stage (see Figure 1.12), which is not a feature that is predicted by current PWN and SNR evolution models. These authors believe that pulsars of all ages host TeV halos and that these TeV halos arise from e+/e- pairs that escape the PWN and interact with either the SNR (for young pulsars) or the ISM (for older pulsars whose PWN have escaped their SNR, e.g., Geminga).

The authors of [54] find that HAWC-identified TeV halos generally increase in extension with characteristic age, t_{ch} and decreasing spin-down power. This indicates that older pulsars have more extended TeV halos than younger pulsars due to continued interaction of pulsar winds with the SNR or ISM. However, luminosity was found to be roughly constant at $L \approx 10^{33}$ erg/s and the spectral index at $\Gamma \approx 2.2$ for all TeV halos and PWN. This, however, could be due to observational bias, because PWNe and TeV halos with low luminosity and soft spectra fall below HAWC's sensitivity.

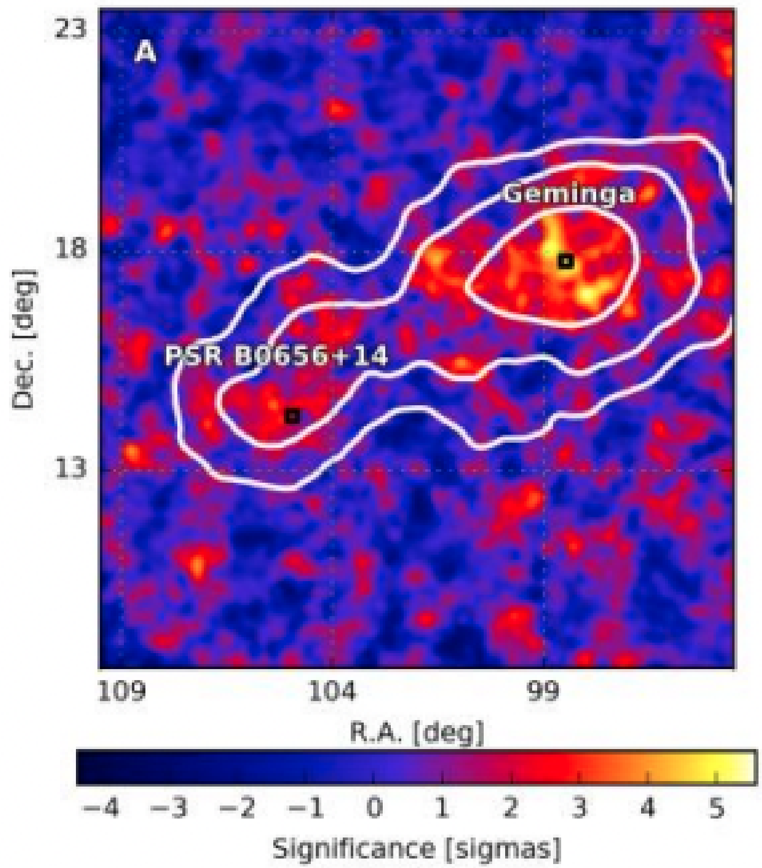

Figure 1.10: HAWC sky map of the VHE emission associated with Geminga (PSR J0633+1746) and Monogem (PSR B0656+14). This emission is considered to be a TeV halo because the large extension is not seen in other wavelengths. From [57].

TeV halos are also of interest for pulsar discoveries, since their emission is believed to be isotropic and un-beamed. Pulsed radio emission from pulsars is dependent of the alignment of the pulsar jet with the line-of-sight to the pulsar. If the jet is mis-aligned, then no pulsed radio emission will be detected from the pulsar. Since other HE pulsed emission are thought to come from a different region of the pulsar magnetosphere, different emission regions may explain why some γ-ray bright pulsars are radio-quiet. Misaligned pulsars should still have TeV halos visible from any line-of-sight, meaning that pulsar candidates may be identified by following up TeV halo candidates with multi-wavelength instruments.

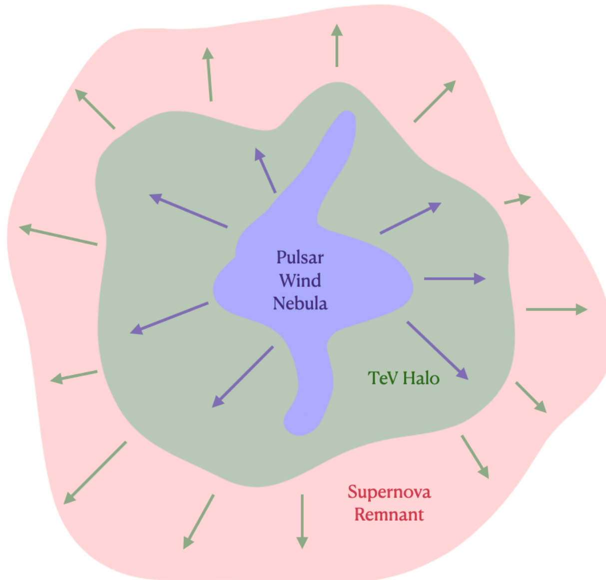

Figure 1.11: Sketch of the relative sizes of PWNe, TeV halos, and SNRs. The arrows represent the outward expansion of each region. This diagram is not to scale, since the absolute scale of each component varies significantly from system to system. SNRs are typically $\approx 1 - 100$ pc in diameter [58], PWN are typically $\approx 0.1 - 1$ pc in diameter [40], and the typical size of TeV halos is not currently known due to small sample sizes, but expected to be ≈ 10 pc in diameter [59] and up to 50 pc in diameter for middle-aged pulsars (e.g., Geminga [50]).

At the time of writing, TeV halos are still a relatively new discovery, with their origin, evolution, and morphology still not well understood. Detections of new, extended TeV sources, often up to hundreds of TeV energies by LHAASO [60] have given VHE instruments a lot to work with on the TeV halo front, and hopefully there will be many exciting developments to come with deeper observations.

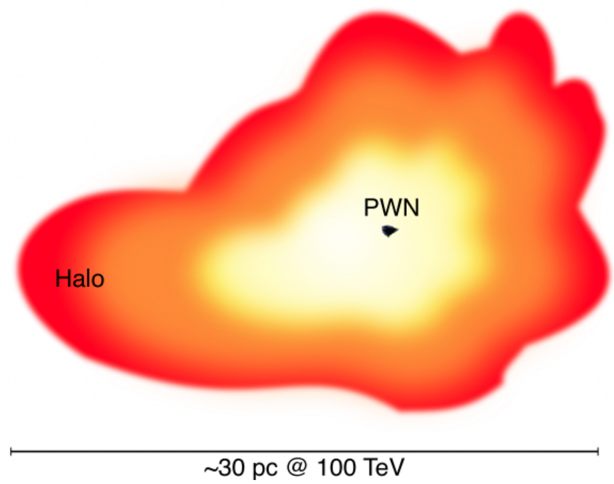

Figure 1.12: Sketch of the relative scales of the Geminga bow shock PWN seen in X-rays (central black semi-circle) within the TeV halo seen by HAWC (see Figure 1.10). From [45].

Chapter 2

The VERITAS Array

2.1 The Imaging Atmospheric Cherenkov Technique

The Very Energetic Radiation Imaging Telescope Array System (VERITAS) is a ground-based γ-ray observatory located near Tucson, Arizona at +31° 40′ 30.21″, -110° 57′ 7.77″ and an altitude of 1.27 km. VERITAS uses the imaging atmospheric Cherenkov technique to detect γ-rays at VHE energies ($E > 100$ GeV), which extends above the energy sensitivity of space-based pair-production telescopes, such as *Fermi*-LAT. IACTs have the advantage of a much larger effective area than is feasible for satellite telescopes, which is useful for > 100 TeV γ-rays, whose fluxes rapidly decrease with increasing energies.

Though Earth's atmosphere is opaque to particles (including photons) at ultraviolet and higher energies, particles at VHE energies are capable of interacting with atmospheric molecules in order to produce particle air showers. For γ-rays, purely electromagnetic cascades are created, which differentiates them from hadronic showers originating from protons and nuclei (though electron cosmic rays will also produce electromagnetic cascades). Electromagnetic γ-ray air showers begin with a γ-ray photon pair-producing with an upper-atmosphere nucleus to produce an e+/e- pair, with the original photon's energy roughly divided equally between the pair. Pair production is described by

$$\gamma + M \longrightarrow e^{+} + e^{-} + M^{*}, \quad (2.1)$$

where γ is the original photon, M is the mediating atmospheric nucleus, and M^{*} is an excited state of M.

The e+/e- pair travels downward in the atmosphere and produces more gamma-rays via bremsstrahlung radiation by interacting with the electromagnetic field of other atomic nuclei in the atmosphere. These lower energy γ-rays will continue to pair-produce and the shower will evolve exponentially, creating a cascade of particles (see Figure 2.1. The shower will reach its maximum when the particles reach $\approx$ 84 MeV, where their energy loss is dominated by ionization of atmospheric particles and not particle creation. Higher energy particles continue further in the atmosphere before reaching the shower maximum, creating larger light pools on the ground (see Figure 2.2).

The e+/e- pairs produced from γ-rays are capable of exceeding the speed of light in the atmosphere, $v_l = c/n$, where n is the refractive index of the atmosphere. When a charged particle moves through the atmosphere, the electromagnetic field associated with the particle polarizes the atmosphere along the particle's track, displacing the electrons in atmospheric atoms to follow the particle's waveform. For a particle moving at $v_p > v_l$, the electrons cannot return to their original positions faster than the speed of light, so a shock front of polarized medium is induced. The shock front creates coherent optical radiation, called Cherenkov radiation, which will be emitted in a cone of fixed angle with respect to the particle's initial direction of motion.

Cherenkov light is an effect not just limited to the atmosphere, and is, in fact, more pronounced in media with a higher refractive index than air, such as water. Cherenkov radiation was first detected in Earth's atmosphere in 1953 [63], from which it was understood that this radiation has many applications to characterizing the nature of the various particles that intersect our atmosphere.

The angle at which Cherenkov radiation is emitted from a given particle is given by

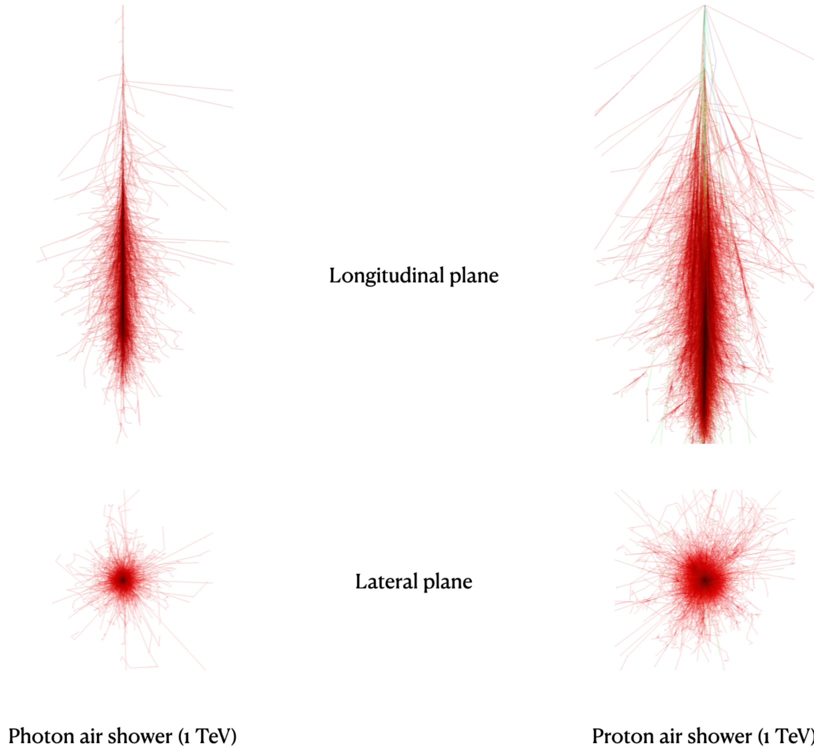

Figure 2.1: The longitudinal and lateral developments of photon (left) and proton (right) induced air showers. Compiled by Fabian Schmidt, University of Leeds, UK, using Corsika simulations [61].

$$cos(\theta_c) = \frac{c}{v n_{air}}, \tag{2.2}$$

where v is the particle velocity and n_{air} is the refractive index of air. At ground level, the spectrum of Cherenkov light in air peaks at 340 nm, with shorter wavelength photons being absorbed by atmospheric particles (see Figure 2.11). The projection of all Cherenkov light generated by a single e+/e- progenitor particle falls into a light pool of radius $\approx$ 130 m on the ground, with a size independent of energy for $\gtrapprox 50$ GeV. The Cherenkov photons from a given shower will all hit the ground within a few nanoseconds of each other.

Large optical reflectors can be used to image these light pools on the ground. From below, the Cherenkov showers from photons are imaged as ellipses with their semi-major axis pointing at the source location. The shower images are offset from the source location

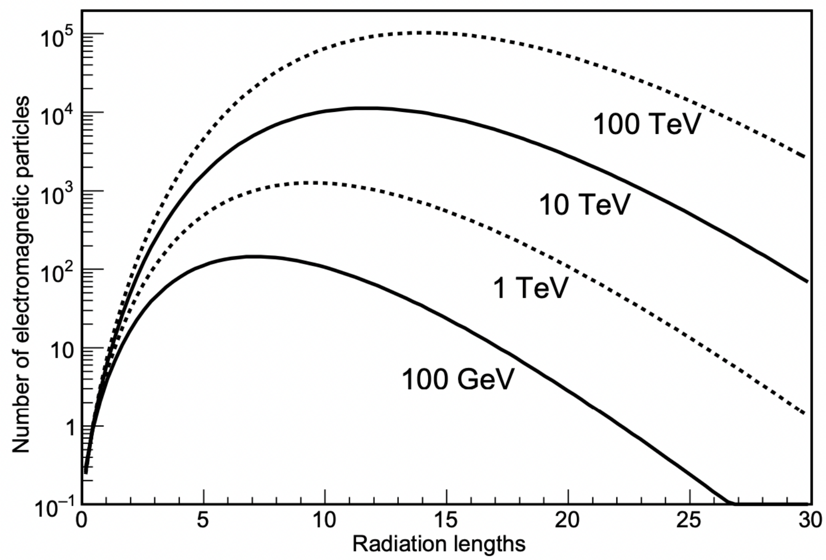

Figure 2.2: The longitudinal development of an air shower for γ-rays at various VHE energies. VERITAS is located at an altitude of 1200 m or $\approx$ 10 radiation lengths into Earth's atmosphere. From [62].

in the focal plane, necessitating a large field of view, even for sources that are point-like. The size of the ellipse can be used to reconstruct the position and energy of the photon, as well as discriminate between photons and other particles (e.g., protons and muons). The techniques used to reconstruct γ-rays from their air showers are outlined in Sections 3.1.4 and 3.1.7.

Charged cosmic rays have a much higher flux than photons and therefore overwhelm the rate of air showers in the atmosphere at any given time. However, the shapes of these showers differ depending on their progenitor particle (see Figure 2.1), which aids in isolating γ-rays from the cosmic ray background. Background subtraction is discussed more thoroughly in 3.1.7.

2.2 The VERITAS Instrument

2.2.1 Mirrors

Each of the four VERITAS telescopes has an assembly of 350 hexagonal mirrors, following the Davies-Cotton design [64], with a total reflecting area of ≈ 100 m^2. Though this is smaller than the light pool radius (≈ 130 m), a telescope placed anywhere in the light pool will be able to image the shower and measure shower parameters, so a larger collecting area will just allow for more photons to be detected. The mirrors are mounted to a steel optical support system, which is attached to a pedestal base equipped with an altitude/azimuth positioner (see 2.3). The VERITAS telescopes are unprotected, meaning that the mirrors slowly degrade over time, due to exposure to the elements - reflectivity losses (at a wavelength of 320 nm) are approximately 3 - 6% per telescope per year. Most mirror damage can be recovered by washing and re-aluminizing each mirror every year. This is typically done during summer months, when VERITAS must shut down due to monsoon storms. The advantage of using many mirrors over a single mirror, as is done with most optical telescopes, is that the cost is greatly reduced in not having to manufacture a 12-m diameter mirror and the individual facets can easily be removed for re-coating.

In order to achieve an optical point spread function (PSF), where the mirrors are providing the sharpest focus possible and performing close to a single reflector, the mirrors must be aligned before use. This is done using a raster scan method, as described by [65], which uses a digital camera mounted to the focal plane of each telescope to image the reflector while the camera is pointed at a bright star. The brightness of the facet in the image gives information about its misalignment.

Compared to typical optical telescopes, IACTs can have much coarser optical angular resolution and larger pixel size. This is because the characteristic angular size of a Cherenkov image is $\approx 0.25°$, whereas typical astrophysical targets for optical telescopes are generally $\approx$ arcseconds in size.

Figure 2.3: T1 shown with all major components highlighted. T2, T3, and T4 are identical.

2.2.2 Camera

A camera is mounted at the focal plane of each telescope, consisting of 499 Hamamatsu R10560-100-20 High QE photomultiplier tubes (PMTs)[1]. PMTs are vacuum tubes with a setup as shown in Figure 2.4. Photons enter the PMT through the input window into the photocathode, where electrons are excited via the photoelectric effect, sending them into the vacuum tube. The photoelectrons then interact with a series of dynodes - electrodes with increasing positive potential moving down the tube. The photoelectron will excite the dynode's material to produce secondary electrons, which interact with the next dynode to produce more electrons. This process is repeated until the electrons produced in the final dynode reach the anode at the end of the PMT. At the anode, there are $\approx 10^6 - 10^7$ electrons for each photoelectron. The anode collects the electrons and outputs them as current to an external circuit.

[1] Hamamatsu PMT handbook v4E

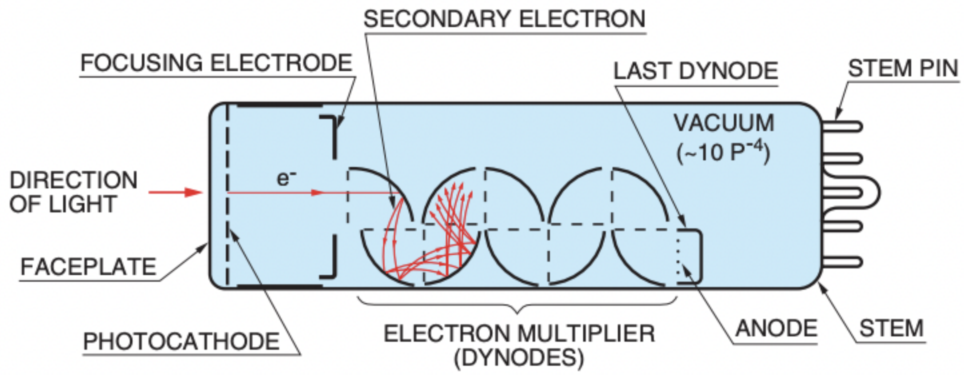

Figure 2.4: Schematic of the photomultiplier tubes used in the VERITAS cameras. From Hamamatsu PMT handbook v4E.

The PMTs are cylindrical in shape, and are arranged in a hexagonal pattern within the camera. To minimize light loss between pixel edges, hexagonal light concentrator (Winston) cones made of machined plastic coated with aluminum (for reflectivity) are placed on a plate mounted to the camera plane. These light cones increase light collection efficency at the photocathodes from 55% to 75% [66].

2.2.3 Data Acquisition and Triggering

The PMT charge outputs from the anodes at the back of each tube are subsequently amplified by a pre-amplifier and then transferred via coaxial cables into the data acquisition systems located in each telescope's neighbouring trailer. These cables are fed into flash analog to digital converters (FADCs), which digitize the amplified PMT signal with 8-bit precision at a rate of 500 MHz in 2 ns samples (the approximate width of a Cherenkov trace). FADC output is fed into 64 microsecond circular buffers to temporarily hold the digitized signal until a trigger system (described below) determines whether or not the data should be saved.

To quantify night sky background (NSB) fluctuations such that they are both positive and negative, a constant voltage value is injected into FADC inputs on top of the amplified PMT signal. "Pedestal events" are forced triggers that are saved at a rate of 3 Hz, which allow a measure of the NSB value and its variance. These are used later, during data analysis, to quantify the NSB, so that PMT traces are integrated from the correct baseline.

In order to better reject NSB fluctuations and hadrons from being reconstructed as γ-rays, VERITAS has a three level trigger system. The trigger system is primarily used keeps file sizes manageable by only saving data that is expected to be useful.

The level one (L1) trigger consists of constant fraction discriminators (CFDs) and threshold discriminators for each PMT. Each signal is separated into two copies, with one going through the L1 trigger and the other copy being digitized through the FADCs. L1 triggers if the pixel has exceeded a given threshold voltage (50 mV); if observations are taken during moonlight, these thresholds are raised to 60 mV to reduce triggering on moonlight photons. CFDs are used to accept events that are a given fraction of the total pulse amplitude rather than a numerical amplitude cutoff, which helps ensure uniformity across different signal brightnesses. During dark, clear conditions, L1 triggers occur at rates of order MHz on each PMT.

The level two (L2) trigger requires that at least three neighbouring pixels meet the L1 trigger condition. This discriminates air shower-like events from NSB fluctuations, pixels pointing at bright stars, or pixels that are stuck at a high voltage. L2 triggers at a rate of $\approx$ kHz during good observing conditions.

Finally, the level three (L3) trigger is an array-based system. L2 triggers are passed via fibre optic cables to the L3 trigger system located in the central control building. This trigger requires that events that pass L2 triggers are seen in more than one telescope (with a time delay to account for different cable lengths), which primarily reduces the muon background. Cherenkov light from muons originates low in the atmosphere, causing them to create relatively small showers compared to hadrons and photons. Cherenkov light pools from muons will not be large enough at the ground to be captured by more than one telescope. L3 triggers at a rate of $\approx$ 300 Hz during good observing conditions.

If L3 conditions are satisfied, a signal is passed back to each telescope, which will enable the digitized signal in buffer to be saved. From here, computers in each trailer called

Event Builders save the FADC information from each pixel, along with a corresponding event number. These events are then sent to a central computer in the control building, called the Harvester, which will assemble the event information from each telescope into full data files.

2.2.4 Sensitivity

VERITAS is a stereoscopic array consisting of four telescopes. The stereoscopic technique [67] is achievable for arrays of telescopes and is useful for improved background rejection, muon rejection, angular resolution, and energy resolution. Figure 3.9 shows the use of VERITAS' 4-telescope array to reconstruct the direction of a γ-ray from images of its Cherenkov light. The stereoscopic technique and directional reconstruction are further discussed in Section 3.1.5.

The sensitivity of VERITAS is defined as the amount of time needed to observe a source with a given flux and spectrum (see Figure 2.5). More exposure time on a source increases VERITAS' sensitivity to dim sources, but there exist many sources that are too dim at VHE energies to be observed in a reasonable amount of time (< 100s of hours). The array's sensitivity determines the energy threshold, which constrains the lowest energy events that can be triggered on and reconstructed.

VERITAS has undergone two major upgrades over its lifetime. These upgrades separate VERITAS data into three epochs: V4 being the initial telescope configuration, V5 after moving T1 to obtain a more symmetric array in 2009 (see Figure 2.6), and V6 after replacing the original PMTs with the new Hamamatsu R10560-100-20 High quantum efficiency PMTs in 2012. All upgrades have resulted in increased sensitivity and a lower energy threshold. Since lower energy showers are much dimmer and smaller in the camera, improvements to imaging capabilities tend to increase the number of low energy events that are recovered.

Sensitivity also depends on observational parameters, such as the camera's zenith angle, the distance of the source from the centre of the camera, and the brightness of the

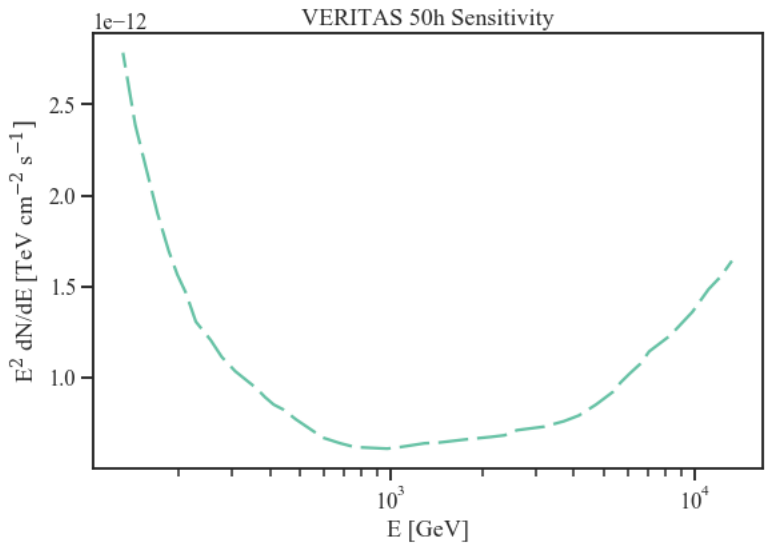

Figure 2.5: VERITAS sensitivity after 50 hours of observations. The dashed line represents the minimum energy flux needed for photons of a given energy to be detected by VERITAS.

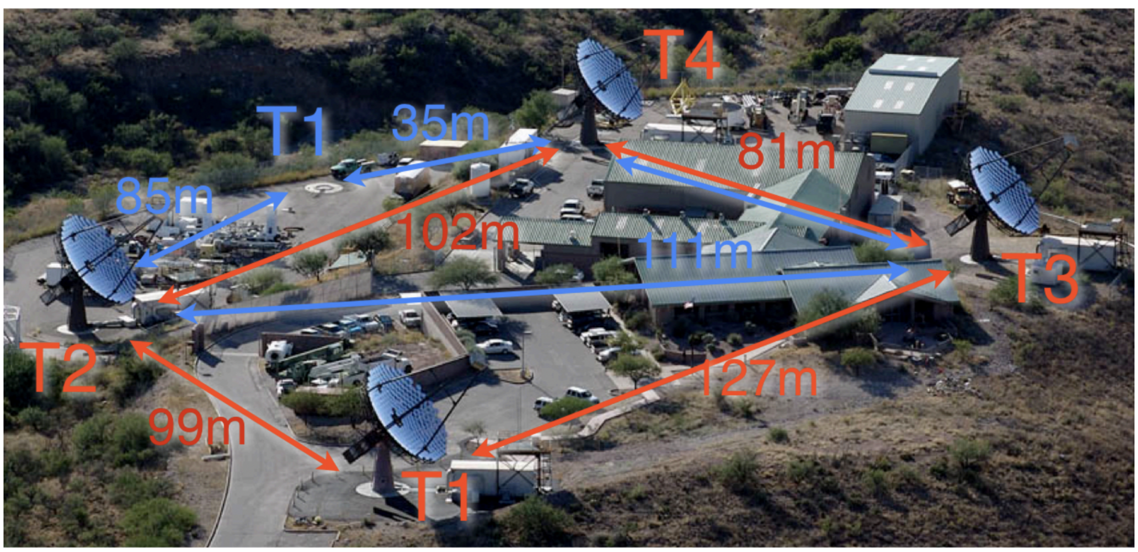

Figure 2.6: VERITAS array configuration for V5 and V6 epochs. From [68].

night sky background (NSB). The camera's zenith angle is the angle from zenith (directly overhead), with large zenith angles meaning that the camera is pointed closer to the horizon. Large zenith angles mean that there is more atmosphere between the shower origin and the camera, leading to absorption of Cherenkov light by atmospheric particles. Large offsets from the camera centre tend to truncate large shower images and lead to the misconstruction of these images as smaller showers, implying lower energy gamma-rays (see Figure 2.7b). Finally, NSB is the collection of light from the dark sky, amplified by light pollution and terrestrial transients, such as meteors. NSB is especially bright when reflected by clouds or atmospheric molecules. This causes an overall increase in PMT currents, making it hard to distinguish dim, low energy showers from the base current levels (see Figure 2.7a).

2.2.5 Monte Carlo Simulations

In order to determine the true direction and energy of reconstructed γ-rays, it is important to understand how the response function of the instrument interacts with the analysis techniques described in Section 3.1. Monte Carlo simulations are used to simulate air showers originating from γ-rays across the VHE spectrum at a range of different elevations (to account for airmass) and azimuths (to account for geomagnetic fields).

Effective Area

The effective area of the instrument is a way of representing its γ-ray sensitivity. This area is based on the area of the Cherenkov light pool, rather than the mirror area (which is typically the case for optical telescopes) and represents the maximum size of light pools that can be accurately reconstructed. The effective area is energy dependent at low energies and asymptotes at the true size of the light pool at approximately 1 TeV (see Figure 2.8). Small showers from low energy photons usually do not pass the L2 trigger, reducing the effective area, but since the Cherenkov shower is visible from anywhere within the light pool, the effective area is large for showers that pass trigger criteria.

Additionally, the zenith angle at which sources are observed also affects the effective area, as seen in Figure 2.9. Atmospheric molecules attenuate Cherenkov light more when they travel through more atmosphere, which is true at large zenith angles (low elevation). This preferentially affects lower energy photons, whose showers are already dim, leading to a higher energy threshold and typically lower sensitivity for VHE sources.

To determine the effective area, Monte Carlo simulations of γ-ray air showers with a Crab-like spectral index ($\Gamma = 2$) are generated. Using the trigger system described in Section 2.2.3, it is determined how many of these events pass all the way through the trigger system and analysis pipeline. This number is compared to the initial number of simulated events using Eq. 2.3 to determine the array's effective area. The effective area is defined as

$$A(E) = A_0 \left(\frac{\text{Number of events passing selection at energy E}}{\text{Number of events simulated at energy E}} \right), \tag{2.3}$$

where A_0 is the area of the Cherenkov light pool on the ground.

During the analysis stage, additional considerations are needed to accurately determine the effective area. These will be discussed in Section 3.1.4.

Angular Resolution

Angular resolution of IACTs is determined by the ability of the telescope to accurately determine the direction of origin of a γ-ray from its image. This is also determined by comparing Monte Carlo simulated showers originating from different directions and with the reconstructed direction (see Section 3.1.5). Around 1 TeV, the angular region containing 68% of simulated γ-ray events is less than $0.1°$. This can be improved upon by using more specialized analysis techniques. VERITAS' angular resolution as a function of energy is shown in Figure 2.10.

2.3 The VERITAS Enhanced Current Monitor (ECM)

The Enhanced Current Monitor (ECM) is a parasitic back-end added to all four telescopes to provide rapid optical photometry capabilities in selected pixels, without interrupting γ-ray observations.

The ECM consists of four DATAQ DI-710 data loggers, with one back-end per telescope. The ECM is attached to several PMT pixels (each called a channel), and reads the voltage output from each PMT at a user-defined rate. Unlike the γ-ray back-end, which only records data when triggered, the ECM monitors PMT voltage at constant intervals during a run. This allows for optical photometry to be performed by converting the voltage changes in each active channel to an optical magnitude. These observations are unfiltered, but due to the sensitivity of the PMTs lying in an optical wavelength sensitive to blue Cherenkov light (see Figure 2.11), the band monitored by the ECM lies within the Johnson-Cousins B and U bands [72].

The ECM has several gain modes, which affect the voltage at which the ECM saturates, as well as the digitization levels of the signal. For this work gain modes G10 and G100 are used. G10 is sensitive between ± 1 V and has has a digitization of ± 122 μV. G100 is the default mode that is used for ECM data taking and is sensitive between ± 100 mV and has has a digitization of ± 12.2 μV.

In principle, the device should sample at a maximum rate of 4800 Hz divided amongst the active channels. Throughout the analysis conducted for this work, it became apparent that the ECM was not truly capable of attaining rates higher than 1200 Hz, giving a minimum time resolution of 0.83 ms. This issue was identified while taking calibration observations of the Crab pulsar (P = 0.0338 s [73][2]). When the sampling frequency was increased from 1200 Hz to 2400 Hz to 4800 Hz at a fixed gain (G100), no notable increase was seen in detection significance (see Figure 5.9), with most variation likely originating from night sky background fluctuations.

Furthermore, analyses using the same run with sampling rate 4800 Hz that cut out every second data point, then every fourth, etc., to mimic lower sampling rates yielded no increase to detection significance at sampling rates $>$ 1200 Hz (see Figure 2.12).

The cause of the inability of the ECM to sample at high rates appears to come from a settling time in the instrument, in which the device's amplifier has not sufficiently settled before the data is digitized, meaning that individual voltage readings still contain some residual voltage from the previous reading (private communication with manufacturer).

[2] http://www.jb.man.ac.uk/ pulsar/crab.html

Tests are still ongoing to determine exactly where the settling time originates, and how the settling time can be resolved to enable faster sampling rates. This will be discussed further in Section 5.2.3.

2.3.1 ECM Flux Calibration

The ECM is calibrated annually by taking photometric observations of stars with known magnitudes. An annual calibration is all that is possible due to observing time being competitive. We use stars from Gaia DR3 [74, 75] with visual B-band magnitudes from roughly $m_B = 9$ to $m_B = 11$ and record the ECM voltage values during these observations to obtain the calibration curve shown in Figure 2.13. The voltage (vertical) uncertainties in Figure 2.13 are not well understood, but the scatter of these data are indicative of these uncertainties.

The conversion between ECM voltage and visual magnitude is the best-fit of the stellar data points in Figure 2.13, which gives the reltaion

$$m_{ECM} = \frac{log|V_{ECM}| - 2.27458167}{-0.40355447} \pm 1, \tag{2.4}$$

where V_{ECM} is the ECM voltage of the source (primary peak phase-folded voltage for pulsars) and ± 1 is the uncertainty on the calibration curve fit. Note that since the ECM is unfiltered, $m_{ECM} \neq m_B$.

The instruments described in this chapter will be used in this thesis to collect data on the Crab pulsar and PSR B1937+21. The data collected for this work and both the optical and γ-ray analyses of these data are discussed in Chapter 5.

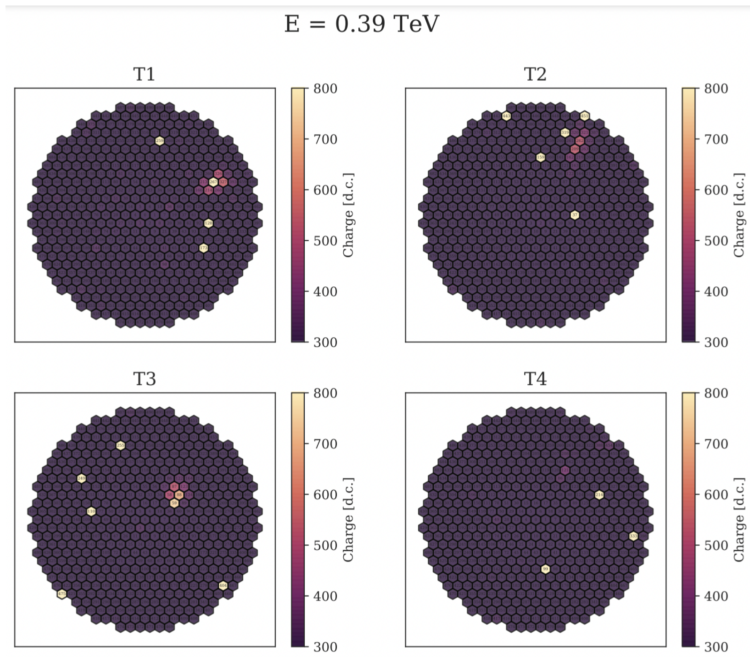

(a)

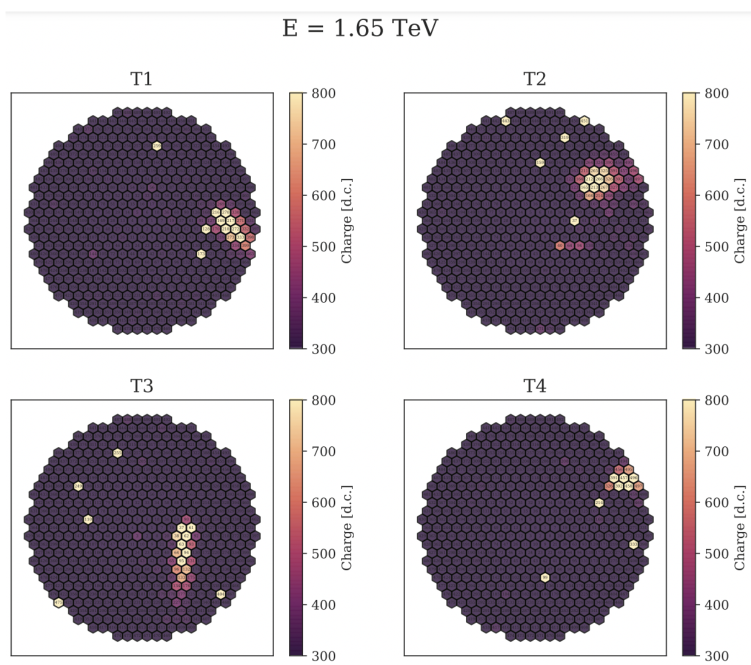

(b)

Figure 2.7: Examples of a small shower (a) and large shower (b) reconstructed as 0.39 TeV and 1.65 TeV γ-rays by the Eventdisplay package, respectively. Isolated yellow-coloured pixels correspond to either bright stars or pixels that are stuck on.

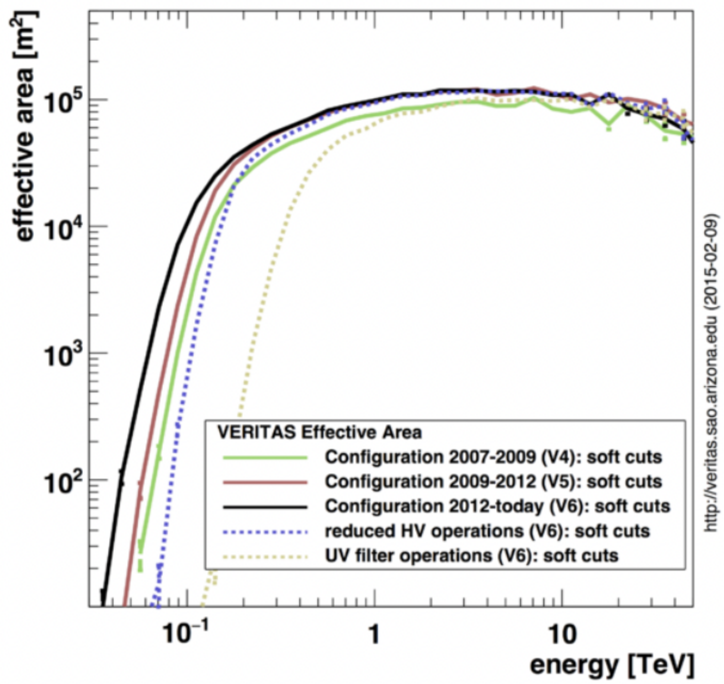

Figure 2.8: VERITAS effective area for photons of energies between 10 GeV and 100 TeV at an elevation of 70 degrees for all three VERITAS epochs. Reduced high voltage (RHV) and UV filter observations for operations during bright moon phases are also included. From [69].

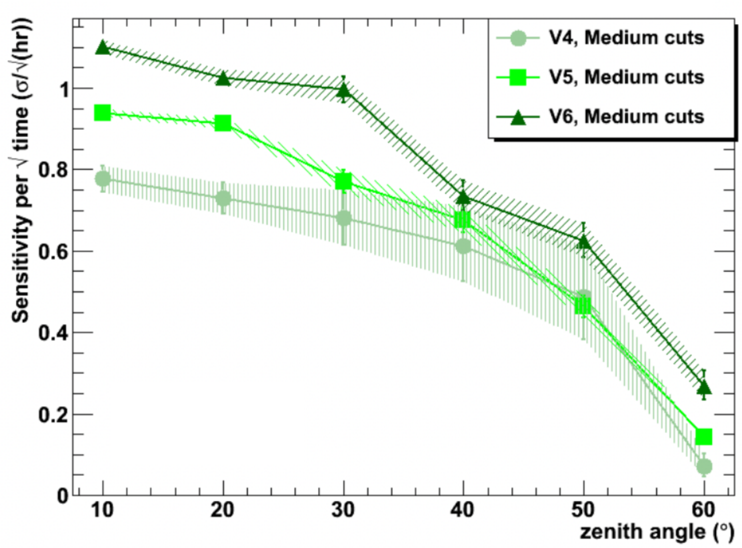

Figure 2.9: Sensitivity to a 1% Crab flux source analyzed with medium cuts (see Table 3.2), as a function of zenith angle for all VERITAS epochs. Here, sensitivity is given as a fraction of the total expected Li & Ma [70] significance as a function of time. From [71].

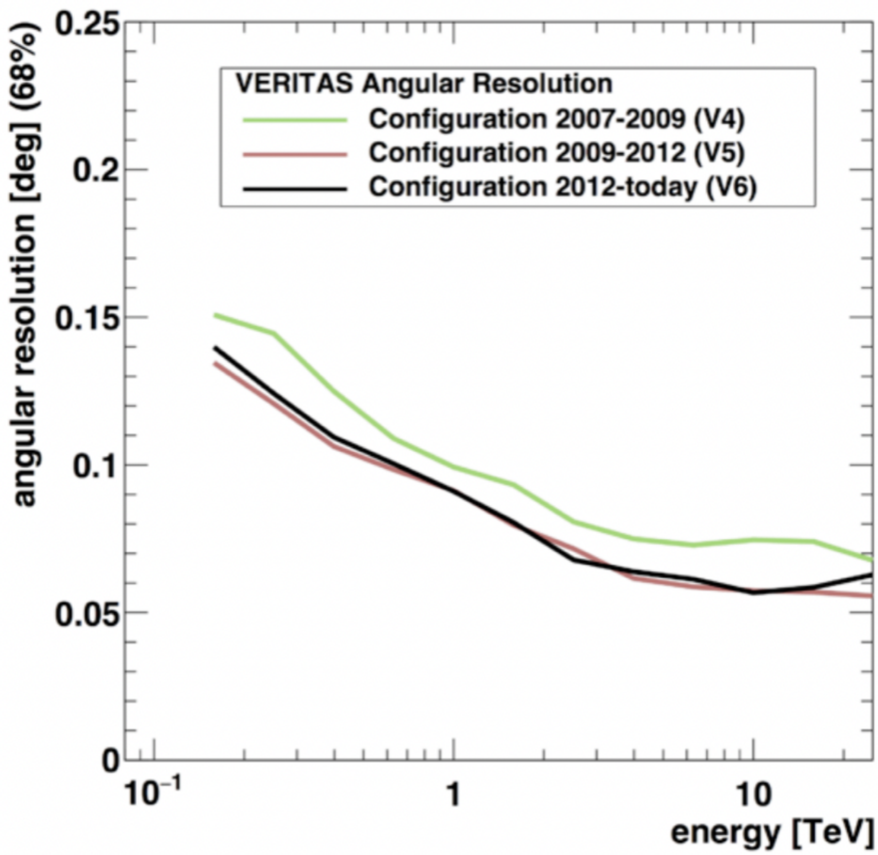

Figure 2.10: Angular resolution (68% containment of γ-ray events) as a function of energy for all three VERITAS epochs. From [71].

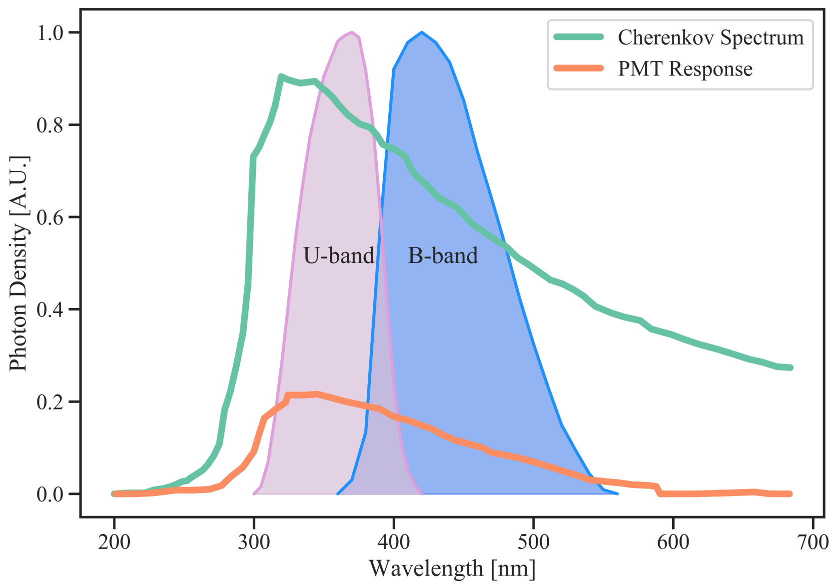

Figure 2.11: The Cherenkov spectrum after atmospheric absorption (green line) plotted with the PMT quantum efficiency (orange line). The Johnson-Cousins B and U bands are plotted to show the ECM response in each band. The PMT response shows the VERITAS sensitivity to the corresponding wavelength range. It can be seen that because the Cherenkov spectrum and PMT response peak in the U-band, this is the band that dominates VERITAS optical observations, though there is some sensitivity in the B-band as well.

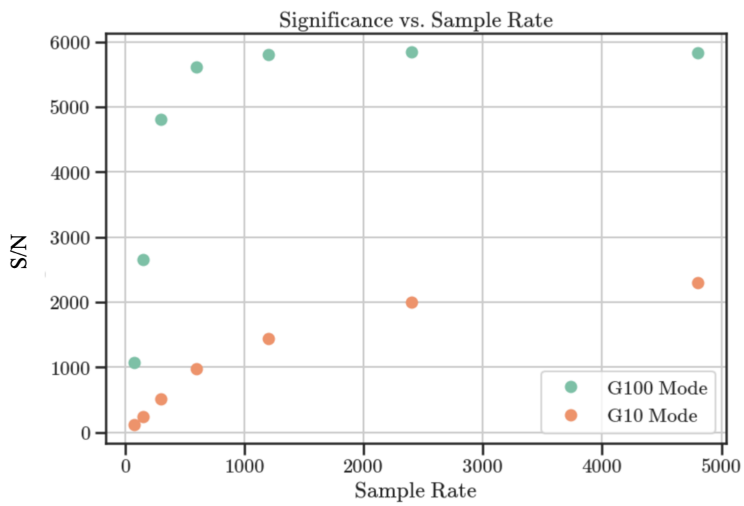

Figure 2.12: Significance (as a signal to noise ratio) for a single Crab run, removing every $2n$ datapoints for $1 \leq n \leq 7$. The significance is expected to increase, rather than flatten beyond ≈ 1200 Hz, so the behaviour of these data indicate that sampling at higher rates does not sample independent data points.

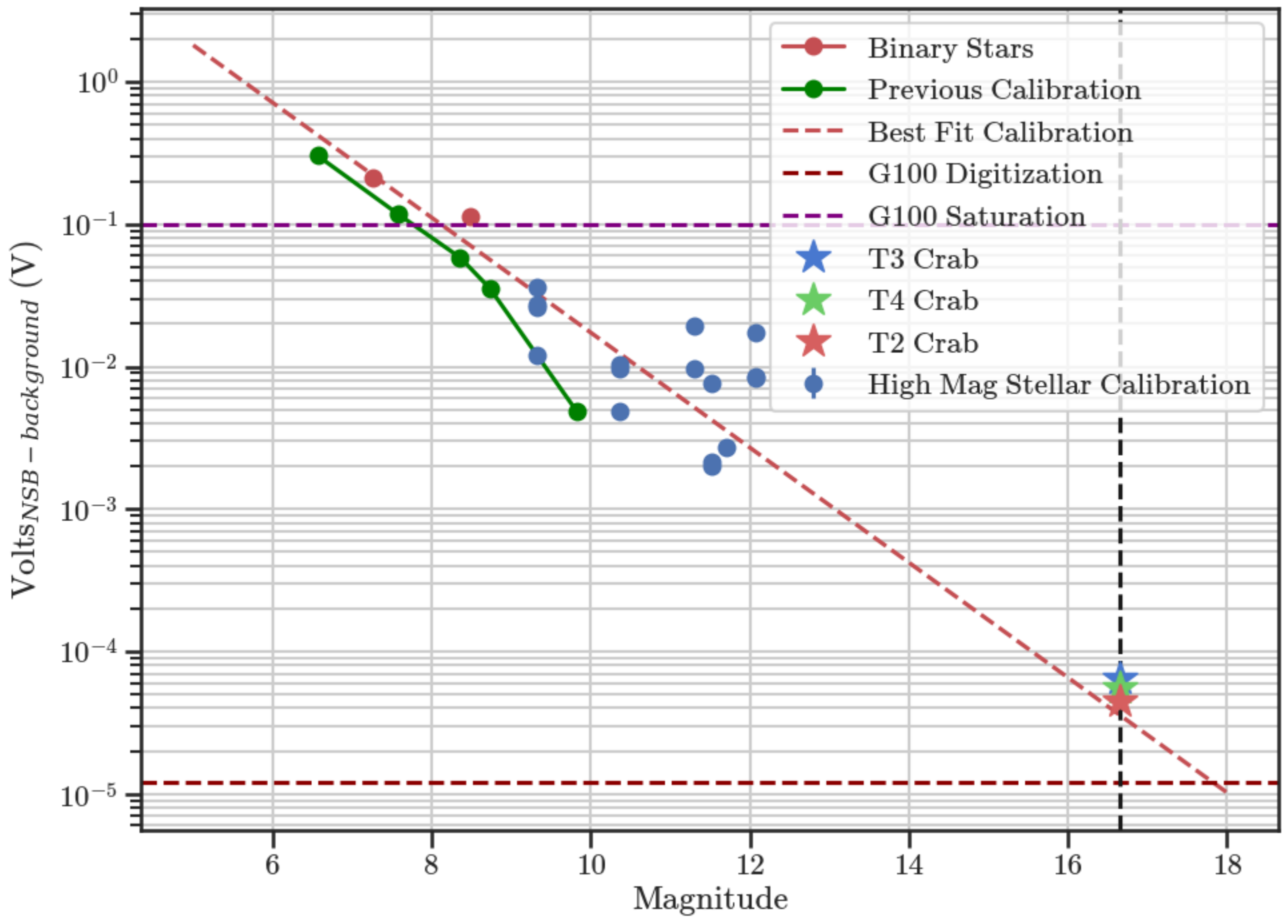

Figure 2.13: ECM calibration curve obtained from observations of stars and binaries of known B-band magnitude. The Crab pulsar calibration points are not used to obtain the curve.

Chapter 3

VERITAS Optical and γ-ray Analysis

3.1 Gamma-ray Analysis

Raw VERITAS data is exported from the telescopes in VERITAS Bank Format (VBF), binary files for every run containing information recorded for each event, including trigger information, event time, pixel voltage values, and telescope positions, among other information that will be used to reconstruct the event that initiated the air shower. All analysis and reconstruction is done with one of two analysis packages: Eventdisplay [76] or VEGAS [77]. Both packages look at each saved event in the VBF file and use the geometry of the camera image to reject background and reconstruct the energy and direction of γ-ray candidate events to determine the overall significance of γ-rays over background, as well as the flux and spectrum of the observed γ-rays. If a significant excess is found at the source location, both packages should agree that that excess rules out the null hypothesis that the excess originates from a background fluctuation at the 5σ level. Both packages have slightly different methods for event selection and parameterization, so a cross-check of analysis methods is necessary to ensure that an observed excess of events is not due to systematic effects in either package. For this work, only Eventdisplay will be used for VHE γ-ray analysis. A VEGAS analysis will be necessary to validate the results of this work, if this work is presented in a conference or publication.

Eventdisplay is comprised of three stages, `evndisp`, `mscw energy`, and `anasum`. These steps are discussed thoroughly throughout the next sections and outlined briefly as follows:

1. `evndisp`: calibrates the relative gain and timing within each telescope's pixels, removes pixels that do not contribute to triggered events, and reconstructs the core of the shower and the direction of the event.

2. `mscw energy`: parameterizes shower images using the Hillas parameters (see Section 3.4) and uses lookup tables to calculate scaled length/width parameters (see Section 3.1.3), which will be used in the `anasum` step. The reconstructed energy of each event is obtained by using lookup tables.

3. `anasum`: rejects events that are classified as hadrons (charged cosmic rays), estimates the number of events expected in background regions, and estimates the significance that an excess at the source location is not occurring due to a background fluctuation.

After all of the above steps are complete, high level data products, such as lightcurves (flux as a function of time), spectra (flux as a function of energy), and sky maps (significance at each spatial location) may be extracted for further studies.

Eventdisplay consists of the following stages that, together, provide a full data analysis for the VHE γ-ray data. The flow of these steps is briefly outlined in Figure 3.1.

3.1.1 Calibration

Evendisplay starts by running `evndisp`, which calibrates each run, integrates the FADC trace of each pixel (see Figure 3.2), and finally cleans each event image to retain only the shower information.

Every night that data is taken, the PMT relative gain and timing are monitored using a flasher system. For each telescope, the flasher system consists of a flashlight of seven

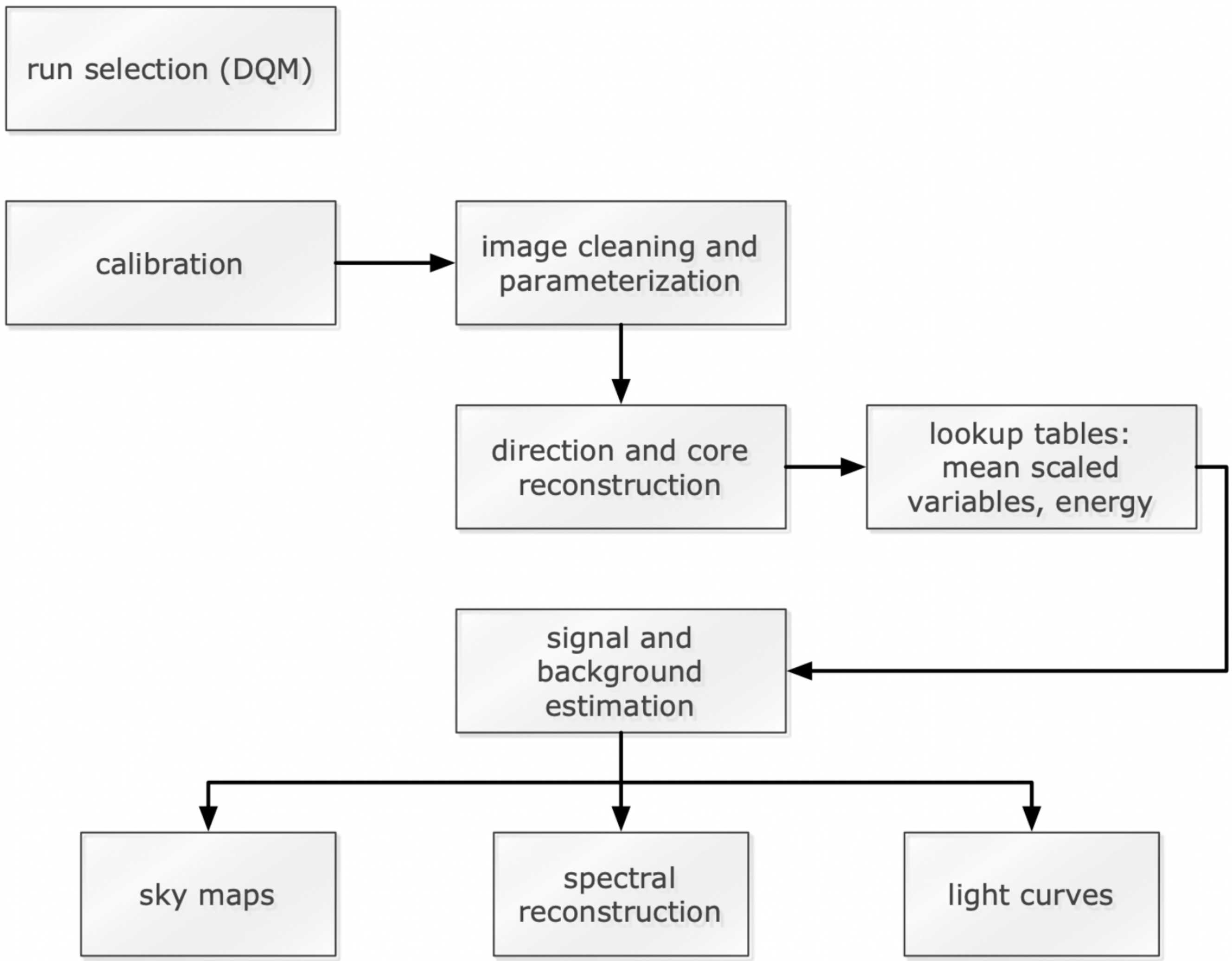

Figure 3.1: Flowchart of the Eventdisplay analysis stages. Credit: Gernot Maier.

blue Optek OVLGB0C6B9 LEDs with a peak wavelength of 465 nm. The flashers pulse at a rate of 300 Hz for two minutes, stepping through eight different light levels. The response of the PMT at each level can be calculated to give a relative gain value. Since all 499 camera pixels are flashed uniformly, any relative time delays between pixels is also measured. This means that any measured time delays after calibrating with the flasher run are intrinsic to the shower physics.

Eventdisplay begins by analyzing the flasher run to calculate relative gain and timing differences as well as the relative calculation between high and low gain modes of the FADC. Pedestal events are forced triggers recorded at a 3 Hz sampling rate that are

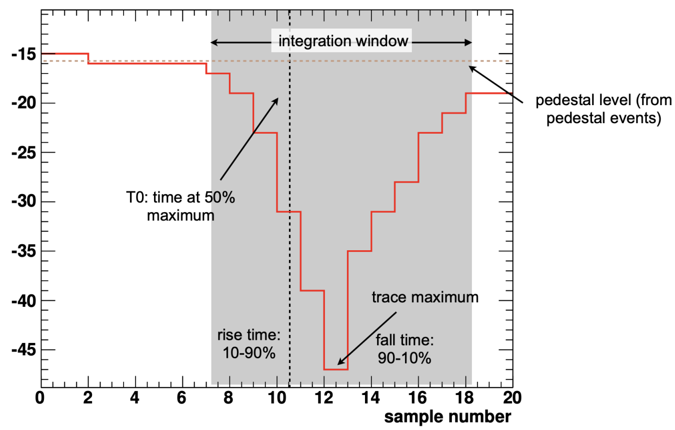

Figure 3.2: An example of an FADC trace showing a Cherenkov pulse. The relevant quantities are labelled. The size parameter is the integral of the pulse over the grey window and is related to the original γ-ray energy. Credit: Gernot Maier.

meant to record the variance in the FADC trace due to night sky background (NSB) and electronic noise (see Figure 3.3). Statistically, Cherenkov pulses will occur during pedestal triggers $\approx 0.3\%$ of the time, which is relatively unimportant, since the mean pedestal value is used. Eventdisplay use pedestal mean and variance to determine the baseline at which to integrate the total charge in each pixel's trace. At this stage, other information that may affect analysis outcomes such as the removal of dead pixels, corrections for the array geometry, and correction for dead time (when the telescope is insensitive while reading out data) are all accounted for.

3.1.2 Image Cleaning

Since not all pixels contribute to the shower image that has caused the telescope to trigger, un-associated pixels must be cleaned out before the image is parameterized. The majority of the pixels are "noise pixels", whose voltage value is due to the NSB. Other pixels may be bright due to being pointed at stars, meteors, terrestrial light, or are stuck on at a given voltage value. All of these are removed using the following cuts:

- The integrated charge in any pixel must be greater than $pedestal + 5 \times pedvar$, where $pedestal$ is the pedestal value and $pedvar$ is the pedestal variance.

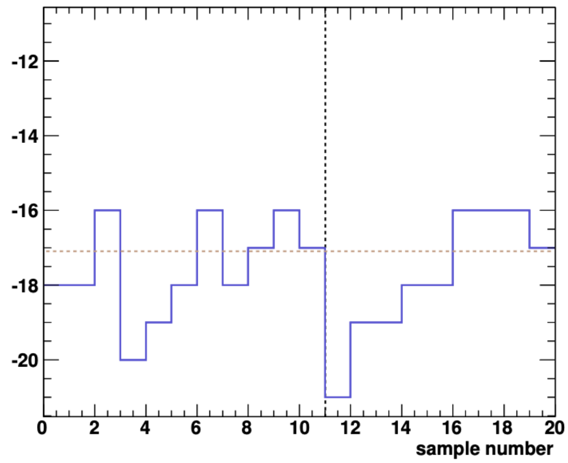

Figure 3.3: Example of the FADC trace for a pedestal event. The dashed red line is the mean, also known as the pedestal value. The black dotted line corresponds to T0, the time at 50% peak maximum. Pedestal variance is calculated as the variance of this trace.

- An image must consist of at least four adjacent pixels that pass the above cut.
- Pixels neighbouring the image are selected if they have an integrated charge greater than $pedestal + 2.5 \times pedvar$.
- At most 20% of the total image charge can be contained in border pixels that are located at the edge of the camera. Showers that mostly fall outside of the camera's field of view are typically poorly reconstructed.
- The above cuts must be passed in at least 2 telescopes in order to reject muon showers and NSB fluctuations from being reconstructed as γ-ray air shower events.

3.1.3 Image Parameterization

Shower images are approximately elliptical in shape and can be parameterized using Hillas parameters [78], a set of geometric parameters that describe the morphology of shower images. These parameters are used for energy reconstruction (Section 3.1.4), directional reconstruction (Section 3.1.5) and γ-hadron separation (Section 3.1.7). The Hillas parameters that are important for γ-ray reconstruction are listed in Table 3.1 and illustrated in Figure 3.4.

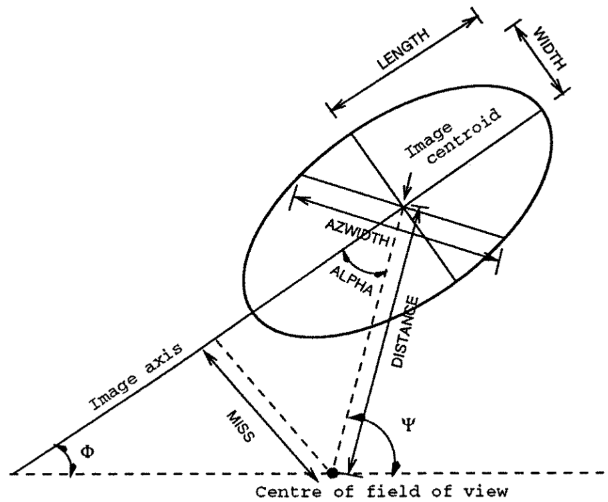

Figure 3.4: Hillas parameters for a shower image [78]. The parameters used for Eventdisplay analysis are length, width, image axis, alpha, image centroid, and distance.

It is also important to consider where the shower fell with regard to the telescopes while using these parameters. Closer showers will appear brighter and larger, but do not necessarily come from higher energy γ-rays. To mitigate this, lookup tables are constructed with Monte Carlo simulated showers of known energies, thrown at various distances from the camera.

Scaled width (SW) and scaled length (SL) parameters are used for γ/hadron separation (see Section 3.1.6) and are derived from these lookup tables. SW is defined as

$$SW = \frac{w(S, D)}{< \hat{w}(S, D) >}, \tag{3.1}$$

and SL is defined as

$$SL = \frac{l(S, D)}{< \hat{l}(S, D) >}, \tag{3.2}$$

Parameter	Definition	Purpose
Size	The total pedestal-corrected integrated charge across all pixels retained after image cleaning and cuts.	Quantifies the shower brightness and is used for energy reconstruction.
Length	The standard deviation of the charge distributed along the semi-major axis of the image.	Used for γ/hadron separation.
Width	The standard deviation of the charge distributed along the semi-minor axis of the image.	Used for γ/hadron separation.
α	The angular mis-alignment between the image axis and the vector connecting the image centroid to the camera center.	Used for directional reconstruction.
Image axis	points in the direction of the shower core	Used for directional reconstruction.
Image centroid	The geometric center of the ellipse	Used for calculating other parameters, such as distance and α.
Distance	The distance of the image centroid from the camera center	Used for cutting truncated events.

Table 3.1: The main Hillas parameters used by Eventdisplay.

where w is the width of the image, l is the length of the image. $\hat{w}$ and $\hat{l}$ are the mean of the simulated image widths and lengths, respectively, S is the image size and D is the shower core distance.

For stereoscopic observations, these parameters are averaged across all n telescopes, such that

$$MSCW = \frac{1}{n}\left(\sum_{i}^{n} \frac{SW_i - \hat{w}(S,D)}{\sigma_{width,MC}(S,D)}\right), \tag{3.3}$$

and

$$MSCL = \frac{1}{n}\left(\sum_{i}^{n} \frac{SL_i - \hat{l}(S,D)}{\sigma_{length,MC}(S,D)}\right), \tag{3.4}$$

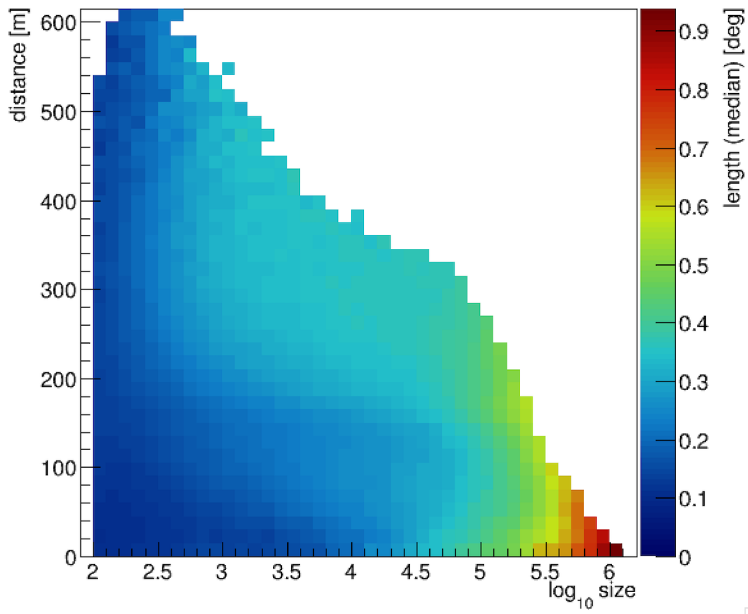

Figure 3.5: Example lookup table for mean scaled length (MSCL). After image parameterization and directional reconstruction (see Section 3.1.5), the image size and the distance of the shower core from the telescope can be obtained. These values are used in the lookup table to find their corresponding MSCL value.

where $\sigma_{width,MC}$ and $\sigma_{length,MC}$ are the uncertainties on simulated image widths and lengths, respectively.

3.1.4 Energy Reconstruction

The γ-ray energy is reconstructed by comparing the image geometry with lookup tables that consist of parameters of simulated showers with known initial energy (see Figure 3.7. The two parameters that are important for reconstructing energy are core distance and image size.

There are uncertainties in energy reconstruction that cause the reconstructed energy of a γ-ray to be smeared in an approximately Gaussian distribution around the true energy known from simulations. This is represented by the energy migration matrix (see Figure 3.8), which shows the distribution of reconstructed energies for a given true energy. This

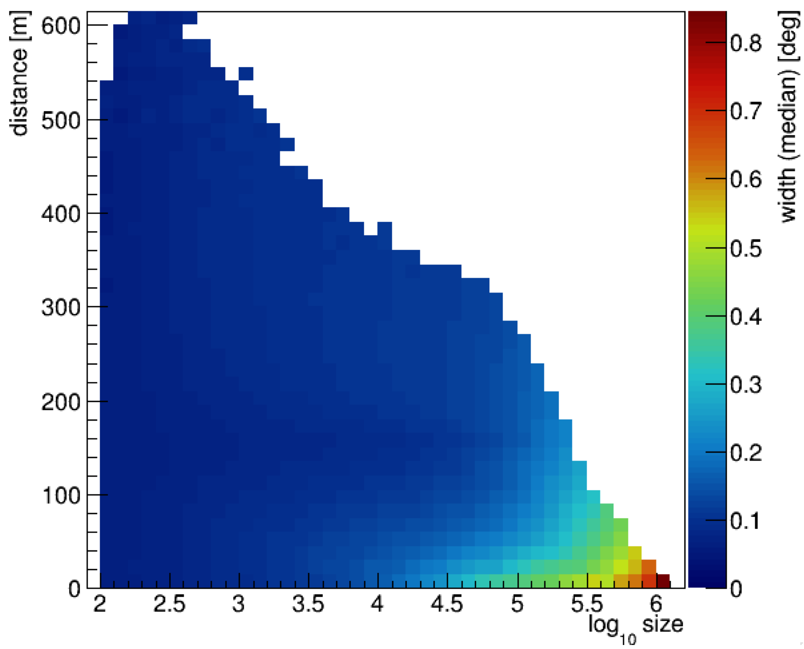

Figure 3.6: Example lookup table for mean scaled width (MSCW). This table works similarly to Figure 3.5, but the value obtained from the lookup table is MSCW.

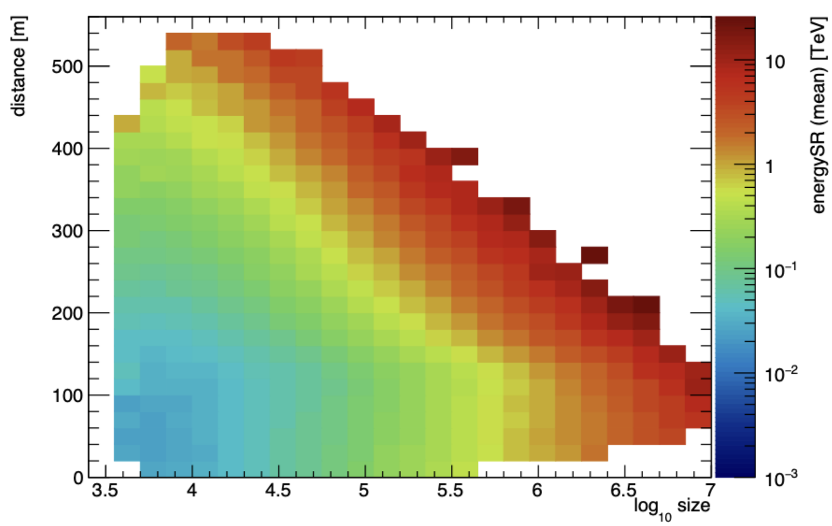

Figure 3.7: Lookup table for energy estimation. Similar to the MSCW and MSCL tables, reconstructed distance and size are used to obtain a reconstructed energy value (energySR).

is used to quantify the uncertainty on reconstructed energies. Again, the energy bias is most prominent for low energy γ-rays, because smaller showers have the largest uncertainties.

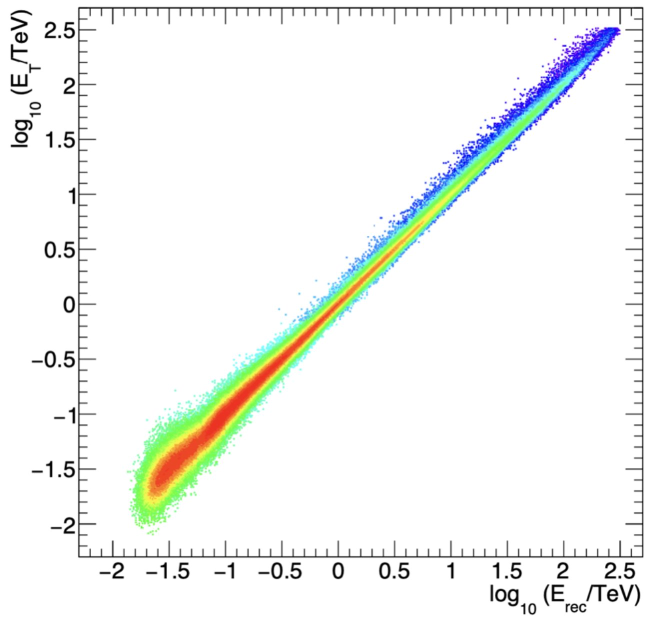

Figure 3.8: Energy migration matrix. The reconstructed energy, E_{rec}, is input into the matrix to obtain a distribution of true energy, E_T, as determined from simulations. This distribution corresponds to a cross-section of the matrix at E_{rec}. The most likely energy value is the peak of the distribution, with uncertainties calculated from the width of the distribution.

3.1.5 Directional Reconstruction

The core of the shower, which points back to the position of the original γ-ray, can be reconstructed stereoscopically. The shower axis corresponds to the direction of the semi-major axis of the reconstructed ellipse. (see Figure 3.4). Since each shower axis should point to the shower core, minimizing the point of intersection between the image axes of multiple telescopes should give an improved estimate over any individual telescope (see Figure 3.9).

In reality, these axes do not intersect at a single point. To correct for different points of intersection and find the "true" shower core, weights are assigned to each shower

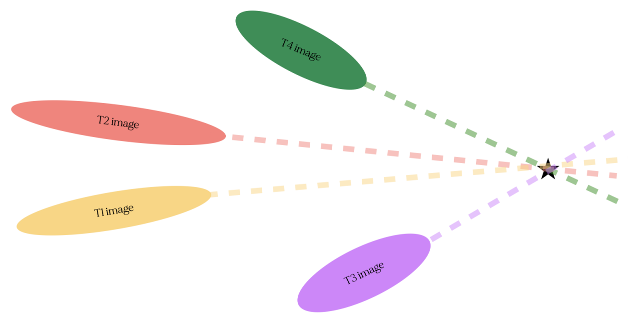

Figure 3.9: An example of directional reconstruction for the VERITAS array. The black star represents the reconstructed source location.

that more heavily weight showers likely to better localize the shower center. Eq. 3.5 describes the function used to weight images by telescope pair. S is the image size, w is the image width (semi-minor axis), l is the image length (semi-major axis), and θ is the angle between the two image axes. Larger sizes and more elliptical shapes are most heavily weighted, as their axis will point to the shower core with more accuracy than smaller, rounder images that are likely not as well parameterized. The weights are given by

$$W = \left(\frac{1}{S_1} + \frac{1}{S_2}\right)^{-1} \times \left(\frac{w_1}{l_1} + \frac{w_2}{l_2}\right)^{-1} \times sin(\theta_{12}). \tag{3.5}$$

Directional reconstruction can be further improved by using boosted decision trees (BDTs) to select the optimal source direction.

3.1.6 Event Rejection and γ/Hadron Separation

Following the paramaterization of each image, further selection cuts are made to only include events that can be reconstructed accurately:

Core distance cut: Images with large distances ($>$ 250 m away from the telescope) lead to poor directional reconstruction of the event and are rejected.

Cut	Spectral Index	Energy Threshold	θ^2 [deg^2]	MSCW	MSCL	SizeSecondMax (SSM) [direct charge]	Emission Height (h) [cm]
Supersoft	> 3	As low as possible	< 0.012	$-1.2 <$ MSCW < 0.3	$-1.2 <$ MSCL < 0.5	$0 <$ SSM $< 10^{30}$	$6 < h < 10^{10}$
Soft	≈ 3	≈ 120 GeV	< 0.008	$-2 <$ MSCW < 2	$-2 <$ MSCL < 5	$0 <$ SSM $< 10^{30}$	$< 10^{10}$
Moderate	≈ 2.4	≈ 250 GeV	< 0.008	$-2 <$ MSCW < 2	$-2 <$ MSCL < 5	$400 <$ SSM $< 10^{30}$	$< 10^{10}$
Hard	> 2.4	≈ 450 GeV	< 0.008	$-2 <$ MSCW < 2	$-2 <$ MSCL < 5	$1.5 \times 10^3 <$ SSM $< 10^{30}$	$< 10^{12}$

Table 3.2: The standard cuts used in Eventdisplay analysis. Cut thresholds are determined by comparing the distributions of these parameters for both simulated protons and photons and optimizing the signal (photon) to noise (proton) ratio.

θ^2 **cut**: θ is the angular distance between the reconstructed shower arrival direction and the source location (which is squared to give a one-sided distribution). Images with large θ^2 values are not likely to come from the source of interest and are more likely to be from cosmic ray or background photon showers.

Loss: Loss is quantified as the percentage of the image that is contributed by pixels at the edge of the camera. Images with large loss percentages are not well contained in the camera and will be poorly reconstructed.

MSCW and MSCL cuts are important for γ/hadron separation, because γ-rays and cosmic rays show different distributions of these parameters (see figure 3.10). Since the γ-ray distributions are peaked at smaller MSCW and MSCL values, the standard cuts outlined above will reject a large quantity of cosmic ray showers.

Eventdisplay has a standard list of cuts that are used for most analyses. The cut set that should be used depends on the source's spectral index. The standard cuts are outlined in Table 3.2.

The main differences between the cuts in Table 3.2 cuts are the *SecondSizeMax* parameter, which corresponds to the size of the second brightest event image and the shower emission height, which are both energy dependent. For cut types (besides supersoft, where the objective is to save the maximum number of events possible), γ/hadron cuts on MSCW and MSCL are cut on the same values, since these only depend on the shower geometry and are not strongly energy dependent. In addition, θ^2 for all cuts (besides supersoft) is set to $\theta^2 < 0.008$ for point sources but must be increased if the source is known to be extended.

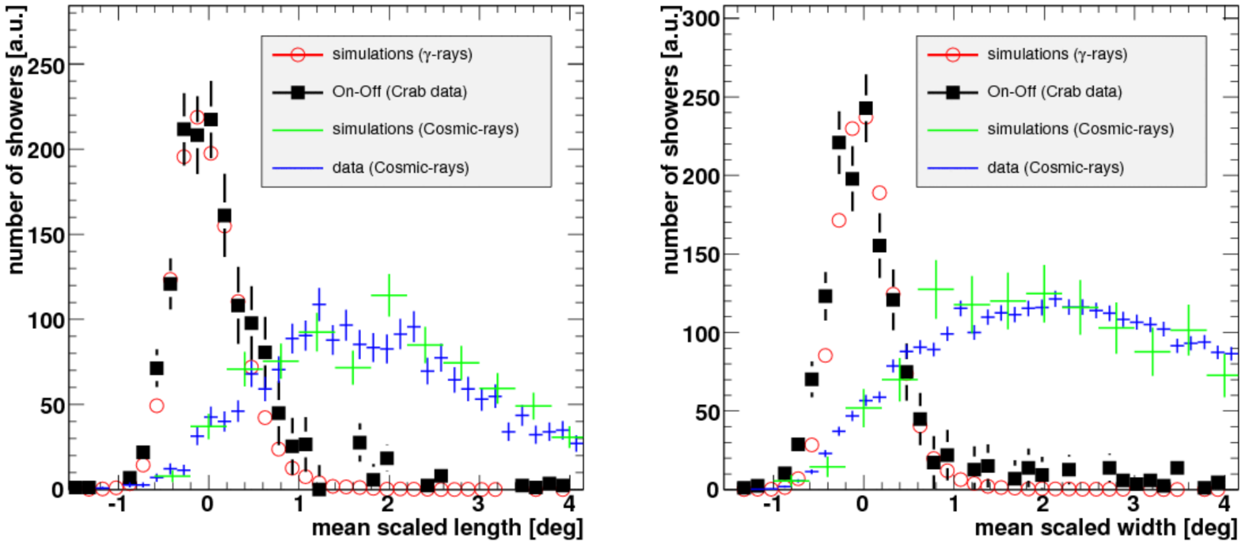

Figure 3.10: MSCL (left) and MSCW (right) distributions for both γ-rays and cosmic rays.

3.1.7 Background Estimation

Even after the cuts discussed in section 3.1.6, there still exists an irreducible background of events coming from the diffuse γ-ray background (which is believed to be small) and from π^0 (neutral pion) showers that originate in cosmic ray showers. π^0 particles decay into photons that will produce their own showers, which are indistinguishable from low energy γ-ray showers.

In order to account for these irreducible backgrounds, the number of background counts is estimated by looking at off-source background regions. As will be discussed in Section 3.1.8, the significance at which the source photons are found to be in excess of the background is calculated by comparing photon counts in both the source and background regions.

For a point source (any source smaller than the point spread function (PSF; $0.15°$) of VERITAS), there are two background methods that are part of the standard analysis. Both of these background methods take advantage of the large VERITAS FoV ($3.5°$) by using regions away from the source as background. This is advantageous because the background region will have sufficiently similar characteristics to the source region, such

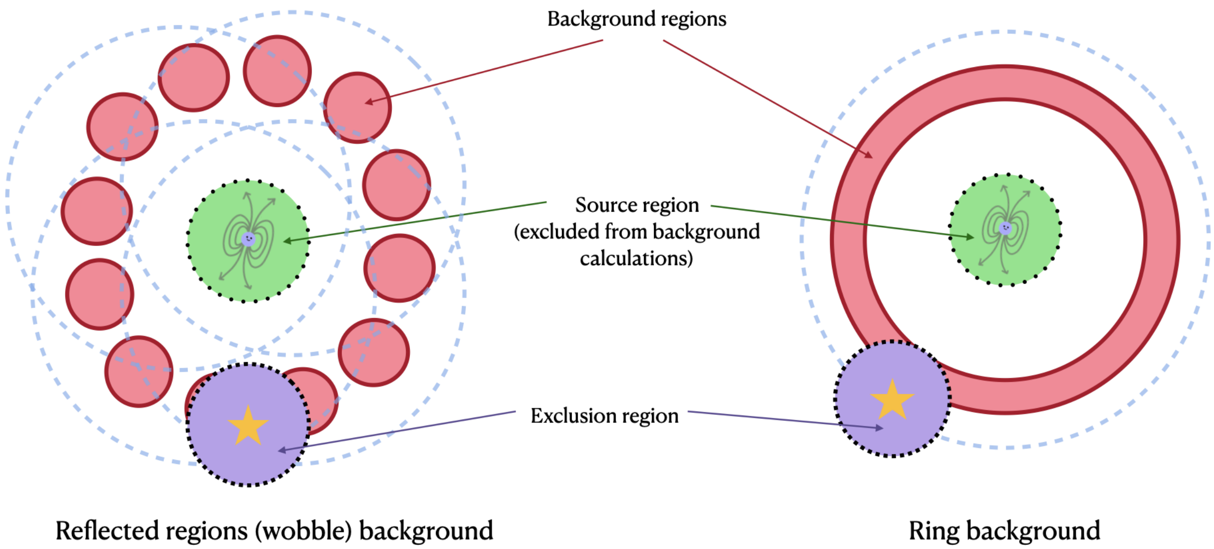

Figure 3.11: Background regions for the reflected region (*wobble*) method (left) and ring background method (right). The light blue dashed circles approximately show the VERITAS FoV with respect to the source and background regions.

as zenith angle, azimuth, and NSB levels, all of which affect count rates, as described in Sections 2.2.4 and 2.2.5. For both background methods, bright stars and nearby known γ-ray sources are masked from the background region so that background γ-ray rates are not contaminated with regions that may contain excess counts.

Standard VERITAS observations are taken in *wobble* mode, where the telescopes are pointed at an offset (typically 0.5°) from the expected source location. *Wobble* observations are taken in the four cardinal directions (North, South, East, and West), where the direction is changed for each subsequent observation (there is no pre-defined time interval for the changing direction and subsequent observations can be anywhere from minutes to years apart). However, the significance of a given run is calculated with the reflected regions contained in the observation, so inconsistent observation cadences do not cause systematic uncertainties. The full picture of observations taken in all four cardinal directions allows for background regions to be created around the source, as shown in Figure 3.11.

For observations taken with the ECM, *wobble* observations are not possible since the pixel connected to the ECM (usually the central pixel) must remain on-source throughout each data taking run. Instead, *tracking* observations are used, where all observations are taken with the source at the center of the camera. To calculate background for these observations, a ring background method (RBM) is used (see Figure 3.11). For RBM, radial acceptances must be generated to determine corrective factors that are applied to the rates of events falling away from the camera center, since background regions are not equidistant from the camera center as with *wobble* observations.

3.1.8 Significance Calculations

Constant Emission (Nebula)

The significance of any excess found with Eventdisplay is derived in [70] and is defined as the probability that the excess γ-ray counts are due to the source and not background fluctuations, once all known systematic uncertainties are removed. The statistical significance of an observed excess of events can be derived as shown in Eq. 17 of [70], based on that N_{on} and N_{off} are independent, poisson-varying quantities. Eq. 17 of [70] is given by

$$S = \sqrt{2\ln\lambda} = \sqrt{2}\left\{N_{on}\ln\left[\frac{1+\alpha}{\alpha}\left(\frac{N_{on}}{N_{on}+N_{off}}\right)\right] + N_{off}\ln\left[(1+\alpha)\right] + N_{off}\ln\left[(1+\alpha)\left(\frac{N_{off}}{N_{on}+N_{off}}\right)\right]\right\}^{1/2}, \quad (3.6)$$

where S is the significance, in units of standard deviation, N_{on} is the number of counts in the source region, N_{off} is the number of background counts, and α is the ratio of the ON and OFF regions' sizes and exposure times, as illustrated in Figure 3.12.

A significance of five standard deviations from the mean (5σ) is generally accepted as a detection.

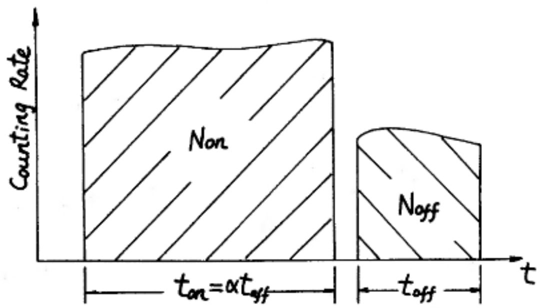

Figure 3.12: A cartoon illustrating the ON and OFF counts obtained during a single observation, as well as the α parameter that corresponds to the differences in physical ON and OFF region size as well as exposure time differences.

Pulsed Emission (Pulsar)

In order to explore the pulsed γ-ray signal (which is $\approx$ 1% of the flux of the PWN at $\approx$ 200 GeV), it is necessary to phase-fold the γ-ray counts obtained from Eventdisplay analysis. Phase folding assigns each event a phase, which is a fraction of the pulsar's period and bins the counts at each phase to obtain a pulse profile for a single period. In this work, Tempo2 [79] is used to perform the phase folding and barycentering of the γ-ray data. Barycentering converts event times to a frame at the center of the solar system, which corrects for the Earth's motion in the Solar System and allows pulse profiles from multiple observatories to be compared without issue of different photon arrival times to different locations on Earth. As will be discussed further in Section 5.2.2, the VHE Crab pulsar signal is very dim and long observation times are required to detect the interpulse ($\approx$ 50 hours) and the main pulse ($\approx$ 80 hours).

Since the locations of the pulsar's main pulse and interpulse are known for the Crab pulsar from previous VERITAS analyses [6], it is possible to search for an excess of counts in known phase intervals or "gates", where the pulses are expected to be contained. Other methods, such as the H-test [80] may be used if the ON and OFF regions are not known (i.e., for pulsars that have not yet been detected in VHE γ-rays), but are not used in this work.

The phase gate method is used in this work as follows:

1. The number of counts is extracted from the phase-folded data, which has already passed through the standard Eventdisplay analysis with soft cuts.
2. Phase gates for the peak regions and background regions are either determined from previous VHE work or from *Fermi*-LAT pulse profiles, if the HE and VHE γ-ray emission is believed to be in phase with each other.
3. The relative size (α) between the phase gates and the background regions is determined by $\alpha = N_{bins,on}/N_{bins,off}$.
4. Equation 3.6 is applied to both the main pulse and interpulse regions to determine a significance for each phase gate. If an individual peak exceeds 5σ, a pulsed signal has been detected in that phase gate.

3.2 Optical Analysis

The optical analysis package OOPS-E[1] was developed for this work. OOPS-E analyzes unprocessed ECM data and evaluates the significance of a pulsed signal at the pulsar's rotation period. Detection significance is the probability that a peak at the pulsar ephemeris in frequency space arises from the pulsed signal, rather than background noise. The analysis workflow is outlined in the steps below.

3.2.1 Data quality checks

Each ECM data file is assessed for data quality, applying a mask to cut effects such as bright events (typically meteors) that saturate the detector and large fluctuations in night sky background due to clouds from the data. Each telescope timeseries file for each run is checked to remove any runs with complete saturation or weather effects that render the data unusable. A typical ECM run can be seen in Figure 3.13.

[1] https://github.com/samanthalwong/OOPS-E

3.2.2 Cleaning Algorithm

Bright flashes appear as spikes scattered stochastically in all ECM data. These are thought to be meteors or other bright flashes of terrestrial origin (e.g., headlights, planes flying overhead, etc.). These spikes, along with NSB fluctuations (see Figure. 3.13), create low-frequency "red" noise in ECM data, which contaminates preferentially low-frequency signals, but can be spread over much of frequency space.

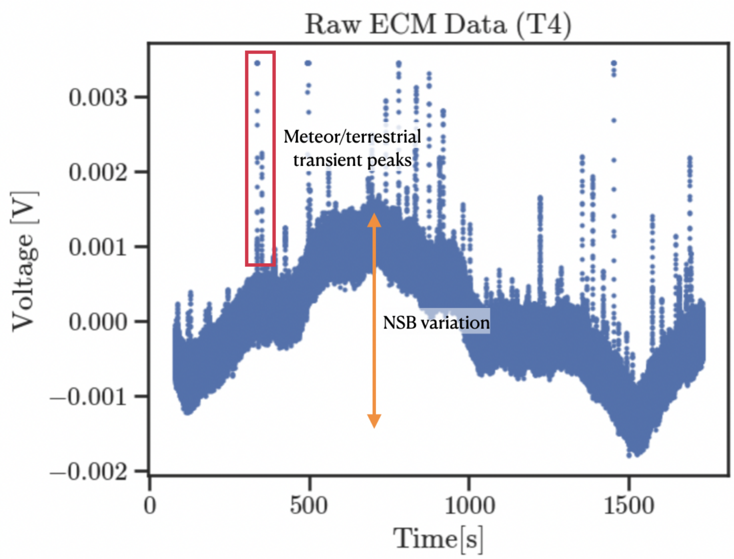

Figure 3.13: Single telescope ECM file showing meteor spikes and NSB variations, which both increase low-frequency noise.

In order to reduce the levels of noise seen in ECM frequency space analyses, a cleaning algorithm is applied to remove any large peaks, as well as NSB fluctuations. The algorithm first uses a spline interpolation (*scipy*'s interpolate.splrep [81] function) to model the shape of the ECM data (Figure. 3.14a), then evaluates the background spline model at $\approx 0.0001\%$ of the data points in order to best fit the NSB variations but avoid over-fitting to the meteor peaks. The residuals of the spline model with the original data give a "flattened" dataset (Figure. 3.14b), from which a median value can be computed in order to estimate the baseline NSB. Any peaks that fall outside a given width from the median are removed. The width chosen is typically 3σ from the median, but can be modified depending on how well the data is "flattened". The number of data points used for fitting and width from the median at which points are removed are both determined by optimizing the signal to noise ratio while varying both parameters. A flattened dataset with an amplitude corresponding to the NSB is returned (See Figure. 3.14 c). Note that the Crab pulsar signal (the brightest pulsar signal we expect to observe) peaks at a voltage $\approx 10^{-5}$ V. Peaks are removed at a voltage of $\approx 10^{-2}$ V, so the data are much lower in amplitude than the peaks that are being removed and apparent truncation of the data does not affect the pulsar signal.

3.2.3 Frequency domain analysis

Because the ECM data are dominated by the NSB and bright transients, it is helpful to perform any searches for a pulsed signal in frequency space. For this analysis, we use astropy's [82, 83, 84] Lomb-Scargle (L-S) periodogram [85, 86, 87], which has the advantage accurately transforming non-uniformly sampled data into frequency space, when compared to a Fourier transform. This is particularly useful, because L-S periodograms allows for masks to be applied to the data in the time domain, if time cuts are necessary due to poor data quality.

The L-S periodogram finds periodic signals by fitting a sinusoidal model to the data at each given frequency. It then assigns a power to each frequency based on how well the sinusoidal model fits the data. Better fits are assigned a higher power, and therefore represent a more likely periodic signal. The frequency grid and powers corresponding to each frequency are the two primary outputs obtained.

The L-S periodogram uses a frequency grid to determine the frequencies at which to calculate a power. For all pulsars with a period < 1s, the frequency grid is determined by the `autopower` method, which calculates a frequency grid appropriate to the number of data points between the pulse frequency $\pm$ 1. It is considered best practice to use `autopower` to generate the frequency grid to avoid situations where the pulsar frequency falls between grid values and is not detected. For pulsars with periods greater than the

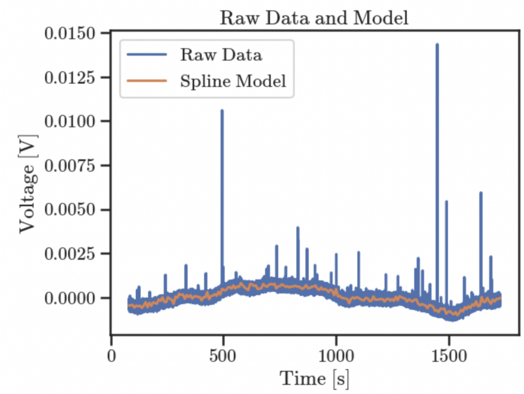

(a) Spline model interpolated from raw data.

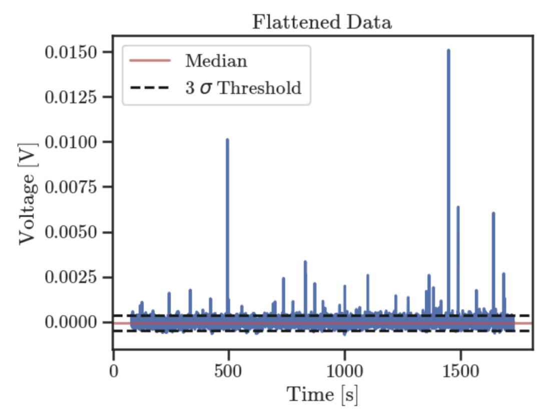

(b) "Flattened" data.

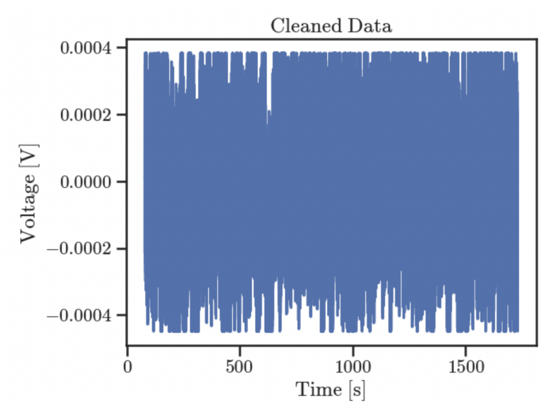

(c) Data after cleaning.

Figure 3.14: Cleaning algorithm applied to ECM data.

Nyquist frequency of the ECM (600 Hz), an appropriate Nyquist factor must be specified for the L-S periodogram to handle higher frequencies.

3.2.4 Significance Calculation

To determine the significance of a peak in the L-S periodogram located at the pulsar's pulse frequency, an ON region is determined by either the width of the pulse frequency error region or the frequency grid spacing, whichever is larger. The choice of the ON region does not have a huge effect on the calculated S/N, as long as it is small enough such that the power spectrum of the chosen frequencies does not exhibit large changes in amplitude. The peak of the ON region is taken to be the signal peak. An OFF region is determined by two regions of width 1 Hz on either side and spaced 0.1 Hz away from the rotation frequency, as to not get any contamination from the true signal but still accurately represent the local noise spectrum.

Significance is calculated by evaluating the likelihood that the ON region peak is coming from a pulsed pulsar signal rather than instrumental or NSB noise. First, it is important to obtain a properly normalized noise spectrum. Following [88], the noise spectrum (OFF region) can be normalized by dividing by the standard deviation of the OFF region divided by two (std[*OFF*]$/2$). Using the method described in Eq. 11 of [89], we assume the normalized noise spectrum to follow an exponential distribution (from a χ^2 distribution with two degrees of freedom). The *scipy* [81] implementation of the χ^2 cumulative distribution function (CDF) with 2 degrees of freedom is used for this work. This distribution returns a p-value (the probability that the given peak is not a noise peak), which can be converted to a significance using the probability point function (PPF; the inverse of the CDF function). The significance can be found using *scipy*'s *scipy.stats.ppf* function. A significance greater than 5σ, excluding trials factors, is generally considered a detection. Trials factors are calculated based on the number of points in the ON region.

3.2.5 Harmonic Stacking

When a discretely sampled time series is Fourier transformed into frequency space, the data become represented by a sum of weighted sine and cosine waves with frequencies at integer multiples of the fundamental frequency (the pulsar rotation frequency). For repeating, periodic signals, harmonic peaks appear in the powers of the Fourier transform at integer multiples of the fundamental frequency. The fundamental frequency itself is considered as the first harmonic. The frequency of each harmonic is given by

$$H_n = nf, \tag{3.7}$$

where H_n is the n^{th} harmonic and f is the fundamental frequency.

Harmonic stacking consists of summing the power spectra of several harmonics. For pulsars, the power of each harmonic decreases by $\approx 1/n$, so generally only a small number of harmonics are stacked to reduce computation time. This technique has proved useful for increasing the signal of dim radio pulsars (e.g., [90]).

For ECM data, the significance of each harmonic for each telescope is calculated independently due to drifts in sampling rate and timing of the ECM that cause small discrepancies between telescopes. The p-values of each harmonic are combined before combining all telescopes. Only the first 3 harmonics are used for ECM analysis because no significant improvement was seen by adding additional harmonics (see Figure 3.15; there is only 0.3% improvement to the S/N between adding H3 and H4).

Harmonic stacking does not always improve the significance of signals in ECM analyses. Pulses from pulsars with sufficiently fast periods ($\lessapprox 0.01$ s) are smeared out by the ECM settling time, which leads to harmonics being too faint to be detected in the Lomb-Scargle periodogram. Pulsars with fast periods are also likely to have their harmonics (if not their signals) well beyond the ECM's Nyquist sampling limit of 600 Hz. Therefore for pulsars with $P < 0.01$s, the harmonic stacking method is not used in order to reduce computational time.

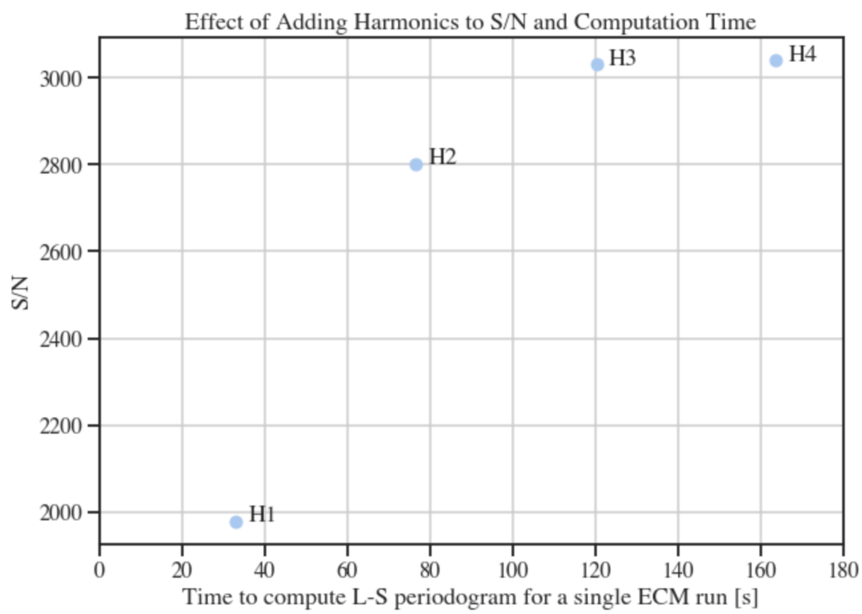

Figure 3.15: Combined S/N for the combination of harmonics up to H_4 as a function of the time needed to obtain the S/N for the full combination. It takes approximately 30s per L-S periodogram per harmonic for a 30 minute ECM run.

3.2.6 Phase Folding

The ECM absolute timing ($\pm$ 1s) is not precise enough to benefit from pulsar timing packages at the current stage. Instead, for the Crab pulsar, the current ephemeris is found for each telescope by selecting the frequency at which the maximum ON region power occurs. For each point in the time array of the time series, a phase value is assigned by

$$phase = t/p - \lfloor t/p \rfloor, \tag{3.8}$$

where t is the time value and p is the pulsar rotation period. The ECM voltage values corresponding to each phase are binned in an appropriate number of bins to represent the data. The mean voltage in each bin is considered to be the signal in that bin.

An optical magnitude for each peak can be extracted from the mean voltage each phase-folded data by Eq. 2.4 to convert the ECM voltage into a magnitude. See Section

5.2.3 for the application of the phase folding method to an analysis of Crab pulsar ECM data.

The VHE and optical analysis techniques discussed in this chapter will be applied to VERITAS data in order to assess the significance of VHE γ-ray and optical emission from pulsar systems (see Chapter 5).

Chapter 4

Optical Pulsar Detectability Studies

4.1 Pulsar Candidate Selection

Though it is difficult to predict which pulsars should have detectable optical pulses with a small sample size of detected sources, it is possible to make general statements about pulsar energetics that should indicate the relative brightness of a source at any wavelength. As discussed in Section 1.1, there are pulsar characteristics that indicate likely detectability across the electromagnetic spectrum, such as close distance and high spin down energy ($\dot{E}$). For this study, a detectability metric D is obtained by

$$D = \frac{\dot{E}}{d^2}, \tag{4.1}$$

where $\dot{E}$ is the rotational energy loss rate and d is the distance obtained from dispersion measure (DM), both obtained from ATNF [5]. Pulsars with shorter periods (faster rotation) and closer distance to Earth are expected to be brightest across the electromagnetic spectrum. This relation is used to isolate the most energetic pulsar populations, which are at the top of the detectability diagram shown in Figure 4.1.

As seen in Figure 4.1, pulsars generally fall into two distinct populations, MSPs and transitional MSPs (tMSPs; MSPs that alternate between states of accretion power and rotation power) in the left population and isolated pulsars in the right population. It is impor-

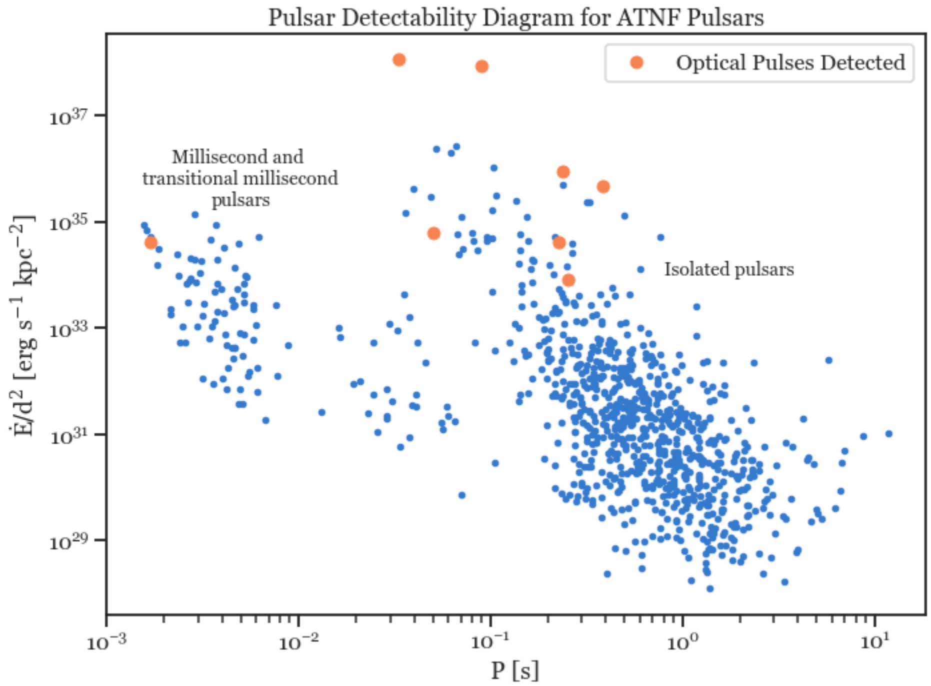

Figure 4.1: Detectability diagram for all ATNF pulsars. Optical pulsars listed in [91] are labelled.

tant to use caution when working with MSPs, since many are in accreting binaries where the thermal accretion-powered emission overpowers any high energy rotation-powered pulses.

As with other sources detected only or primarily in radio wavelengths with unconstrained emission mechanisms (e.g., fast radio bursts), in order to determine expected optical magnitude, it is assumed that optical and radio wavelengths have similar efficiencies. It remains difficult to test whether or not the assumption of similar radio/optical efficiency is reasonable without deeper limits or detections in optical wavelengths, especially given that radio and optical emission do not appear to be produced by the same processes in the same location in the pulsar magnetosphere (see Section 1.2. That being said, The following equation (Eq. 1 from [92]) was applied to the subset of the ATNF catalog at declinations visible to VERITAS ($-14^{\circ} \leq \delta \leq 90^{\circ}$), to obtain an approximate optical ECM magnitude m_{ECM} for each candidate. The ECM magnitude is estimated by

$$m_{ECM} = m_{Crab} - 2.5log[\frac{\dot{P}/P^3}{\dot{P}_{Crab}/P_{Crab}^3}(\frac{d_{Crab}}{d})^2], \tag{4.2}$$

where m_{Crab} is the optical magnitude of the Crab pulsar measured by the ECM (see Section 5.2.3), P and $\dot{P}$ are the pulsar's period and period derivative, respectively, obtained from ATNF [5]. P_{Crab} and $\dot{P}_{Crab}$ are the Crab pulsar's period and period derivative, respectively, obtained from the Jodrell Bank Observatory [73].

Eq. 4.2 is a heuristic that assumes Crab-like optical and radio emission mechanisms and efficiencies for all pulsars. This is unlikely to be the case for MSPs, which are rapidly rotating but have relatively stable $\dot{P}$ values, giving them small magnitude values in equation 4.2. In order to better account for the rotation power of MSPs, we make use of the relation found in [91] that finds a strong correlation between non-thermal X-ray and optical radiation efficiencies $\eta = L/\dot{E}$, where $\dot{E}$ is the pulsar's rotational energy loss and L is the observed non-thermal luminosity.

Fitting the data used in [91], the following linear relation between pulsar optical and X-ray efficiencies is obtained with

$$\eta_{Opt} = \frac{\eta_X - b}{a}, \tag{4.3}$$

where $a = 1.161 \pm 0.001$ and $b = -0.052 \pm 0.001$ with $\chi^2/\text{d.o.f.} = 24/5$. This relation is illustrated in fig. 4.2.

Using non-thermal X-ray fluxes from *Chandra*/ACIS, *XMM-Newton*, *Swift*/XRT, *Suzaku*/XIS compiled in [93], the estimated ECM magnitudes were computed using Eq. 4.3, given that $L = 4\pi d^2 F$, where F is the flux. Substituting fluxes into the optical efficiencies of Eq. 4.3, the following relation between X-ray and optical flux is obtained with

$$F_o = \frac{F_X}{a} - \frac{b\dot{E}}{4\pi d^2 a}, \tag{4.4}$$

and an optical magnitude can be estimated by

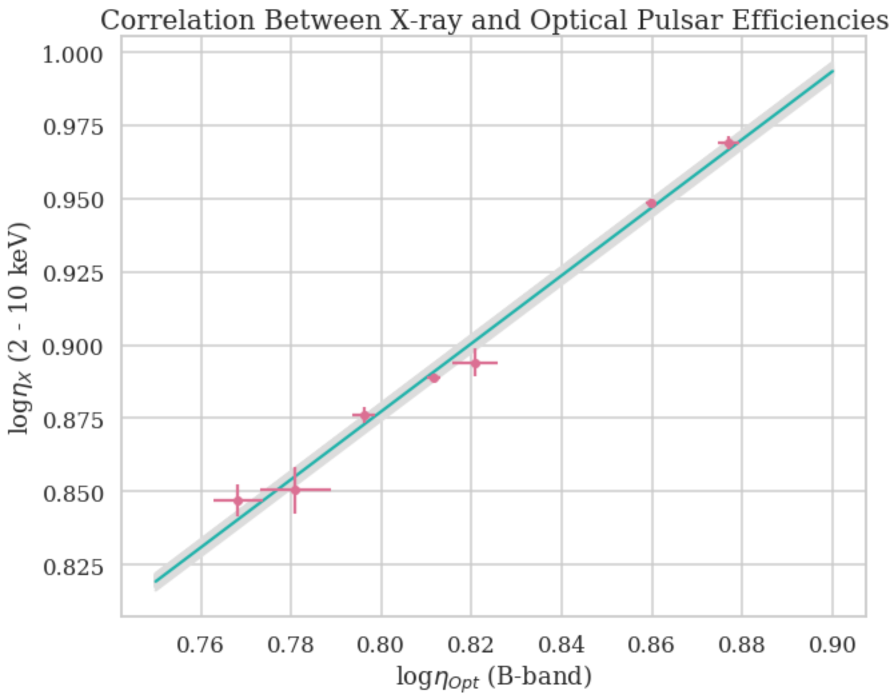

Figure 4.2: Correlation plot for X-ray and optical efficiencies of pulsed, non-thermal emission. Values are obtained from [91].

$$m_o = -2.5\log_{10}\left(\frac{L_o}{L_c}\right) + m_c = -2.5\log_{10}\left(\frac{F_o d_o^2}{F_c d_c^2}\right) + m_c, \tag{4.5}$$

where $m_c = 16.07$ is the Crab magnitude found by the ECM, L_c is the Crab optical luminosity found from Eq. 4.4 using L_x from [94], and $d_c = 2$ kpc [5].

The estimated magnitudes obtained from Eq. 4.2 and Eq. 4.5 are mostly consistent with each other, to within the ECM magnitude resolution of ± 1.

Whether or not either of these relations can accurately predict true optical pulse magnitude is, of course, one of the goals of this study. Therefore, it is advantageous to target observations of the broad category of "Crab-like" pulsars, which includes rapidly rotating (either young or rotation-powered millisecond) pulsars or pulsars that share characteristics such as giant radio pulses (GRPs) and strong light cylinder magnetic fields (B_{LC}) with the Crab pulsar.

Pulsar	Scaling Relation	X-ray Scaling
PSR B1937+21	23.8	22.7
PSR J0218+4232	25.2	24.3
PSR J0205+6449	19.2	20.1
PSR J2229+6114	19.4	20.2
PSR J2021+3651	21.5	21.1
PSR J0633+1746	26.5	21.9
PSR J1023+0038	22.3	24.7

Table 4.1: Comparison of estimated ECM magnitudes from Eq. 4.2 and Eq. 4.5. The uncertainty on each of these values is ± 1, which is driven by the uncertainty on the ECM Crab pulsar magnitude.

In particular, pulsars that exhibit giant radio pulses (GRPs) are thought to be good candidates for optical pulse searches. GRPs are individual radio pulses that are extremely narrow (≈ 2 ns for the Crab [95]) and bright ($> 100\times$ the mean intensity [95]), appearing stochastically in the same phase window as the main pulse and interpulse. The Crab pulsar was originally discovered by observations of its GRPs [96]. In optical searches, [97] found a 3% increase in optical flux temporally coincident with GRPs in the Crab pulsar. Since there are no other changes to the pulse profiles or timing, it is believed that an increase in e^+/e^- density is responsible for increasing both coherent radio emission and incoherent synchrotron optical emission. Of the sources that are known to have GRPs, 3 are MSPs (PSR B1937+21 [98], PSR B1821-24 [99], and PSR J0218+4232 [100]), and 2 are young pulsars (Crab pulsar and PSR B0540-69 [101]) Though these two populations are generally very different, all five sources share some commonalities: hard, non-thermal HE emission, high B_{LC}, and fast periods.

Most of these sources are expected to pulse at VHE γ-ray energies, but at fluxes significantly below the sensitivity of VERITAS, even after hundreds of hours of observations. Figure 4.3 shows the spectra of all 4FGL [26] *Fermi*-LAT pulsars extrapolated to the low energy end of VERITAS' sensitivity. Only pulsars whose spectrum is dominated by pulsed emission (i.e., the PWN or SNR is not bright compared to the pulsar) are selected for extrapolation.

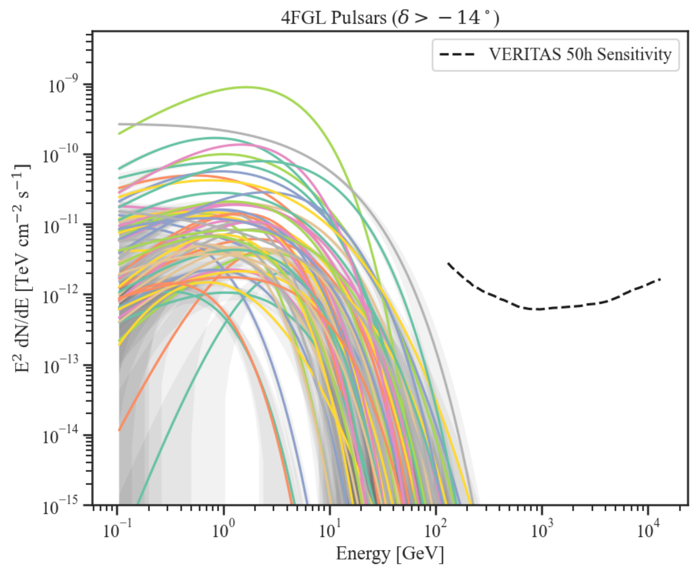

Figure 4.3: *Fermi*-LAT detected pulsars with pulsed spectra extrapolated to energies detectable to VERITAS.

Due to the expected faint VHE fluxes, pulsars for this study are selected only based on expected optical magnitude. Simultaneous γ-ray pulsar observations are useful only in the case of the Crab pulsar, but may be used to study the PWN or TeV halo surrounding the pulsar.

All ATNF catalog pulsars visible to VERITAS are ranked according to the estimated ECM magnitude found in Eq. 4.2, with several top candidates chosen for deeper studies. The candidates selected are shown in Table 4.2 and consist of ATNF pulsars with estimated ECM magnitude < 22 as well as two MSPs (PSR B1937+21 and PSR J0218+4232) that have high B_{LC} values and exhibit GRPs. Transitional MSP PSR J1023+0038 is also included because it has been detected to pulse optically during accretion states [15]. The following criteria are used to determine which sources should be examined further to determine ECM detectability:

- $P < 0.1$ seconds
- Declination visible to VERITAS ($> -14^\circ$)

Pulsar Name	Right Ascension	Declination	Age (log(years))	Distance (kpc)	Period [s]	$\dot{P}$ [s/s]	$\dot{E}$ [erg/s]	B_{LC} [G]
B0531+21 (Crab)	05 34 31.97	+22 00 52.1	3.1	2	0.033	4.21e-13	4.5e+38	9.55e+05
J0205+6449	02 05 37.92	+64 49 41.3	3.7	3.2	0.066	1.94e-13	2.7e+37	1.19e+05
J2229+6114	22 29 05.28	+61 14 09.3	4.0	3	0.052	7.82e-14	2.2e+37	3.21e+05
J2021+3651	20 21 05.46	+36 51 04.8	4.2	1.8	0.10	9.57e-14	3.4e+36	7.65e+02
J0633+1746 (Geminga)	06 33 54.15	+17 46 12.9	5.5	0.25	0.24	1.10e-14	3.2e+34	1.42e+05
B1937+21	19 39 38.56	+21 34 59.1	8.4	3.5	0.0016	1.05e-19	1.1e+36	2.68e+04
J0218+4232	02 18 06.36	+42 32 17.4	8.7	3.2	0.0023	7.73e-20	2.4e+35	1.39e+05
J1023+0038	10 23 47.69	+00 38 40.8	9.3	1.4	0.0017	4.0e-16	9.8e+34	2.13e+05

Table 4.2: List of pulsar candidates for ECM observations.

- Non-thermal X-ray pulses detected (sharp, non-sinusoidal peaks imply magnetospheric emission; see Section 1.2.1).

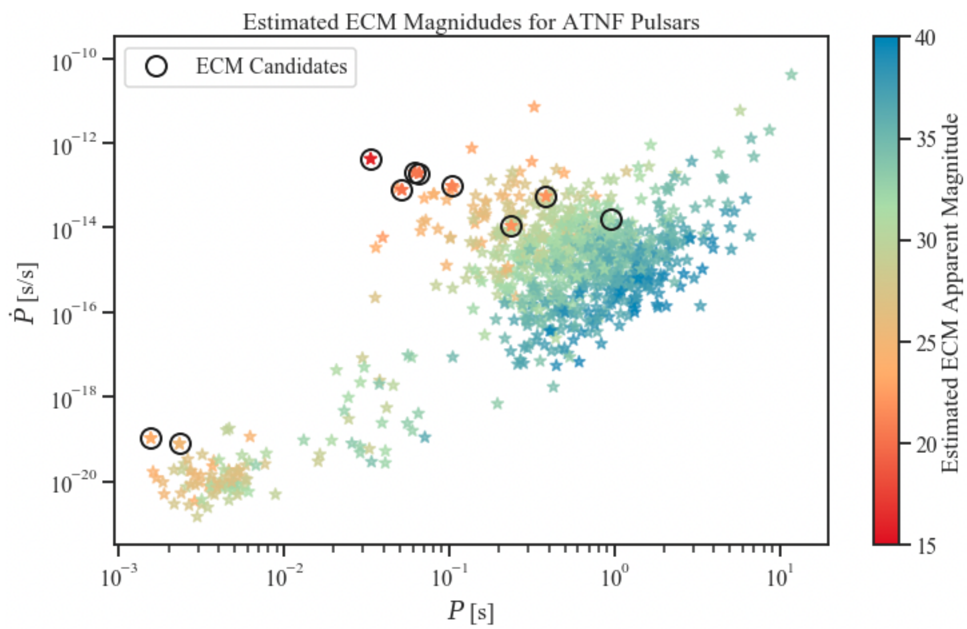

Figure 4.4: $P - \dot{P}$ diagram of all ATNF pulsars at declination $\delta > -14°$ with estimated ECM magnitudes calculated from Eq. 4.2. Black circles denote the pulsars selected for further ECM studies in Table 4.2.

In the following sections, the pulsars selected in Table 4.2 that have been selected as candidates for ECM observations are described.

PSR B1937+21

PSR B1937+21 is a MSP (P = 1.55 ms) with no identified binary companion. This was the first pulsar selected for VERITAS observations as part of this study. PSR B1937+21 is the fastest Northern hemisphere MSP and exhibits both GRPs, relatively high X-ray flux $F_X = 3.95 \times 10^{-13}$ erg s^{-1} (c.f. median $F_X = 9.84 \times 10^{14}$erg s^{-1} for sources in [93]) and a strong $B_{LC} = 1.02 \times 10^6$ G (c.f. median ATNF $B_{LC} = 61$ G). More information about the source can be found in Section 5.3.

It is worth noting that the one of the reasons for which PSR B1937+21 was selected as the only optical pulsar candidate to be followed up with VERITAS observations so far is due to an outdated distance in the ATNF catalog version used for this study (version 1.54[1]). More recent catalog versions discuss the distance of PSR B1937+21 from 1.5 kpc to 3.5 kpc, and PSR B1937+21 is believed to be no longer as clearly detectable as previously thought, but may still be visible to VERITAS, as will be discussed in Section 4.2.1.

PSR J0218+4232

PSR J0218+4232 is a MSP (P = 2.32 ms) in a white dwarf binary system (so the system is non-accreting) with a hard, non-thermal X-ray spectrum [102]. Like PSR B1937+21, PSR J0218+4232 also exhibits GRPs, a strong $B_{LC} = 3.21 \times 10^5$G, and high X-ray flux $F_X = 4.62 \times 10^{-13}$.

PSR J0218+4232 is also tentatively associated with a TeV source 1LHAASO J0216+4237u [60] that is only seen at energies > 25 TeV. If PSR J0218+4232 and 1LHAASO J0216+4237u are truly associated, a detection of VHE emission from the system would be the first detection of a TeV halo around a MSP.

PSR J0205+6449

PSR J0205+6449 is a young ($\approx$ 5000 years old [5]) 65 ms, rotation-powered pulsar associated with SNR 3C 58. It has the third highest $\dot{E}/d^2$ (spin down energy flux) value of all ATNF pulsars, after only the Crab pulsar and Vela. Chandra observations [103] show a narrow X-ray pulse and non-thermal spectrum.

[1]https://www.atnf.csiro.au/people/pulsar/psrcat/catalogueHistory.html

A search for an optical counterpart for PSR J0205+6449 was conducted in [104] that detected an un-pulsed point source. However, none of the instruments used there have sufficient time resolution to detect optical pulses.

PSR J2229+6114

PSR J2229+6114 is a 52 ms pulsar with high $\dot{E} = 2.2 \times 10^{37}$ and sharp, non-thermal X-ray pulses [105]. PSR J2229+6114 is located within the Boomerang PWN (PWN G106.65+2.96), which is potentially associated with LHAASO J2226+6057, a PeVatron candidate whose spectrum extends beyond 100 TeV [106].

PSR J2021+3651

PSR J2021+3651 is a 0.1 s pulsar located within the Dragonfly nebula and potentially associated with extended VHE source VER J2019+368. PSR J2021+3651 is Vela-like (i.e., similar to the Vela pulsar) in age (10 kyr) and energetics ($\dot{E} = 3.4 \times 10^{36}$). Though Vela-like pulsars are not expected to be efficient at optical, X-ray, or γ-ray energies, PSR J2021+3651 is fairly close (1.8 kpc) and shows evidence of weak non-thermal X-ray pulses [107], which satisfies the above criteria for sources that may be ECM detectable.

PSR J0633+1746

PSR J0633+1746, more commonly known as Geminga, is a radio-quiet (HE γ-ray bright), middle-aged pulsar known to have a TeV halo [50], which is very extended ($> 2^{\circ}$), mostly due to its proximity of 250 pc. Geminga has a pulse period of 0.2 s, which is slightly slower than the criterion that this study allows, but its detection is still perhaps possible by cleaning the data (see Section 3.2.2 and selecting noise regions in areas of frequency space that are not heavily contaminated by low-frequency noise peaks.

Geminga was an exception to the above criteria because possible pulsed optical emission has been seen at a significance of $\approx 4\sigma$ in [108]. Since Geminga's X-ray pulse profile seems to be predominantly thermal [109], it would be interesting to obtain a detection and spectral point in an optical wavelength to determine whether the optical emission is also thermal in nature, or non-thermal as we would expect (see Section 1.2).

Follow-up observations of Geminga with the ECM (which has $\approx 1000\times$ better time resolution and double the light collecting area/telescope than the instrument and telescope used in the previous study) would be particularly interesting to either validate or refute the detection of Geminga as an optical pulsar.

PSR J1023+0038

Unlike the other MSP candidates (PSR B1937+21 and PSR J0218+4232), PSR J1023+0038 is in an accreting binary system with a 0.2 $M_\odot$ stellar companion. PSR J1023+0038 is known as a transitional millisecond pulsar (tMSP) and alternates between stages of accretion power and rotation power.

Though it is generally thought that the brightness of the thermal accretion disk emission should make it difficult to see pulsed emission, the accretion state seems to increase the efficiency of non-thermal optical processes. A detection of optical pulses from PSR J1023+0038 [110] during an X-ray/HE γ-ray high state suggests that the pulsed flux originates from inverse Compton scattering within the optically thick accretion disk. In [110], an optical luminosity of $L = 4.2 \times 10^{33}$ erg s^{-1} (where the pulsed component represents 97% of the total emission) and a g-band magnitude of $g \approx 22.5$, corresponding to an estimated ECM magnitude of 24 were determined. This is dimmer than expected to be detectable from ten hours of ECM observations (see Figure 4.7), but since optically detected tMSPs are a new source class that could potentially motivate other binary observations, it may be possible to take longer observations of PSR J1023+0038.

4.2 ECM Simulations

To determine pulsar visibility to the ECM, we generate simulated ECM data containing the pulsed signal. The signal's amplitude is calculated by Eq. 2.4 with an apparent magnitude found from 4.2 or 4.3 for MSPs with known X-ray luminosity, L_X. The pulse period is taken from ATNF and the pulse width corresponds to the X-ray pulse full width half maximum (FWHM) value or from ATNF if there is no available X-ray pulse profile. Following the assumption that X-ray and optical emission originate from the same location, the X-ray pulse should be more similar to the optical pulse than the radio pulse. Of course, there is only a limited sample of optical pulsars, so the assumption of a linear X-ray/optical flux relation remains to be tested.

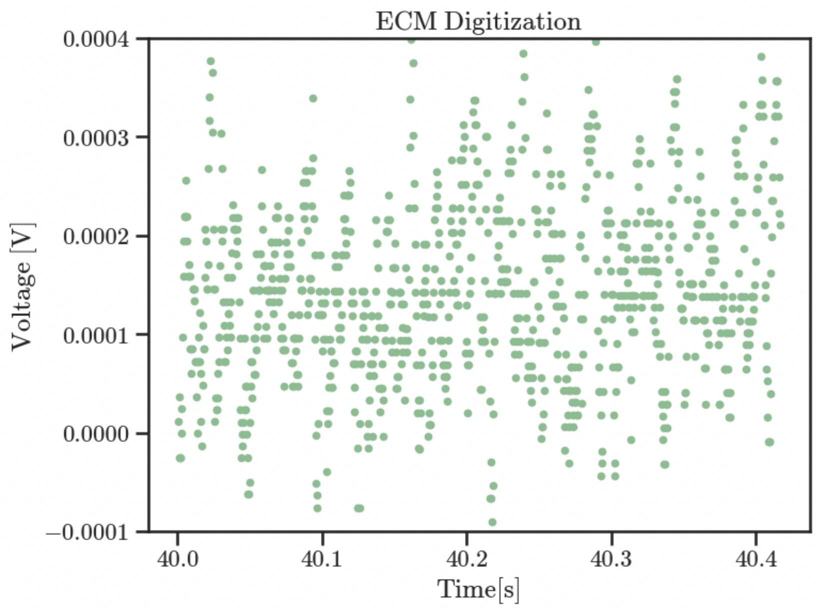

Figure 4.5: A small sample of a single telescope ECM run, chosen to show the G100 digitization, which appears as horizontal lines formed by data points clustering around the digitization values..

Simulations are conducted as follows:

1. Background data files for each telescope are obtained from ECM observations where no source has been detected. Approximately ten hours of background data were used for these studies, divided into individual runs of 20-60 minutes.

2. The background data are cleaned according to the algorithm described in Section 3.2.2.

3. The digitization (see Figure 4.5) of the data is removed by adding Gaussian noise to the background voltage at the width of the G100 digitization (1.22×10^{-5} V).

4. A Lorentzian pulse is generated with

$$S = \frac{V_{ECM}}{(1 + ((t - \mu)/(0.5 \times FWHM))^2}, \tag{4.6}$$

where V_{ECM} is the estimated ECM voltage, μ is phase at which the peak occurs, and $FWHM$ is the non-thermal X-ray FWHM. The pulse is convolved with the ECM settling time (an exponential with a decay constant of 2.89 ms) in order to match the Crab pulse shape seen by the ECM (see Section 5.2.3).

5. A pulse train of these smeared Lorentzian pulses is injected into the un-digitized background data from step 2 at intervals corresponding to the ECM sampling rate (1200 Hz for this work).

6. The full signal is re-digitized into bins of 1.22×10^{-5} V.

7. The data from step 5 are then processed through OOPS-E as described in Section 3.2.

8. The background runs without injected signal are processed through OOPS-E in order to determine if the significance of the simulated signal found in step 7 is due to the injected pulses and not from noise peaks.

9. The significances for all four telescopes in each run are combined.

10. All run significances are combined.

Figure 4.6 describes how the above steps fit into the OOPS-E analysis pipeline described in Section 3.2.

In order to determine the magnitude cutoff for the sample in Table 4.2, a test was performed by injecting a Crab-like pulse (same period and width as the true optical Crab

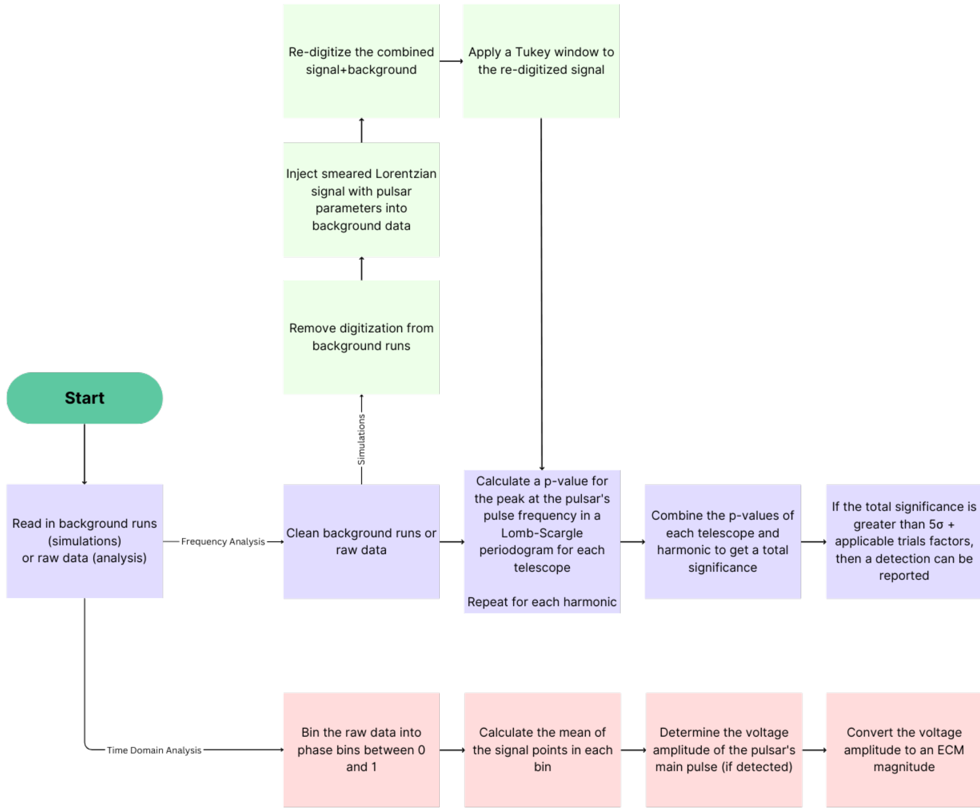

Figure 4.6: Flowchart describing the above simulations (green boxes) and how they fit in with OOPS-E data analysis (purple boxes; see Section 3.2) and phase-folding (pink boxes; see Section 3.2.6).

pulse) from $m_B = 16$ to $m_B = 30$ into ≈ 10 hours of background data using the same simulation steps as outlined above. Pulses at periods of 3 ms, 30 ms (the Crab pulsar frequency), and 300 ms were tested. The results of the Crab-like pulse injection test are shown in Figure 4.7, where it is clear that signals with faster periods can be detected to larger (dimmer) magnitudes.

4.2.1 Results

All of the candidate pulsars listed in Table 4.2 were simulated using the magnitude estimates from Eq. 4.2 and Eq. 4.5 to estimate the ECM voltage amplitude. The results of this study are presented in Table 4.3. For each source, a periodic signal with the pulsar

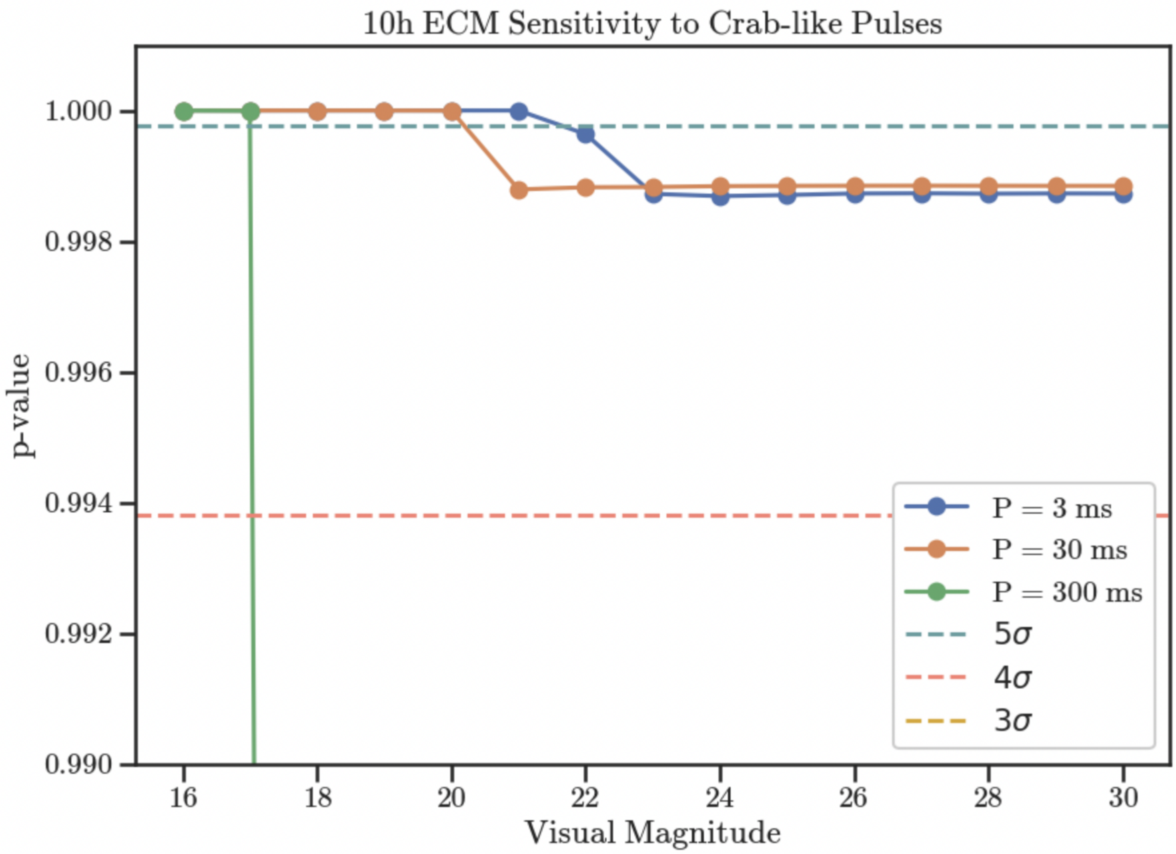

Figure 4.7: Crab-like pulse sensitivity test results. The plot has been cropped to show the magnitudes at which signals drop below 5σ. The flattening of the signals below 5σ is not well understood, but is further discussed in Section 4.2.1.

parameters was injected into 10 hours of background runs as per the steps outlined in Section 4.2. This is done for magnitudes obtained by both the Crab pulsar scaling relation (Eq. 4.2) and the X-ray scaling relation (Eq. 4.5).

The threshold significance required for a detection in this study is 5σ because the ON region in which the peak is chosen can be chosen such that it is the width of the frequency bin in which the pulsar's pulse frequency is obtained. This leads to only one data point in the search region, which does not require consideration of the look-elsewhere effect. However, the look-elsewhere effect will not necessarily apply to the ECM data, because the pulse frequency is not typically known precisely enough for the error region to be smaller than or equal to the frequency bin width.

Pulsar	Crab Scaling Significance	X-ray Scaling Significance	Background Significance	Threshold Significance
PSR B1937+21	1.1	1.6	1.1	5
PSR J0218+4232	1.2	1.1	1.4	5
PSR J0205+6449	2.4	3.8	2.3	5
PSR J2229+6114	2.7	6.4	1.7	5
PSR J2021+3651	2.7	2.5	2.5	5
PSR J0633+1746	1.5	1.5	1.5	5
PSR J1023+0038	1.4	1.3	1.1	5

Table 4.3: Simulated results of pulsar observations with the ECM.

For this study, the only pulsar for which a statistically significant detection may be reached after ten hours of observations is PSR J2229+6114 using the X-ray scaling relation magnitude (Eq. 4.5). The cumulative p-value of PSR J2229+6114 is shown in Figure 4.8, where the final p-value after 9.77 hours of simulated data corresponds to 6.4 σ.

In order to estimate if any of these sources may be detectable by the ECM with more observing time, a linear function is fit to the cumulative p-value plots and extrapolated to larger exposure times. These plots can be found in Appendix A and their results are presented in Table 4.4.

This study reveals that there are many sources for which the background data grows equally or more quickly in significance than the data comprised of both signal and background (e.g., Figure 4.9; more plots can be found in Appendix A). It remains unclear as to why the background should show a more significant peak at the pulse frequency. One possible hypothesis is that the injected pulses cause a smearing of noise peaks across several bins near the pulse frequency, leading to a decrease from the original, sharper noise peak.

Additionally, it can be seen in the simulations of every source that the significance of the background data always increases with time. This is because the significance calculation method used in this analysis (see Section 4.2) always selects a positive peak for which to evaluate the significance, because the Lomb-Scargle periodogram does not contain negative peaks. The combination of positive significances, however small they may

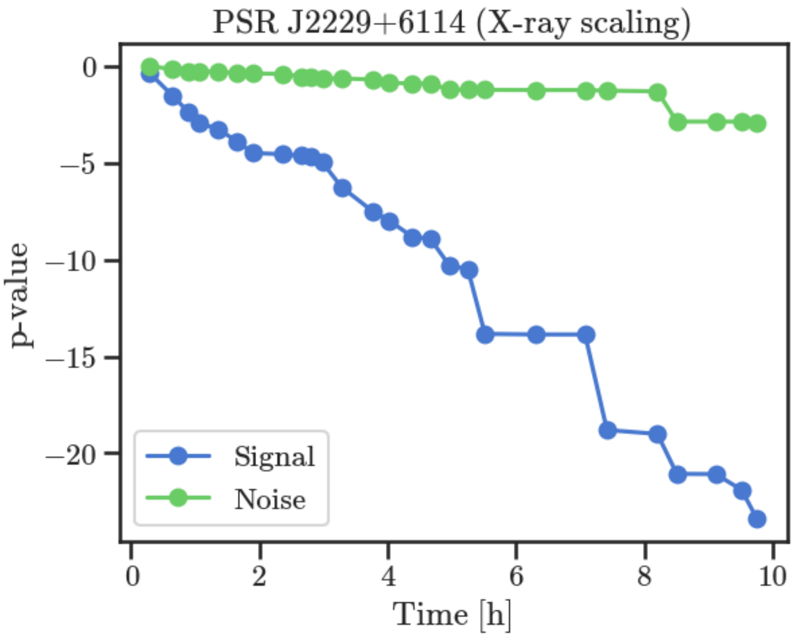

Figure 4.8: Cumulative p-value vs. time for simulated data of PSR J2229+6114 using an estimated ECM magnitude calculated by Eq. 4.5. 'Signal' corresponds to the simulated data comprised of background runs with an injected pulsar signal and 'Noise' corresponds to the background data only. Note that smaller p-values correspond to higher significances. The flattening of signals in a given run (e.g., $5-7$ hours) is thought to be due to the NSB peaks dominating the signal peaks, such that no additional significance is added to the cumulative significance.

be, will always lead to an increasing cumulative significance. This means that given a long enough observation, the background data will cross the detection threshold. While an artificial signal originating from background noise isn't a problem for the simulated data, because the background data is available for comparison, high background signal must be considered for observations. The high significance of background peaks compared to signal makes it unclear as to how to determine if frequency space peaks are truly originating from the pulsar. This issue makes it difficult to reliably estimate the true significance of a pulsar and use simulations to estimate how much exposure time is needed for a detection.

Pulsar Name	20h Significance [σ]	20h Background Significance [σ]	50h Significance [σ]	50h Background Significance [σ]
Crab Scaling				
PSR B1937+21	2.2	2.2	4.0	4.0
PSR J0218+4232	2.4	2.7	4.3	4.8
PSR J0205+6449	3.3	3.0	5.6	5.3
PSR J2229+6114	4.0	2.7	6.9	4.8
PSR J2021+3651	3.6	3.9	6.1	6.6
PSR J0633+1746	2.1	2.2	3.9	4.1
PSR J1023+0038	2.8	2.7	5.0	4.9
X-ray Scaling				
PSR B1937+21	2.9	2.1	4.8	4.0
PSR J0218+4232	2.3	2.6	4.1	4.6
PSR J0205+6449	5.2	3.0	> 8	5.3
PSR J2229+6114	> 8	2.7	> 8	4.8
PSR J2021+3651	3.6	3.9	6.1	6.6
PSR J0633+1746	2.0	2.2	3.9	4.1
PSR J1023+0038	2.5	2.4	4.5	4.4

Table 4.4: Extrapolated significances to 20 hours and 50 hours for all simulated pulsars based off of linear fits to each pulsar's signal and noise cumulative p-values.

Both of the abovementioned issues with significance calculations remain without a solution. Future tests and analysis methods will need to be developed in order to determine the cause and any possible solutions to these problems.

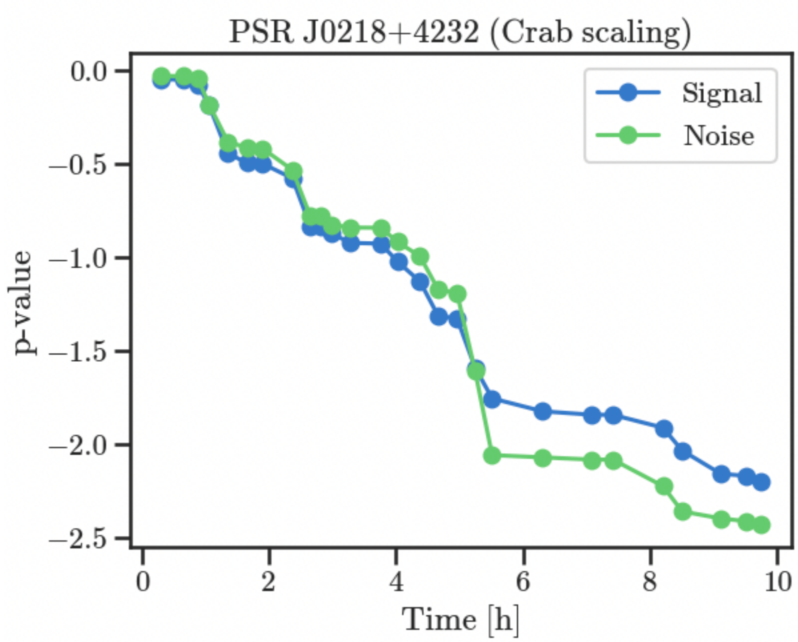

Figure 4.9: Cumulative p-value vs. time for simulated data of PSR J0218+4232 using an estimated ECM magnitude calculated using Eq. 4.2.

Chapter 5

Pulsar Observations and Analysis

5.1 Analysis Overview

The sources analyzed in this work are the Crab system and PSR B1937+21, where the Crab system is comprised of PSR B0531+21 (Crab pulsar) and the Crab nebula (M1). Figure 5.1 shows the analyses conducted for each source.

Though it was discussed in Section 4.2.1 that PSR J2229+6114 is a favourable candidate over PSR B1937+21, the initial calculations performed for this work estimated that PSR B1937+21 was instead the favourable candidate. Previous calculations used an outdated pulsar distance for PSR B1937+21 from ATNF as well as an ECM sampling rate of 4800 Hz, since the settling time issue (see Section 2.3) had not yet been identified when time was requested on PSR B1937+21 during the 2021-2022 season.

VHE γ-ray data is analyzed with Eventdisplay, as described in Section 3.1. The analysis of pulsed VHE emission requires some additional work after the Eventdisplay analysis is done, as described in Section 3.1.8. Optical emission is analyzed with OOPS-E, as described in Section 3.2, with phase folding steps described in Section 3.2.6.

It is currently unknown as to whether or not PSR B1937+21 has a PWN or TeV halo counterpart in VHE. Further investigation must be undertaken before performing VHE analysis of the source region, so VHE analysis of the PWN is beyond the scope of this work and may be presented in future work. The complicated nature of a potential PWN/TeV halo will be further discussed in Sections 5.3 and 5.3.2.

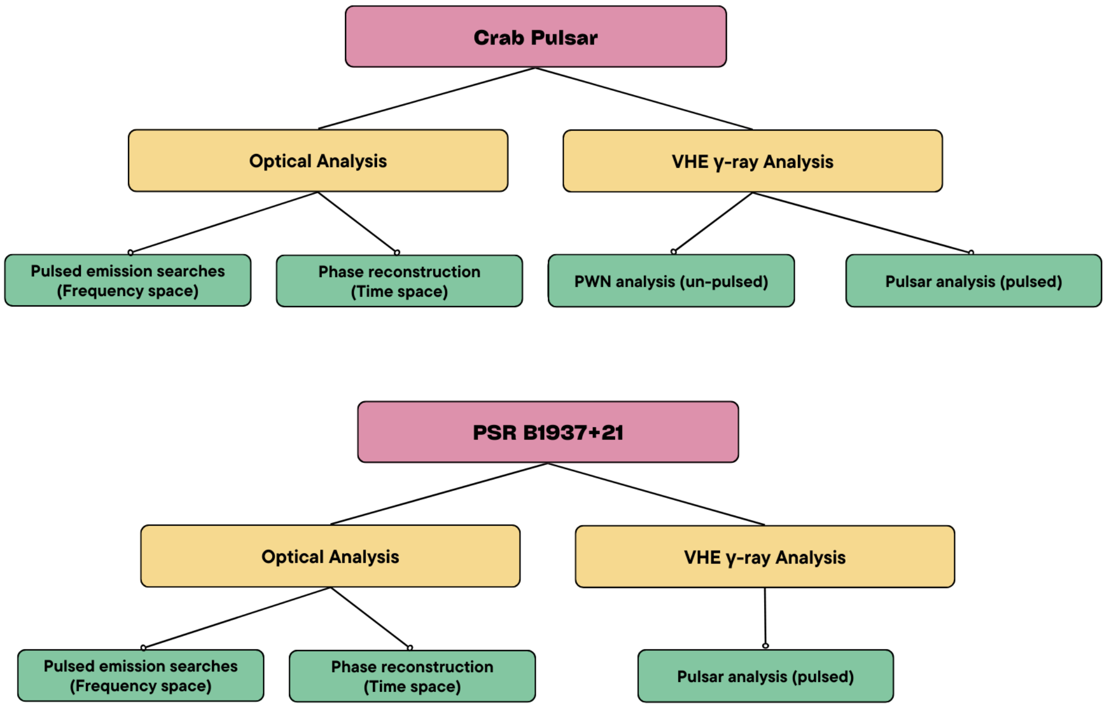

Figure 5.1: Flowchart describing the analyses performed for this work.

5.2 The Crab Pulsar

PSR B0531+21, known colloquially as the Crab pulsar, is a particularly unique source along with the associated pulsar wind nebula, the Crab nebula. While the Crab pulsar and nebula are not particularly unusual astrophysically, their young age and proximity to Earth make them particularly bright sources.

The Crab PWN (hereafter referred to as the Crab nebula) was the first detected VHE γ-ray source, detected by the Whipple 10-m IACT [39]. The current generation of IACTs detect the Crab nebula in a few minutes, making it an excellent source for calibrating the instrument response as well as testing new analysis techniques.

The Crab pulsar is the brightest known pulsar across the electromagnetic spectrum. Formed from the collapse of a massive star, the Crab nebula and supernova were first observed and documented by civilizations around the world in 1054 C.E. Though the Crab pulsar is old on human timescales, the Crab pulsar remains the fourth youngest observed pulsar and the youngest pulsar in the Northern sky [5].

5.2.1 Observations

The VERITAS instrument detects both the Crab nebula and its pulsar as a single point-like source in γ-rays, and has taken data on both components since the beginning of full-array operations in 2007. However, use of the ECM to take joint optical and γ-ray observations of the Crab pulsar has only been part of the observation program in recent years. Most of the data presented in this work is from the 2022-2023 season, with one run from 2018 that allowed us to first determine that optical pulses from Crab pulsar could be detected with the ECM.

In total, the data set used in this work is comprised of eight 30-minute runs in both optical and γ-ray wavelengths. A broader set of 66 hours of γ-ray data on the Crab pulsar collected during the 2019-2023 season were used to obtain an updated Crab pulsar detection since the last VERITAS result in 2015 [111]. Table 5.1 describes the total number of observation hours and total exposure time after data quality cuts.

Quality cuts are applied to the data to exclude any sections of the runs affected by weather, instrument readout issues, bright transients, or other non-astrophysical events.

5.2.2 VHE γ-ray Analysis

Separate γ-ray analyses were conducted to detect the PWN emission and the pulsar emission separately. Since the Crab pulsar is much dimmer and has a softer spectrum than the nebula, a longer dataset must be used to detect pulsed emission.

Dataset	Dates	Epoch	Total Exposure (h)	Total Usable Exposure (h)
Crab Nebula	17/01/2018 - 19/03/2023	V6	5.25	5.02
Crab Pulsar	06/01/2018 - 19/03/2023	V6	68.55	66.87

Table 5.1: Run dates and exposure times for the γ-ray nebula and pulsar analyses.

For the nebula detection, only runs taken jointly with ECM data are used. Since observations taken with either clouds or bright moonlight (> 33% of the moon illuminated) increase NSB levels and attenuate dim Cherenkov light pools (which generally originate from low energy showers; see discussion in Section 2.2.4), for the Crab pulsar, all data from 2018 - 2023 taken during ideal conditions (no moonlight, A weather, $> 50°$ elevation) were used. "A weather" corresponds to conditions in which skies are completely clear and no clouds are visible to observers. The full exposure times for both of these analyses, along with the exposure times corrected for data quality cuts, are found in Table 5.1.

VHE Non-pulsed Emission

γ-ray analysis for the Crab nebula can be performed using the standard Eventdisplay analysis described in section 3.1. Moderate cuts (see Table 3.2) are used in the nebula analysis, since these are optimized for the Crab nebula spectrum ($\Gamma = 2.4$).

The Crab nebula is detected in this analysis with a significance of 89σ (see Figures 5.2 and 5.3). The Crab nebula reaches the detection threshold of 5σ after only 1.6 minutes of observations. The growth of the significance with exposure time follows a square root function, as expected from Poissonian statistics in the low counts regime (see Figure 5.2).

Pulsed Emission

A source with flux 1% of the Crab's flux (such as the Crab pulsar) should be detected in 21.5 hours as per VERITAS' sensitivity calculations. However, the Crab pulsar is not just dimmer in flux, but also has a much softer spectrum ($\Gamma = 3.8$). Figure 5.4 shows that the VHE end of the spectrum cuts off to fluxes below VERITAS' sensitivity around the range of $\approx$ a few hundred GeV. This means that much larger (> 50 h) datasets are necessary to

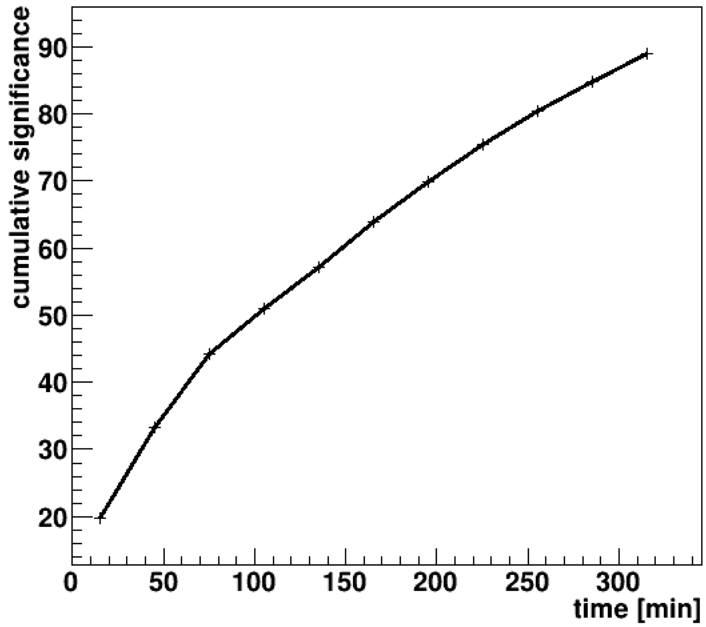

Figure 5.2: Cumulative significance of the Crab nebula for the nebula dataset described in Table 5.1.

detect pulsed VHE γ-ray emission from the Crab pulsar, as can be seen from the exposure times in Table 5.1.

In previous analyses (e.g., [6, 112], cut values were optimized in order to exclude photons originating from the Crab nebula. This is a computationally heavy process that involves iterating through analyses of Monte Carlo simulated data until the data remaining after cuts has a Crab pulsar-like spectrum. Producing these simulations was beyond the scope of this work, so Eventdisplay's default "supersoft" cuts were used, as described in 3.2. Supersoft cuts are designed to lower the energy threshold as much as possible, which should prevent low energy events originating from the pulsar from being cut (see Table 3.2).

Since only a phase-folded significance is obtained for this work, it is not necessary to remove counts from nebula emission. However, the nebula emission is un-pulsed and thus will only appear in the phase-folded counts as a constant added to both the ON and OFF phase gate regions, which should not largely affect significance calculations.

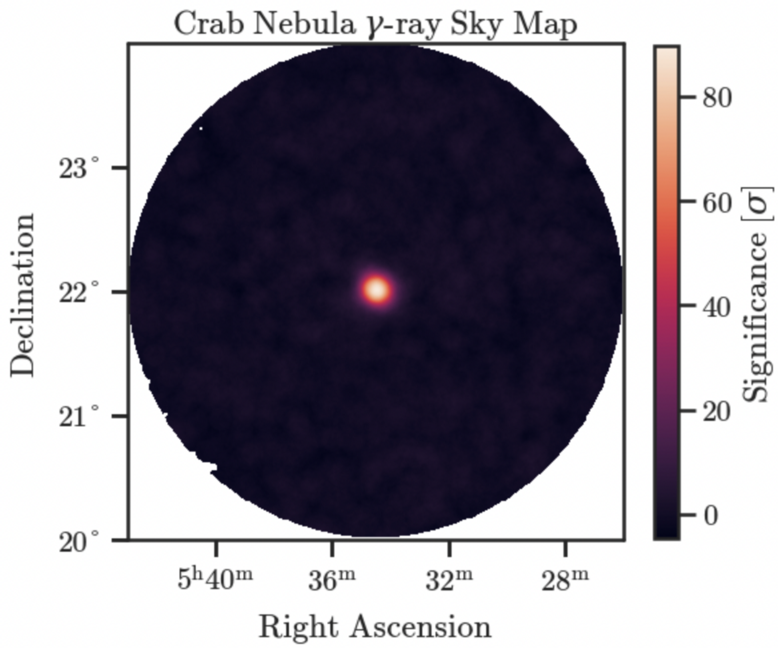

Figure 5.3: Significance of γ-ray excess plotted as a function of angular position Significance of γ-ray excess plotted as a function of angular position. White spots in the sky map are due to a lack of events at that location.

Main pulse	Interpulse	Background
$-0.01 < phase < 0.01$	$-0.38 < phase < 0.41$	$-0.43 < phase < 0.94$

Table 5.2: Phase gate values for pulsed emission significance calculation.

The phaseogram obtained in this analysis is shown in 5.5. A phaseogram shows either the counts (for VHE emission) or flux (for optical emission) phase-folded between phases of 0 and 1, to show the integrated pulse profile. As per pulsar convention, identical phase-folded data is shown twice (between phases 0 and 1 and between phases 1 and 2) to guide the reader's eye to the peaks. The energy threshold of 126 GeV is calculated as the edge of the lowest energy bin from the Eventdisplay analysis with a detection significance $> 2\sigma$. The period on which the counts are folded is obtained from [73].

Using the phase gates used for the analysis in [6] (see Table 5.2 and Figure 5.6), evidence for the main pulse at a significance of 4.3σ and a detection of the interpulse at a significance of 7.6σ were found.

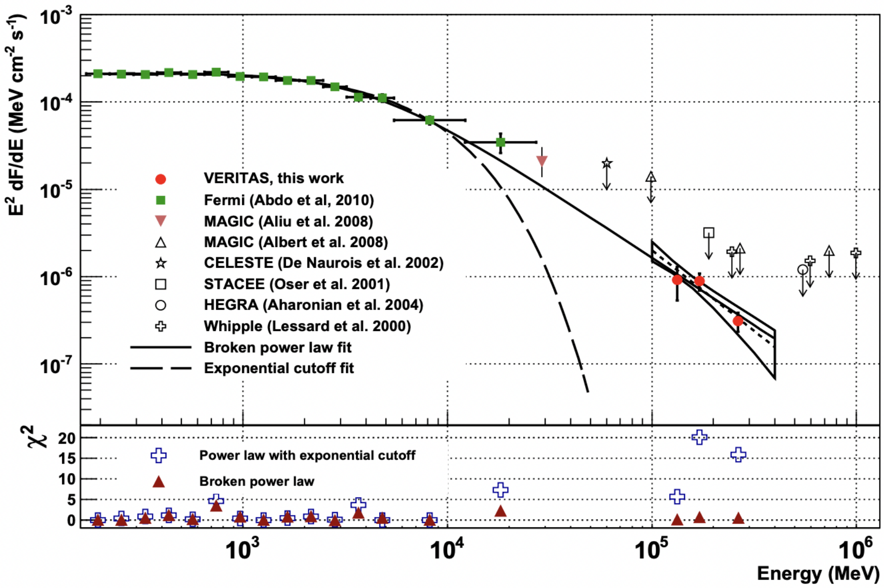

Figure 5.4: Crab pulsar spectrum at γ-ray energies. From [6].

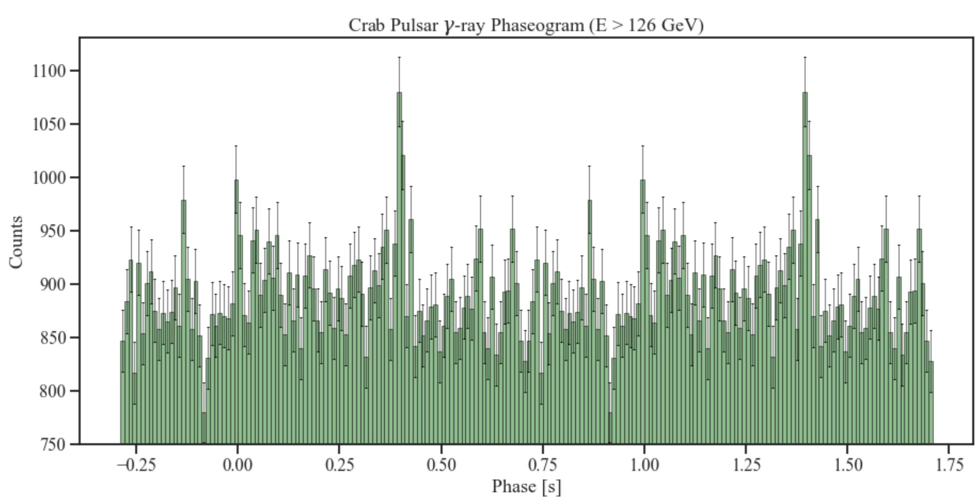

Figure 5.5: VHE γ-ray phaseogram of the Crab pulsar. The same phase is shown twice to guide the eye.

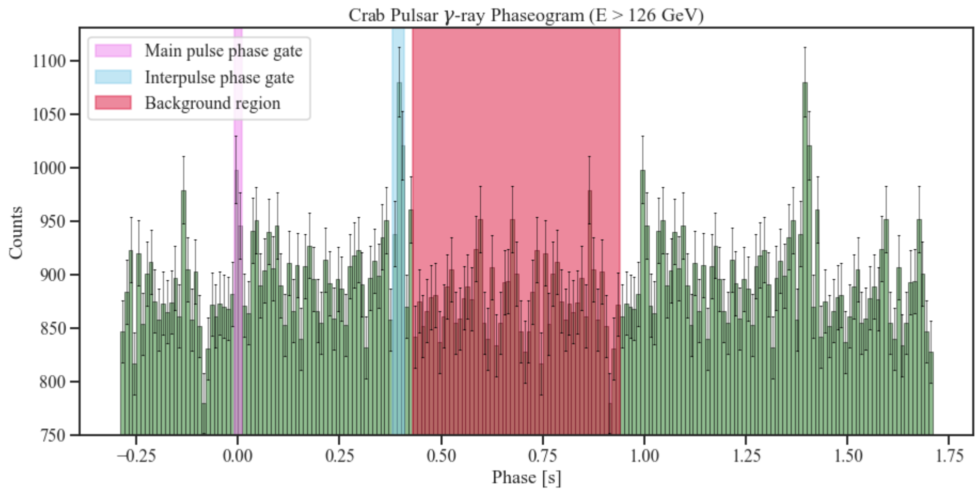

Figure 5.6: Phase gates and background region for pulsed emission significance calculation.

5.2.3 Optical Analysis

Significance Calculation

All nine ECM Crab runs are processed using the method outlined in Section 3.2. Data quality cuts are applied to the beginning and end of data taking, to remove effects from telescope slewing and pixel suppressions that denote the beginning and end of each data-taking run (see Figure 5.7).

The ON region for the Crab pulsar is selected as the difference between the latest known Jodrell Bank rotation period [73] and the extrapolation of that period to the observation date. The ON region is determined by

$$ON = \pm|\dot{P}_{JB} * \Delta t|, \tag{5.1}$$

where $\dot{P}$ is the period derivative and Δt is the elapsed time between the latest Jodrell Bank ephemeris and the observation date. For the data presented in this work, $ON \approx 0.01$ Hz. The extrapolation in Eq. 5.1 is just an approximation, as this extrapolation does not take into account the second period derivative or any drift in the ECM clocks (which is known

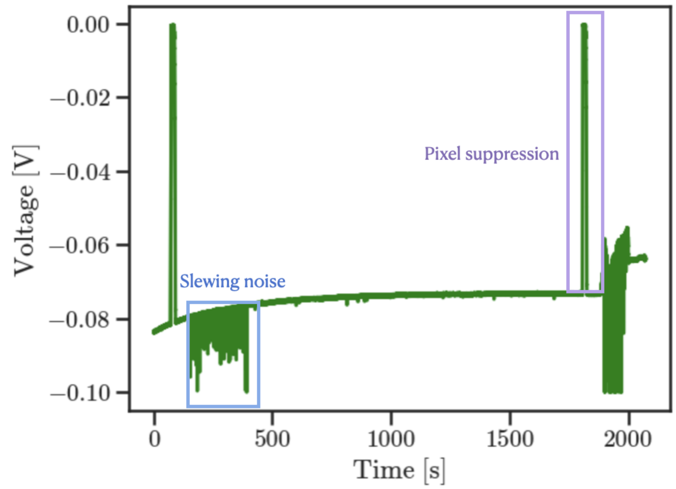

Figure 5.7: ECM signal contamination due to slewing noise and pixel suppressions. These are removed before analysis as part of data quality checks.

to shift peaks slightly). However, it can be seen in Figure 5.8 that Eq. 5.1 errs on the larger side, so the region should still contain the signal.

For each telescope dataset from each run, the peak of the Crab pulsar signal found by the Lomb-Scargle periodogram is so large, the p-values obtained for each telescope will be equal to exactly 1 due to machine precision limitations (i.e., the true p-value is less than $1-10^{-16}$ or $> 8\sigma$) , from which a significance cannot be calculated. It is possible, however, to extract a signal to noise ratio (S/N), which allows observations to be compared, and the contributions of each telescope to be evaluated. The S/N is calculated as

$$S/N = \frac{max(ON)}{std(OFF)}, \tag{5.2}$$

where max(ON) is the maximum peak value in the ON region, and std(OFF) is the standard deviation of the OFF region. The combined S/N for each harmonic and each telescope can be well approximated by a sum in quadrature, e.g.,

$$S/N_{total} = \sqrt{S/N_{T2}^2 + S/N_{T3}^2 + S/N_{T4}^2}. \tag{5.3}$$

For most Crab pulsar observations, T1 is saturated because it is set to a lower sampling rate of 1200 Hz (which is the standard ECM configuration) and therefore has a longer integration time. Though it was discussed in Section 2.3 that the ECM cannot take independent samples above 1200 Hz, the integration time remains at 1/2400 s, which helps avoid saturation. Because of saturation, T1 is excluded from the Crab pulsar analyses in this work and from Eq. 5.3.

Figure 5.8 shows the L-S periodogram for a 30 minute, single telescope observation of the Crab pulsar. It can be seen that there is a considerable offset of the peak height from the pulse frequency obtained from Jodrell Bank. This is due to the spin-down of the pulsar as well as the drift in the ECM clocks.

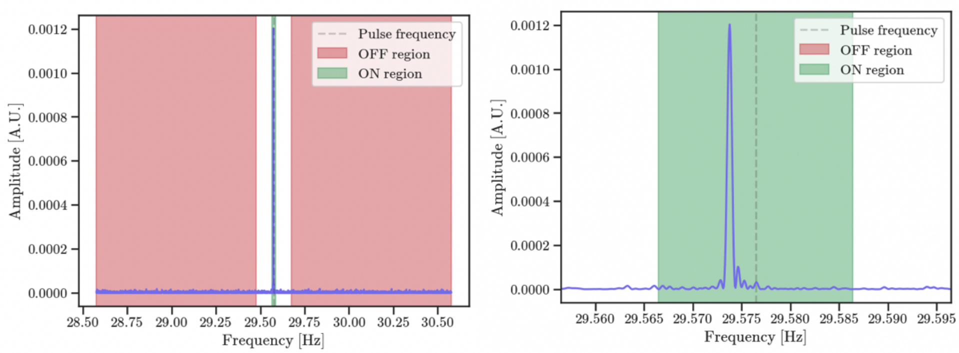

Figure 5.8: Lomb-Scargle periodograms for the Crab pulsar. The full analysis region is shown on the left, and a zoomed-in version showing the

$$ON$$

region is shown on the right. The pulse frequency can clearly be seen as the sharp peak in both figures.

The results for the S/N calculations for all ECM runs can be found in Table 5.3. Each Crab pulsar run is named after the date the data were taken, with runs marked (1) and (2) corresponding to the first and second runs of the night, respectively, if more than one Crab pulsar run was taken.

ECM Run	Usable Time [s]	T2 S/N	T3 S/N	T4 S/N	Combined S/N
20180117[1]	800	175	153	152	264
20221125 (1)	1700	2816	4210	2736	5756
20221125 (2)	1680	2428	4042	2743	5456
20230120 (1)	1670	2521	4643	2662	5916
20230120 (2)	1660	2207	4061	2549	5279
20230212	1720	3370	5628	2614	7062
20230216[2]	1710	2301	4348	2792	5657
20230217[2]	1710	3257	3504	3227	5771
20230319[2,3]	1260	1407	3100	1924	3910

Table 5.3: S/N calculated for all ECM Crab runs using the first three harmonics of the pulsar period. Runs labeled [1] are taken at a sampling rate of 300 Hz (the default sampling rate is 2400 Hz). Runs labeled [2] are taken at a sampling rate of 4800 Hz . Runs labelled [3] are taken in G10 mode, where the ECM digitization is 1.55×10^{-5} V.

For all runs during the 2022-2023 observing season, T2 systematically detects higher S/N for the Crab pulsar. The reason for T2's higher S/N is not currently understood and will be investigated in future work. Figure 5.9 shows the distribution of the cumulative significances for each run. The jumps and drops in each curve are likely originating from the amplitude of noise peaks in the OFF region of the significance calculation (see Section 3.2) rapidly increasing or decreasing due to NSB fluctuations. The differences in total S/N are believed to originate from attenuation of the pulsar signal due to different NSB conditions, which varies by a factor of ≈ 2 over these runs.

Phase Folding

The ECM data are phase-folded before the cleaning algorithm is applied. Though the cleaning algorithm consistently improves the signal in frequency space, the phase-folded peak amplitude is a factor of two lower than that of the raw data. The period at which each telescope's data is folded is determined from the frequency at which the peak is found in the Lomb-Scargle.

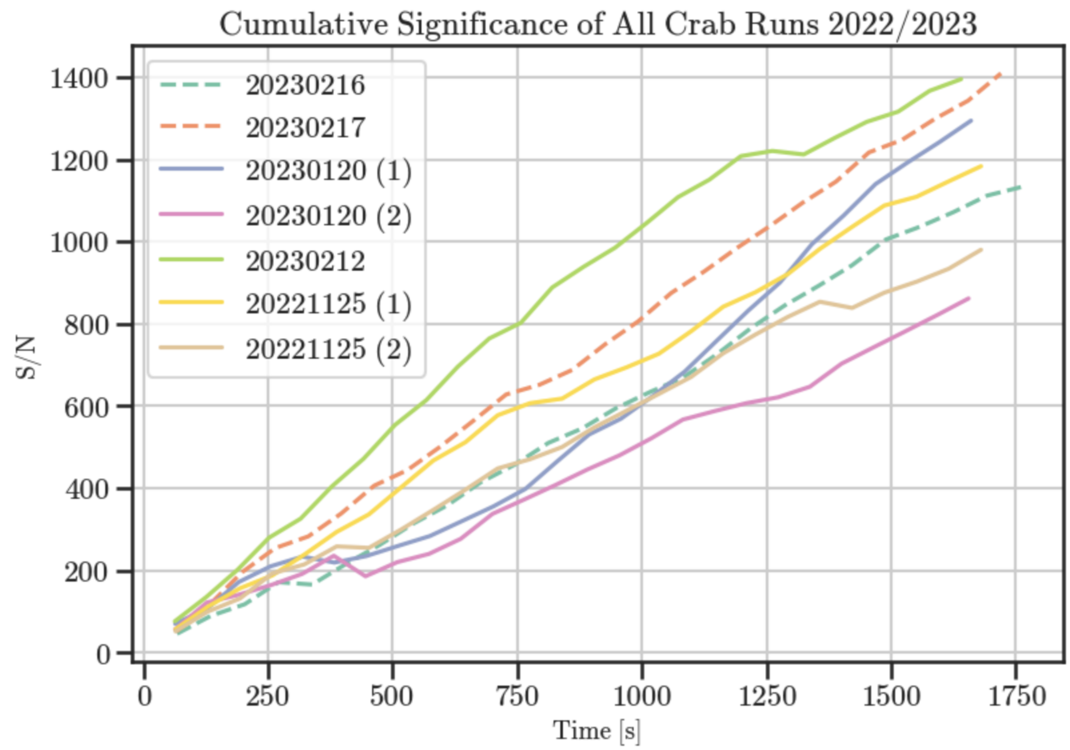

Figure 5.9: Cumulative significance of each Crab pulsar ECM run. The S/N are obtained from 3-telescope combined analysis of the first harmonic only, which accounts for the difference in numerical value than the S/N found in Table 5.3.

Phase folding demands a decently exact and precise measurement of the pulsar period (typically with $\approx \mu s$ uncertainties). The ECM data only produce meaningful phase-folding results when used in pulsar timing packages, like Tempo2, due to large uncertainties in absolute timing. For the Crab pulsar, the lack of timing precision can be mitigated by taking the maximum peak in the Lomb-Scargle periodogram to phase-fold on.

The raw data Crab pulsar phaseogram for a single telescope can be seen in Figure 5.10. The main pulse amplitude of $(5.28 \pm 0.33) \times 10^{-5}$ V corresponds to a visual magnitude of 16.2 ± 1, which is consistent with the V band magnitudes found in [113].

Phase Reconstruction

Compared with phaseograms from other instruments (e.g., [114, 115]), the pulse profile obtained from phase-folding raw ECM data (Figure 5.10) has an apparent broadening on

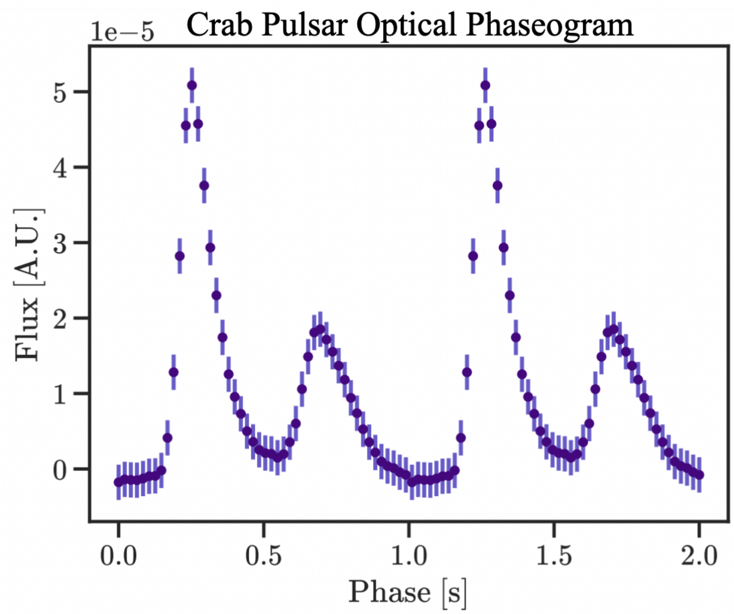

Figure 5.10: Single telescope Crab pulsar phaseogram obtained from phase-folding the raw ECM data. The same phase is shown twice to guide the eye.

the decay side of the pulse (see Figure 5.11). We believes the broadening of ECM signals is due to the settling time issue discussed in Section 2.3.

In order to quantify the settling time, observations of a series of laser pulses from the Cloud-Aerosol Lidar and Infrared Pathfinder Satellite Observation (CALIPSO) satellite [116] that were observed with the ECM were used. CALIPSO emits laser pulses that are ≈ 20 ns long at a wavelength of 532 nm in order to measure the structure and distribution of clouds and aerosols in the Earth's atmosphere. Eight of these pulses were visible during the ECM data taking run, which are shown with their best fit exponential decay functions in Figure 5.12. A settling time of 2.9 ms or a decay constant of $\lambda = 349$ was obtained from these fits.

Additionally, the 2.9 ms settling time is consistent with the Crab pulsar measurement, which is obtained from the convolution of an exponential with decay time 2.9 ms with the Aqueye phaseogram [115] (see Figure 5.13).

If the decay time of the Crab pulsar should roughly match the rise time, as seen in the Aqueye profile of Figure 5.13, we would expect a decay time of 0.001 ms or a decay

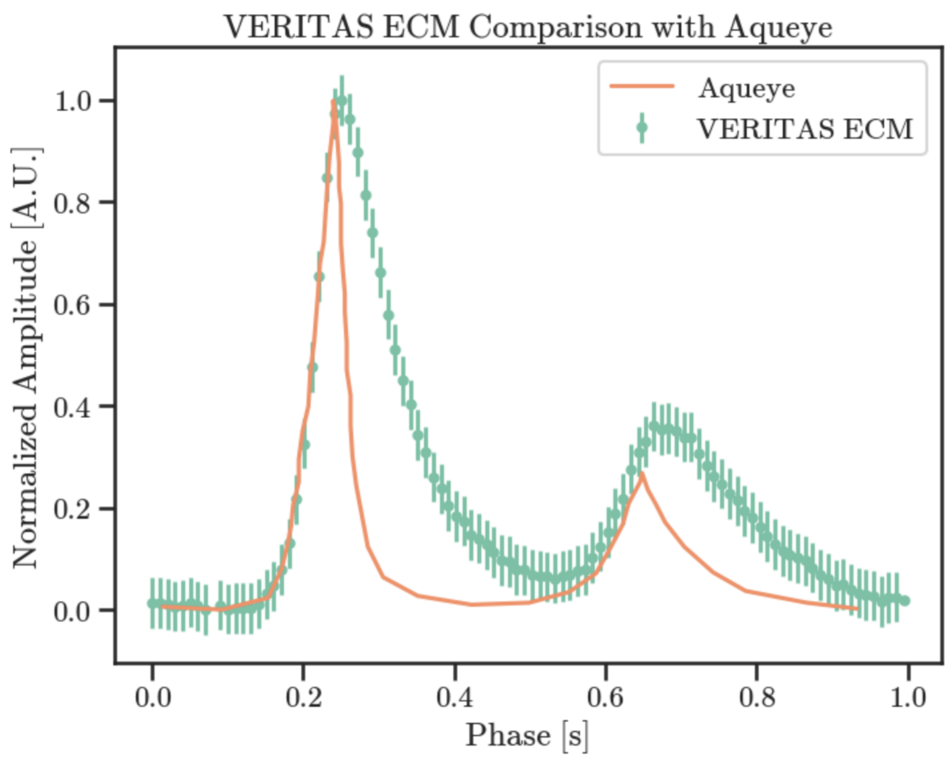

Figure 5.11: Comparison of the ECM and Aqueye [115] Crab pulsar phaseograms. The broadening of the ECM pulse compared to the Aqueye pulse is apparent. Though it is possible that Aqueye has its own settling time constant, this constant is negligible compared to that of the ECM, as is evident in the figure.

constant of $\lambda = 998$. This decay constant is 2.85 times larger than that of the observed ECM decay. This would correspond to a sampling rate of

$$\frac{4800\text{Hz}}{2.85} = 1684 \text{ Hz}. \tag{5.4}$$

This corresponds to where the ECM significance curve (see Figure 2.12) begins to flatten, therefore corroborating our claim that the highest reliable ECM sampling rate is 1200 Hz.

Therefore, the shape of the Crab pulsar's main pulse in the ECM data can be improved by applying a de-convolution algorithm to the binned phaseogram, removing the broadening of the peak due to instrumental settling time.

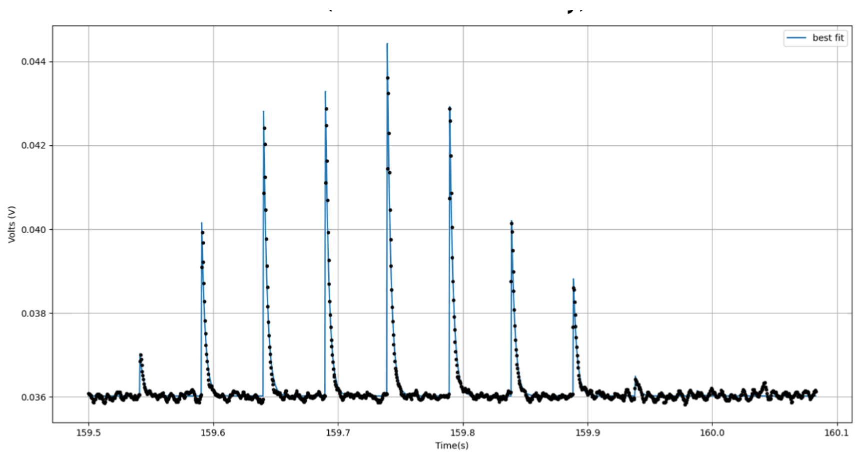

Figure 5.12: CALIPSO pulses seen by the ECM fit with exponential functions with a decay time of 2.9 ms.

The de-convolution algorithm fits the following function to the binned, phase-folded data to recover the underlying Lorentzian pulse shape

$$F = \left[\frac{A_1}{1+((t-x_1)/0.5w_1)^2} + \frac{A_2}{1+((t-x_2)/0.5w_2)^2} + d\right] * \left[A_1 exp\left(\frac{|t-x_1|}{t_{rise,decay}}\right) + A_2 exp\left(\frac{|t-x_2|}{t_{rise,decay}}\right)\right], \quad (5.5)$$

where $A_{1,2}$ are the peak amplitudes, $x_{1,2}$ are the peak offsets, $w_{1,2}$ are the Lorentzian widths, $t_{rise_{1,2}}$ represent the steepness of the rise time of the exponential (which is set to be infinitely steep, to machine precision), and $t_{decay_{1,2}}$ is the instrumental settling time in phase space. The python package `emcee` [117] is used to fit the model to the phase-folded data using a Markov chain Monte Carlo. The best-fit parameters for $A_{1,2}$, $x_{1,2}$, and w can be re-inserted into the 'true' pulse profile

$$pulse = \frac{A_1}{1+((t-x_1)/0.5w_1)^2} + \frac{A_2}{1+((t-x_2)/0.5w_2)^2} + d \quad (5.6)$$

to obtain a de-convolved pulse. The interpulse is not well modelled by an Lorentzian function, so some of its amplitude is not recovered using the de-convolution algorithm.

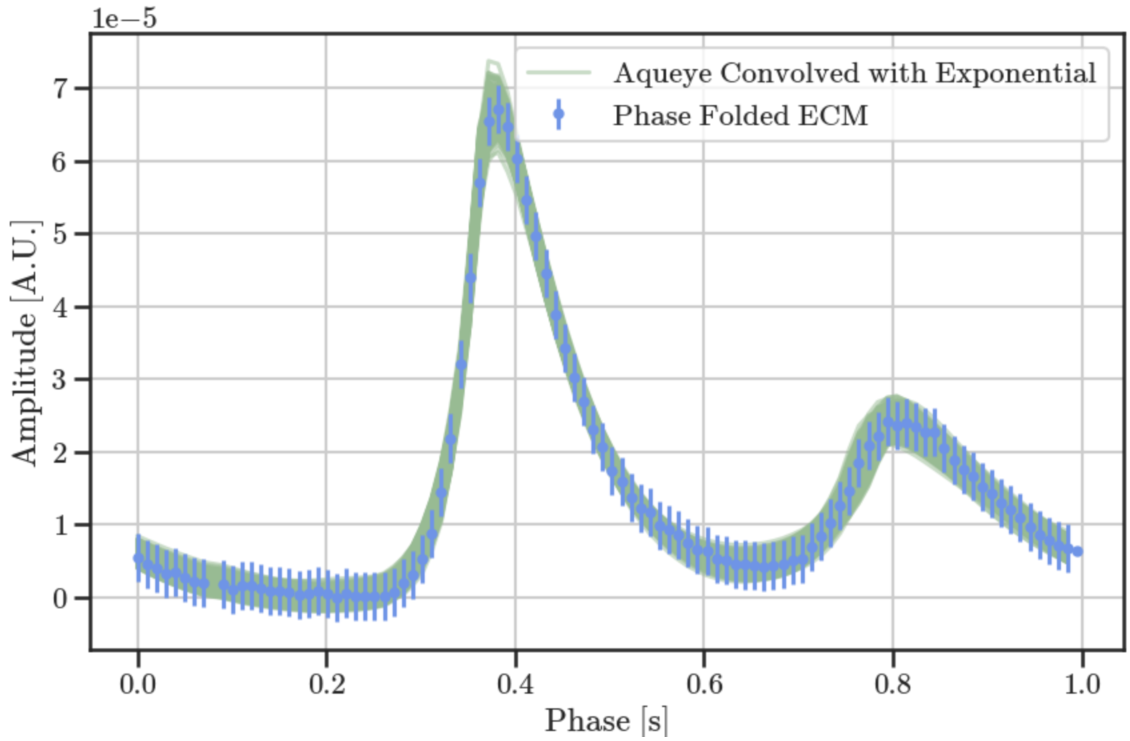

Figure 5.13: Best-fit of the Aqueye Crab pulsar data convolved with an exponential function consistent with the ECM settling time (2.9 ms). The error region (green) is given by the last 1000 fits given by the Markov Chain Monte Carlo (MCMC).

The de-convolved pulse profile is shown in Figure 5.14 and the shape of the main pulse is consistent with previous optical observations from [115, 114].

5.3 PSR B1937+21

PSR B1937+21 is the second fastest (and fastest Northern hemisphere) MSP and was the first MSP ever discovered [118]. Several characteristics make PSR B1937+21 a good candidate for VERITAS ECM observations, including giant radio pulses, non-thermal X-ray emission, and a large value of B_{LC} (the magnetic field at the pulsar's light cylinder).

Previous VERITAS observations have targeted PSR B1937+21 for VHE pulsed emission searches. As can be seen in Figure 5.15, the spectrum of the pulsed emission drops

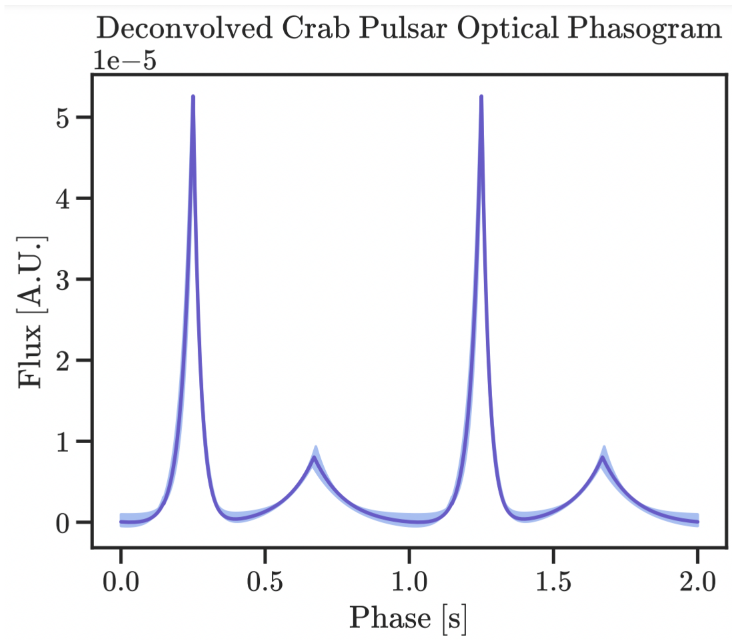

Figure 5.14: Crab pulsar phaseogram deconvolved with ECM response function. The best-fit is the dark blue line and the light blue region represents the uncertainty on the fit.

off rapidly in flux around 10 GeV, well below VERITAS' sensitivity range, therefore we do not expect to see pulsed VHE emission from PSR B1937+21 with VERITAS.

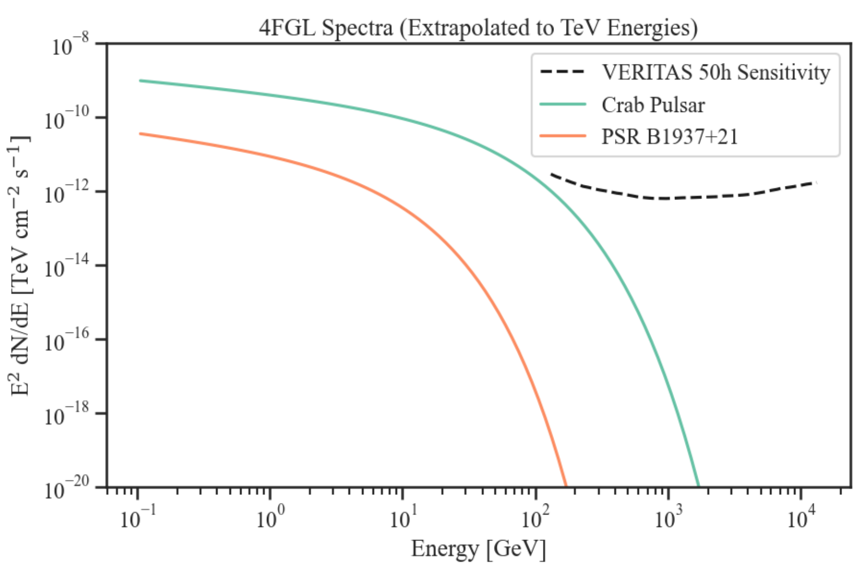

Figure 5.15: *Fermi*-LAT spectrum for PSR B1937+21 extrapolated to the VERITAS energy sensitivity range and compared with the Crab pulsar spectrum.

However, there remains the question as to whether or not steady emission should be expected from PSR B1937+21. Many older pulsars, such as Geminga [50] and Monogem [57] have been found to have extended TeV halos, but it is uncertain as to whether or not TeV haloes should be expected to be found around MSPs as well. While it has been argued that the Galactic centre γ-ray excess originates from MSPs injecting pulsar winds into a dense environment to accelerate particles, there lacks evidence that MSPs can create diffuse emission. Additionally, LHAASO has recently detected UHE emission that is associated with MSP PSR J0218+4232 [60], a MSP that shares many characteristics with PSR B1937+21.

Using data from the High Altitude Water Cherenkov (HAWC) observatory, a VHE survey instrument, [119] find a 3.34σ excess of TeV γ-rays at the point source location of PSR B1937+21. Assuming the same extension as Geminga at the pulsar's distance of 3.5 kpc, a TeV halo should appear as a point source to HAWC. However, repeating a similar search, assuming a more extended TeV halo (evolution of PWN and TeV halos is not well understood for pulsars older than Geminga or MSPs thought to have evolved in a binary) reveals that the HAWC point source emission may just be a hot spot in a region of very extended emission likely originating from nearby source HESS J1943+213. (see Figure 5.16). The aforementioned searches were conducted using HAWC's online tool[1], based on the 3HWC survey [120].

Although it seems unlikely that the HAWC excess originates from PSR B1937+21 itself, more detailed studies using IACTs (which have higher angular resolution than HAWC) are perhaps merited to look for emission that is not source confused with HESS J1943+213.

5.3.1 Observations

Though 10 hours of VERITAS ECM observations were requested for the September 2022 - June 2023 observation season, only 30 minutes of data were taken on PSR B1937+21. The quality of these data are fairly poor, because these 30 minutes of data were the last data

[1]https://data.hawc-observatory.org/datasets/3hwc-survey/coordinate.php

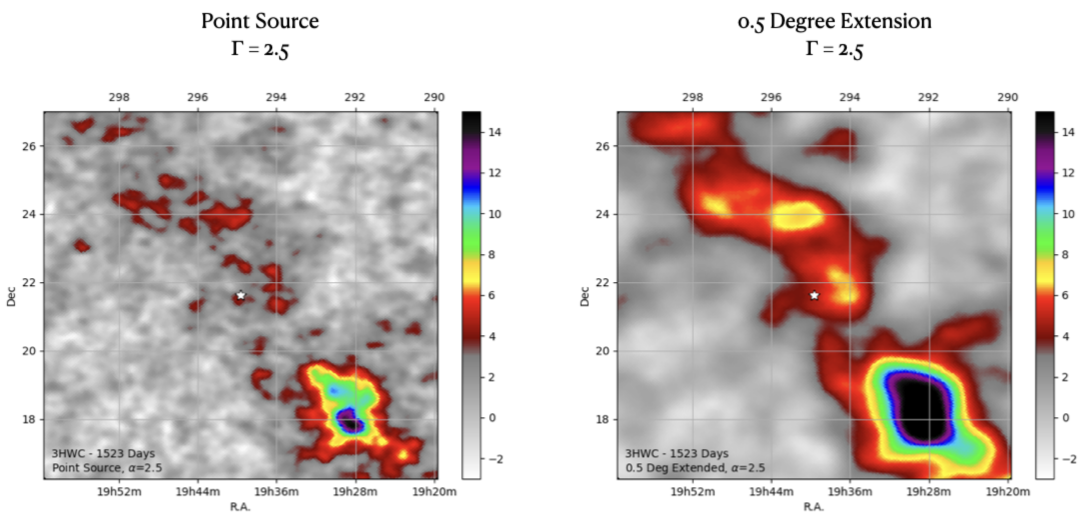

Figure 5.16: HAWC sky maps for the location of PSR B1937+21 (denoted by a white star) for point-like extension (left) and $0.5°$ extension (right). Both analyses are for a Crab-like energy spectrum.

taking run of the night, and the rising sun caused very high NSB levels during the second half of the run (see Figure 5.17). Though even with good data, the pulsar would not be visible with 30 minutes of data (and it remains unclear whether or not PSR B1937+21 will be visible with longer exposures; see Section 4.2.1), it is still worthwhile analyzing the PSR B1937+21 to either confirm or refute that the data behaves as predicted from the simulations discussed in Section 4.2.1.

The following analyses use an ephemeris obtained from the CHIME/Pulsar team via private communications.

5.3.2 γ-ray Analysis

For this work, the γ-ray data are only used to search for pulsed emission. Following from the above discussion, it is necessary to constrain the extension and spectral index of the expected TeV halo or PWN emission more before attempting a γ-ray analysis of the nebula. Multiple searches using different assumptions will create trials factors, which will decrease the significance of any excess that is seen in a given trial.

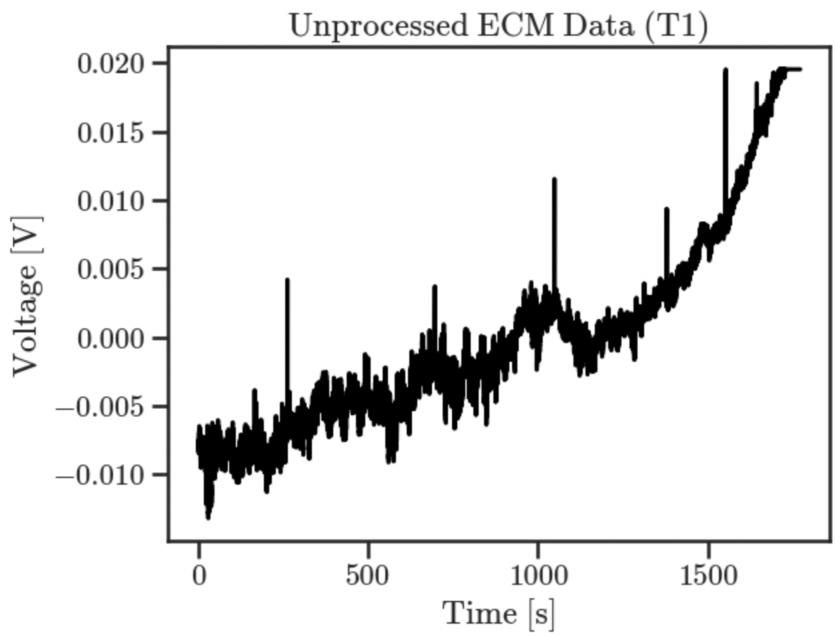

Figure 5.17: Example of one telescope unprocessed ECM data for the single data taking run of PSR B1937+21. T2, T3, and T4 look similar. The rising ECM voltage is due to the Sun rising, since these data were taken at the end of the night.

After data quality cuts, 28 of the 30 minute exposure is usable for γ-ray analysis. Following the standard Eventdisplay analysis described in section 3.1 with supersoft cuts (described in Table 3.2), only six events are labelled as excess events after image quality and γ/hadron separation cuts. There are not enough counts to perform a statistically significant search for pulsed emission.

Although no evidence for pulsed emission is expected even after over a hundred times the available exposure time, the γ-ray analysis was useful for testing the ephemeris obtained from CHIME/Pulsar using data with GPS timestamps, especially given that the ephemeris is only valid up until MJD 60025 and observations were taken on MJD 60124. Since MSPs are generally very stable and have low spin-down rates ($\dot{P} = -4.33 \times 10^{-14}$ s/s for PSR B1937+21), the ephemeris is valid to well below ECM timing precision for the observation date.

A future γ-ray analysis may be conducted if more data are collected on PSR B1937+21 in order to place an upper limit on the VHE flux. This would help constrain whether the

T1 p-value	T2 p-value	T3 p-value	T4 p-value	Combined Significance [σ]
0.4	0.72	0.71	0.68	1.1

Table 5.4: Individual telescope p-values and combined significance (see Section 3.2.4) for PSR B1937+21 ECM data.

VHE emission is consistent with the *Fermi*-LAT extrapolation shown in Figure 5.15 or if the source has a spectral shape that extends into VERITAS' sensitivity range, as seen with the Crab pulsar's broken power law fit in Figure 5.4.

5.3.3 Optical Analysis

In order to extract as much information as possible from the limited dataset, no time cuts are applied for the optical analysis. However, it should be noted that, if combined with higher quality data in future work, all data with $t > 1000$ s should be omitted, because the increasing NSB magnitude likely buries any pulsed signals, lowering the overall cumulative significance during the run.

The ECM data were run through the OOPS-E optical analysis pipeline, as described in Section 3.2. Harmonic stacking was not used for this analysis because the first harmonic frequency is already above the Nyquist limit, so sampling to higher frequencies will produce increasingly unreliable results. Using simulated data of a pulse with the same width and period as PSR B1937+21 but larger amplitude (smaller magnitude) found that the second and third harmonic were not visible in ten hours of data.

The four telescope combined significance of these data is calculated to be 1.1σ (see Table 5.4). Compared to half an hour of simulated PSR B1937+21 data injected into a half hour background run (with better data quality), a 1.6σ significance would be expected, with 2.1σ expected for the background run without injected signal. The higher significance of the background data for small exposure times was discussed in Section 4.2.1 but is not currently well understood. The Lomb-Scargle periodograms from which the significances are calculated are shown in Figure 5.18.

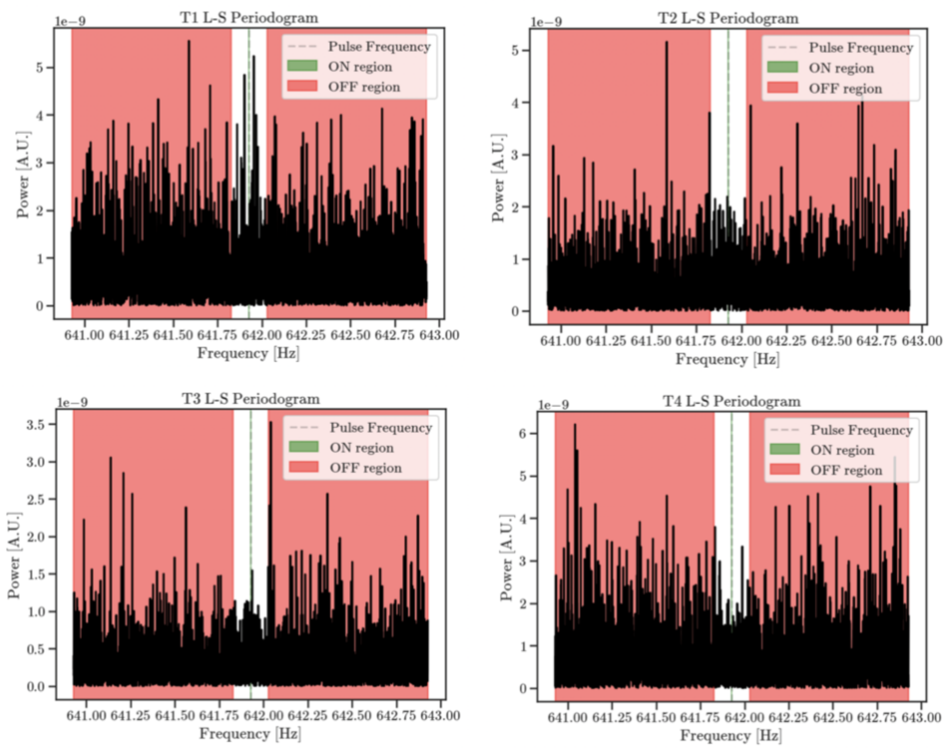

Figure 5.18: Lomb-Scargle periodograms of PSR B1937+21 ECM data.

Phase folding the pre-cleaned PSR B1937+21 data does not show any evidence for a pulsed signal (see Figure 5.19). A constant function: $y = 6.6 \times 10^{-10} \pm 9.79 \times 10^{-8}$ V can be fit to the data with a χ^2/d.o.f value of 0.31 for 48 degrees of freedom. The uncertainties shown in Figure 5.19 represent the standard error of each bin

$$Error = \frac{std(counts)}{\sqrt{N_{counts}}}, \tag{5.7}$$

where $counts$ are the values contained in each phase bin and N_{counts} are the number of counts in each phase bin. The systematic uncertainties on the mean of each bin (corresponding to the datapoints shown in Figure 5.19) are too small to be shown and are of order $\approx 10^{-8}$.

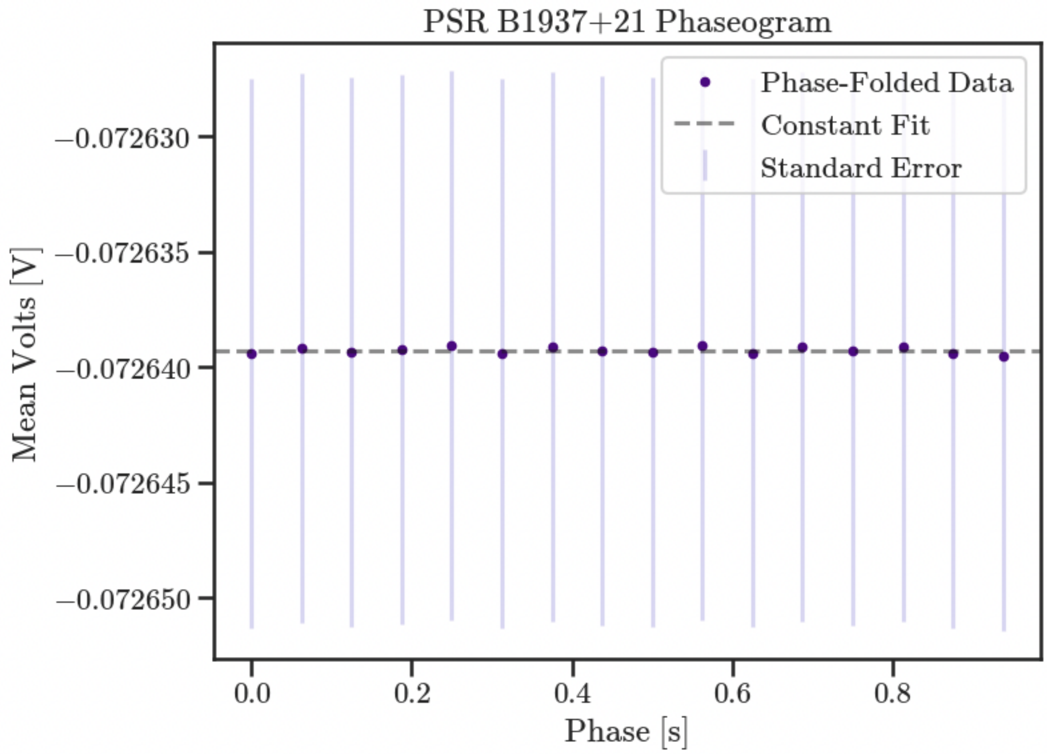

Figure 5.19: Phaseogram of ECM data for PSR B1937+21. Due to the ECM settling time and rapid pulse period of PSR B1937+21, the phase bins are believed to be correlated with each other, leading to lower scatter than expected.

5.4 Analysis Conclusions

To summarize, the sources analyzed in this work are the Crab pulsar and nebula and PSR B1937+21. Both optical and VHE analyes are conducted, which can be summarized as follows:

- The Crab nebula (unpulsed) is detected in VHE γ-rays at a significance of 89σ (see Figure 5.3).
- The Crab pulsar's interpulse is clearly detected in VHE at 7.6σ and there is strong evidence for the existence of the main pulse at 4.3σ.

- The Crab pulsar is detected to optically at a significance of $> 8\sigma$ and at a signal to noise ratio of ≈ 5000. The phase-folded ECM data main pulse peak corresponds to an apparent magnitude of 16 ± 1.

- PSR B1937+21 is neither detected in VHE nor optically. The source is not expected to be visible to VERITAS at all in VHE (see Figure 5.15), and insufficient observations were obtained to find evidence for an optical signal (which may be distinguishable from background noise after ≈ 10h of observations; see Table4.3.

If more data are taken on PSR B1937+21 in future observing seasons, a search for the PWN will be conducted, as well as limits on or evidence for the existence of optical pulsed emission.

Chapter 6

Future Work & Conclusions

6.1 Future Work

We have obtained a 10 hour allocation of VERITAS observing time during the 2023-2024 observing season for PSR J2229+6114 and hope to fill the remaining 9.5 hour allocation for PSR B1937+21 when it is visible to VERITAS during the late spring months. These observations will be useful in order to determine the accuracy of the predictions discussed in Section 4.1. While few optical pulsars have been detected in optical wavelengths, particularly in the fast period parameter space to which the ECM is sensitive, it remains difficult to make accurate predictions without observations.

We would also like to observe the transitional millisecond pulsar (tMSP) PSR J1023+0038 when it is in an accretion high state (see Section 4.1 for more details) to test the ECM sensitivity to MSPs, in order to determine if the predictions in Section 4.1 can be improved upon.. It is also possible that other similar systems exist, which were previously ignored by this study because we focused only on non-accreting X-ray pulsars. Studies of such systems could lead to the discovery of more tMSPs in optical wavelengths

Finding or developing better models for pulsed optical emission will also be important for future studies. Though scaling relations like those used in Section 4.1 are sufficient estimates for ranking most pulsars in terms of their overall energetics, even small errors in magnitude estimates can lead to very different predicted ECM detection outcomes. In future work, we plan to look further into the connection between X-ray and optical flux, and whether non-thermal X-ray spectra of pulsed emission can reliably be extrapolated to optical wavelengths. Additionally, we plan to improve predictions for MSPs to better understand any connections between the emission characteristics of fast, isolated pulsars (e.g., the Crab pulsar) and MSPs.

Follow-up observations for sources in the 1LHAASO catalog [60] are currently also being organized. Many of these sources are associated with pulsars and are thought to be PWNe or TeV halos. These follow-up observations will provide new insight into the morphology and evolution of PWNe/TeV halos. Several of these observations should be possible to take jointly with the ECM in order to investigate optical pulses from the pulsar simultaneously.

For 1LHAASO sources as well as future PWN/TeV halo searches, it will be important to improve our understanding of how the environment around pulsars changes as they age, especially for MSPs. This will likely require complicated particle-in-cell (PIC) simulations or perhaps may be understood from studies of HAWC and LHAASO detected sources. Future searches for VHE emission near PSR B1937+21 will be conducted once it is more certain what the extension and spectrum of the emission should look like.

Instrumentally, there is ongoing work to better understand the origin of the ECM settling time (see Section 2.3). If the settling time is resolved such that a sampling rate of 4800 Hz can be achieved, the observation times needed for sources to be detected will decrease. Additionally, better phase reconstruction of the Crab pulsar and potentially other bright sources can be obtained.

6.2 Optical Upgrades

An upgrade to the VERITAS FADCs will be underway shortly that should enable optical observations to be taken in every pixel, concurrently with all VHE observations. This upgrade will also increase the sampling rate of optical observations to $\approx$ MHz and link the optical observations with the GPS clock used for VHE observations, allowing for much better absolute timing and timing resolution. This upgrade should further increase VERITAS' optical sensitivity to fast pulsars and MSPs, as well as facilitate phase reconstruction and provide much higher resolution in frequency space.

Over the next observing season, a smaller upgrade will be undertaken to add Johnson-Cousins B-band filters to the ECM-connected pixel and add a light shield to the pixel in order to reduce the magnitude of the NSB. This upgrade aims to reduce noise from the NSB and allow the ECM to be set to a higher gain mode, which reduces the magnitude of the digitization steps by a factor of ten. Since most optical pulsar pulses are estimated to be at voltages lower than the digitization limit of the ECM, lowering the digitization step should make it possible to detect pulsars at magnitudes $m_{ECM} < 22$.

6.3 The Future of IACTs and VERITAS

The next generation of IACTs, the Cherenkov Telescope Array (CTA) [121] is an array of 60 telescopes distributed at both a Northern and Southern site with five to ten times the sensitivity of current IACT arrays. Currently one telescope has been fully constructed and is taking data [122] and the rest will be operational by the late 2020s.

CTA has plans to continue observations of rapid optical transients and is currently working with IACT optical experts to develop the necessary technology for these observations. Additionally, for the first time in IACT history, CTA will have an open data policy, meaning that anyone can access and analyze both VHE and optical data.

Although CTA will be a very exciting step forward for both VHE and rapid optical astrophysics, VERITAS is not necessarily out of the picture. With the many exciting upgrades discussed above, VERITAS will remain one of the best performing rapid optical telescopes in the world for the rest of its life, with the advantage of having a less competitive observing program than CTA. Additionally, CTA uses silicon photomultipliers

(SiPMs), as opposed to PMTs, which are sensitive to optical wavelengths from $\approx 400-600$ nm. Since PMTs operate at slightly bluer wavelengths, so the combined use of CTA with VERITAS will allow for at least two spectral points to be calculated in the case of a detection, rather than just a single optical point.

6.4 Conclusions

Optical observations with the VERITAS ECM constitute a novel and exciting use for IACTs. Currently, VERITAS has a significantly larger light collecting area and much faster time resolution than other rapid optical instruments, making it an excellent tool for pushing into the fastest varying end of transient parameter space.

Though pulsars have been studied for over half a century, there still remains uncertainty as to which emission models can describe the observed multi-wavelength emission. Furthermore, pulsars like the Crab pulsar and MSPs PSR B1937+21 and PSR J0218+4232 show interesting characteristics like multi-wavelength phase alignment and giant pulses that are seemingly unique in the broader pulsar population. How these characteristics tie in with other multi-wavelength model uncertainties also remains unresolved and necessitates further observational studies. Optical pulsar studies, particularly those of fast pulsars, such as young Crab-like sources and MSPs, have likely not been conducted to their full potential, mainly due to instrumental limitations. Though the ECM is still limited by the intrinsic optical faintness of many pulsars, the predictions done in this work show that it is perhaps possible to detect new optical pulsars.

The first catalog of LHAASO sources [60] has also re-ignited an interest in pulsar sources in the VHE community. Many of the largest and most energetic VHE sources in the Galaxy seem to be associated with pulsars. It may be pulsars and their environments that provide the best laboratories for studying particles at the highest energies ever observed. Understanding the mechanisms by which the observed γ-rays in these systems are produced will also help constrain the origin of the UHE cosmic-ray flux we detect on

Earth. Simultaneous γ-ray and optical ECM observations facilitate the accomplishment of multiple science goals in a single observation program.

Though it has been over sixty years since the first pulsar was discovered and over seventeen years of VERITAS observations, there still remain many open questions about pulsars, VHE astrophysics, and the overlap of both. With optical upgrades coming soon to VERITAS and CTA coming online within the next decade, there will be a lot of (Cherenkov and optical) light shed on the questions that remain open in this thesis, hopefully resulting in some exciting new discoveries in the near future.

Bibliography

[1] A. Hewish et al. "Observation of a Rapidly Pulsating Radio Source". *Nature* 217.5130 (Feb. 1968), pp. 709–713. ISSN: 1476-4687. DOI: 10.1038/217709a0. URL: https://doi.org/10.1038/217709a0.

[2] Zhan-Kui Huang and Xin-Ji Wu. "An Estimation of the Initial Period of Pulsars". Chinese J. Astron. Astrophys. 3 (Apr. 2003), pp. 166–174. DOI: 10.1088/1009-9271/3/2/166.

[3] Kyle Kremer et al. "White Dwarf Subsystems in Core-Collapsed Globular Clusters". *The Astrophysical Journal* 917.1 (Aug. 2021), p. 28. DOI: 10.3847/1538-4357/ac06d4. URL: https://dx.doi.org/10.3847/1538-4357/ac06d4.

[4] Thomas M. Tauris, Norbert Langer, and Philipp Podsiadlowski. "Ultra-stripped supernovae: progenitors and fate". *Monthly Notices of the Royal Astronomical Society* 451.2 (June 2015), pp. 2123–2144. ISSN: 0035-8711. DOI: 10.1093/mnras/stv990. eprint: https://academic.oup.com/mnras/article-pdf/451/2/2123/5758766/stv990.pdf. URL: https://doi.org/10.1093/mnras/stv990.

[5] R. N. Manchester et al. "The Australia Telescope National Facility Pulsar Catalogue". AJ 129.4 (Apr. 2005), pp. 1993–2006. DOI: 10.1086/428488. arXiv: astro-ph/0412641 [astro-ph].

[6] E. Aliu et al. "Detection of Pulsed Gamma Rays Above 100 GeV from the Crab Pulsar". *Science* 334.6052 (Oct. 2011), pp. 69–72. DOI: 10.1126/science.1208192. URL: https://doi.org/10.1126%5C%20%5C%2Fscience.1208192.

[7] and H. Abdalla et al. “First ground-based measurement of sub-20 GeV to 100 GeV gamma-Rays from the Vela pulsar with H.E.S.S. II”. *Astronomy and Astrophysics* 620 (Dec. 2018), A66. DOI: 10.1051/0004-6361/201732153. URL: https://doi.org/10.1051%2F0004-6361%2F201732153.

[8] M. Pitkin. “psrqpy: a python interface for querying the ATNF pulsar catalogue”. *Journal of Open Source Software* 3.22 (Feb. 2018), p. 538. DOI: 10.21105/joss.00538. URL: https://doi.org/10.21105/joss.00538.

[9] F.C. Michel and W.H. Tucker. “Pulsar emission mechanism”. *Nature* 223.5203 (1969), pp. 277–279.

[10] Roger D. Blandford and Roger W. Romani. “On the interpretation of pulsar braking indices.” MNRAS 234 (Oct. 1988), 57P–60. DOI: 10.1093/mnras/234.1.57P.

[11] C. Alvarez and A. Carrami nana. “Monopolar Pulsar Spin-Down”. *Astronomy & Astrophysics* 414.2 (Feb. 2004), pp. 651–658. ISSN: 0004-6361, 1432-0746. DOI: 10.1051/0004-6361:20031627. URL: http://www.aanda.org/10.1051/0004-6361:20031627 (visited on 06/28/2023).

[12] Cristobal M. Espinoza. “The Spin Evolution of Young Pulsars”. *Proceedings of the International Astronomical Union* 8.S291 (Aug. 2012), pp. 195–198. ISSN: 1743-9213, 1743-9221. DOI: 10.1017/S1743921312023629. arXiv: 1211.5276 [astro-ph]. URL: http://arxiv.org/abs/1211.5276 (visited on 06/09/2023).

[13] Bing Zhang, Alice K. Harding, and Alexander G. Muslimov. “Radio Pulsar Death Line Revisited: Is PSR J2144-3933 Anomalous?” *The Astrophysical Journal* 531.2 (Mar. 2000), pp. L135–L138. DOI: 10.1086/312542. URL: https://doi.org/10.1086%2F312542.

[14] Zhan-Kui Huang and Xin-Ji Wu. “An Estimation of the Initial Period of Pulsars”. *Chinese Journal of Astronomy and Astrophysics* 3.2 (Apr. 2003), pp. 166–174. ISSN:

1009-9271. DOI: 10.1088/1009-9271/3/2/166. URL: https://iopscience.iop.org/article/10.1088/1009-9271/3/2/166 (visited on 06/09/2023).

[15] F. Ambrosino et al. "Optical pulsations from a transitional millisecond pulsar". *Nature Astronomy* 1.12 (Oct. 2017), pp. 854–858. DOI: 10.1038/s41550-017-0266-2. URL: https://doi.org/10.1038%2Fs41550-017-0266-2.

[16] F. Pacini and M. Salvati. "On the Evolution of Supernova Remnants. Evolution of the Magnetic Field, Particles, Content, and Luminosity". ApJ 186 (Nov. 1973), pp. 249–266. DOI: 10.1086/152495.

[17] VERITAS Collaboration et al. "Detection of Pulsed Gamma Rays Above 100 GeV from the Crab Pulsar". *Science* 334.6052 (Oct. 2011), pp. 69–72. ISSN: 0036-8075, 1095-9203. DOI: 10.1126/science.1208192. arXiv: 1108.3797 [astro-ph]. URL: http://arxiv.org/abs/1108.3797 (visited on 06/09/2023).

[18] J. K. Daugherty and A. K. Harding. "Gamma ray pulsars: Extended polar CAP cascades from nearly aligned rotators." A&AS 120 (Nov. 1996), pp. 107–110.

[19] Roger W. Romani. "Gamma-Ray Pulsars: Radiation Processes in the Outer Magnetosphere". *The Astrophysical Journal* 470 (Oct. 1996), p. 469. ISSN: 0004-637X. DOI: 10.1086/177878. URL: https://ui.adsabs.harvard.edu/abs/1996ApJ...470..469R (visited on 06/11/2023).

[20] K. S. Cheng, C. Ho, and M. Ruderman. "Energetic Radiation from Rapidly Spinning Pulsars. II. VELA and Crab". *The Astrophysical Journal* 300 (Jan. 1986), p. 522. ISSN: 0004-637X. DOI: 10.1086/163830. URL: https://ui.adsabs.harvard.edu/abs/1986ApJ...300..522C (visited on 06/11/2023).

[21] J. Arons. "Pair Creation above Pulsar Polar Caps : Geometrical Structure and Energetics of Slot Gaps." *The Astrophysical Journal* 266 (Mar. 1983), pp. 215–241. ISSN: 0004-637X. DOI: 10.1086/160771. URL: https://ui.adsabs.harvard.edu/abs/1983ApJ...266..215A (visited on 06/11/2023).

[22] P Goldreich and W H Julian. "PULSAR ELECTRODYNAMICS." *Astrophys. J., 157: 869-80(Aug. 1969).* (Jan. 1969). DOI: 10.1086/150119. URL: https://www.osti.gov/biblio/4776086.

[23] S. Abdollahi et al. "Incremental Fermi Large Area Telescope Fourth Source Catalog". *The Astrophysical Journal Supplement Series* 260.2 (June 2022), p. 53. DOI: 10.3847/1538-4365/ac6751. URL: https://doi.org/10.3847%2F1538-4365%2Fac6751.

[24] John Sampson Toll. "The Dispersion Relation for Light and its Application to Problems Involving Electron Pairs." PhD thesis. Princeton University, New Jersey, Jan. 1952.

[25] A. A. Abdo et al. "FERMI LARGE AREA TELESCOPE OBSERVATIONS OF THE VELA PULSAR". *The Astrophysical Journal* 696.2 (Apr. 2009), pp. 1084–1093. DOI: 10.1088/0004-637x/696/2/1084. URL: https://doi.org/10.1088%5C%20%5C%2F0004-637x%5C%20%5C%2F696%5C%20%5C%2F2%5C%20%5C%2F1084.

[26] A. A. Abdo et al. "The First Fermi Large Area Telescope Catalog of Gamma-ray Pulsars". ApJS 187.2 (Apr. 2010), pp. 460–494. DOI: 10.1088/0067-0049/187/2/460. arXiv: 0910.1608 [astro-ph.HE].

[27] F. C. Michel. "Vacuum gaps in pulsar magnetospheres." ApJ 227 (Jan. 1979), pp. 579–589. DOI: 10.1086/156768.

[28] J. G. Kirk, O. Skjæraasen, and Y. A. Gallant. "Pulsed radiation from neutron star winds". *Astronomy and Astrophysics* 388.2 (May 2002), pp. L29–L32. DOI: 10.1051/0004-6361:20020599. URL: https://doi.org/10.1051%5C%20%5C%2F00046361%5C%20%5C%3A20020599.

[29] Kouichi Hirotani. *High Energy Emission from Rotation-Powered Pulsars: Outer-gap vs. Slot-gap Models*. 2008. arXiv: 0809.1283 [astro-ph].

[30] Maxim Lyutikov, Nepomuk Otte, and Andrew McCann. "THE VERY HIGH ENERGY EMISSION FROM PULSARS: A CASE FOR INVERSE COMPTON SCATTERING". *The Astrophysical Journal* 754.1 (July 2012), p. 33. DOI: 10.1088/0004-637X/754/1/33. URL: https://dx.doi.org/10.1088/0004-637X/754/1/33.

[31] Mikhail A Belyaev. "PICsar: Particle in cell pulsar magnetosphere simulator". *Astrophysics Source Code Library* (2016), ascl–1607.

[32] K. Liu et al. "Variability, polarimetry, and timing properties of single pulses from PSR J1713+0747 using the Large European Array for Pulsars". *Monthly Notices of the Royal Astronomical Society* 463.3 (Sept. 2016), pp. 3239–3248. ISSN: 0035-8711. DOI: 10.1093/mnras/stw2223. eprint: https://academic.oup.com/mnras/article-pdf/463/3/3239/18243265/stw2223.pdf. URL: https://doi.org/10.1093/mnras/stw2223.

[33] Andrew Lyne and Francis Graham-Smith. *Pulsar Astronomy*. 4th ed. Cambridge Astrophysics. Cambridge University Press, 2012. DOI: 10.1017/CBO9780511844584.

[34] Krzysztof Maciesiak, Janusz Gil, and Valério A. R. M. Ribeiro. "On the pulse-width statistics in radio pulsars – I. Importance of the interpulse emission". *Monthly Notices of the Royal Astronomical Society* 414.2 (June 2011), pp. 1314–1328. ISSN: 0035-8711. DOI: 10.1111/j.1365-2966.2011.18471.x. eprint: https://academic.oup.com/mnras/article-pdf/414/2/1314/17328161/mnras0414-1314.pdf. URL: https://doi.org/10.1111/j.1365-2966.2011.18471.x.

[35] J. A. Gil, J. Kijak, and J. H. Seiradakis. "On the two-dimensional structure ofp pulsar beams." A&A 272 (May 1993), pp. 268–276.

[36] A. G. Lyne and R. N. Manchester. "The shape of pulsar radio beams." MNRAS 234 (Oct. 1988), pp. 477–508. DOI: 10.1093/mnras/234.3.477.

[37] N. D. R. Bhat et al. "The Southern-sky MWA Rapid Two-metre (SMART) pulsar survey—II. Survey status, pulsar census, and first pulsar discoveries". *Publications of the Astronomical Society of Australia* 40 (2023). DOI: 10.1017/pasa.2023.18. URL: https://doi.org/10.1017%2Fpasa.2023.18.

[38] Alice K. Harding. *Pulsar High-Energy Emission From the Polar Cap and Slot Gap*. Oct. 2007. arXiv: 0710.3517 [astro-ph]. URL: http://arxiv.org/abs/0710.3517 (visited on 06/12/2023).

[39] T. C. Weekes et al. "Observation of TeV Gamma Rays from the Crab Nebula Using the Atmospheric Cerenkov Imaging Technique". ApJ 342 (July 1989), p. 379. DOI: 10.1086/167599.

[40] Bryan M. Gaensler and Patrick O. Slane. "The Evolution and Structure of Pulsar Wind Nebulae". *Annual Review of Astronomy and Astrophysics* 44.1 (Sept. 2006), pp. 17–47. DOI: 10.1146/annurev.astro.44.051905.092528. URL: https://doi.org/10.1146%2Fannurev.astro.44.051905.092528.

[41] Gilles Ferrand and Samar Safi-Harb. "A census of high-energy observations of Galactic supernova remnants". *Advances in Space Research* 49.9 (May 2012), pp. 1313–1319. DOI: 10.1016/j.asr.2012.02.004. arXiv: 1202.0245 [astro-ph.HE].

[42] George R. Blumenthal. "Spectrum of High-Energy Electrons Undergoing Klein-Nishina Losses". Phys. Rev. D 3.10 (May 1971), pp. 2308–2311. DOI: 10.1103/PhysRevD.3.2308.

[43] and Zhen Cao et al. "Peta–electron volt gamma-ray emission from the Crab Nebula". *Science* 373.6553 (July 2021), pp. 425–430. DOI: 10.1126/science.abg5137. URL: https://doi.org/10.1126%5C%20%5C%2Fscience.abg5137.

[44] Victor Hess. *On the Observations of the Penetrating Radiation during Seven Balloon Flights*. 2018. arXiv: 1808.02927 [physics.hist-ph].

[45] Barbara Olmi and Niccolò Bucciantini. "From Young to Old: The Evolutionary Path of Pulsar Wind Nebulae". *Publications of the Astronomical Society of Australia* 40 (2023), e007. ISSN: 1323-3580, 1448-6083. DOI: 10.1017/pasa.2023.5. arXiv: 2301.12903 [astro-ph]. URL: http://arxiv.org/abs/2301.12903 (visited on 06/11/2023).

[46] J. Kelly Truelove and Christopher F. McKee. "Evolution of Nonradiative Supernova Remnants". ApJS 120.2 (Feb. 1999), pp. 299–326. DOI: 10.1086/313176.

[47] S. P. Reynolds and R. A. Chevalier. "Evolution of Pulsar-Driven Supernova Remnants." *The Astrophysical Journal* 278 (Mar. 1984), pp. 630–648. ISSN: 0004-637X. DOI: 10.1086/161831. URL: https://ui.adsabs.harvard.edu/abs/1984ApJ...278..630R (visited on 07/02/2023).

[48] R Bandiera et al. "Reverberation of pulsar wind nebulae – II. Anatomy of the 'thin-shell' evolution". *Monthly Notices of the Royal Astronomical Society* 520.2 (Jan. 2023), pp. 2451–2472. DOI: 10.1093/mnras/stad134. URL: https://doi.org/10.1093%5C%20%5C%2Fmnras%5C%20%5C%2Fstad134.

[49] G. Hobbs et al. "A statistical study of 233 pulsar proper motions". *Monthly Notices of the Royal Astronomical Society* 360.3 (July 2005), pp. 974–992. DOI: 10.1111/j.1365-2966.2005.09087.x. URL: https://doi.org/10.1111%2Fj.1365-2966.2005.09087.x.

[50] F. Aharonian et al. "Detection of extended gamma-ray emission around the Geminga pulsar with H.E.S.S." *Astronomy and Astrophysics* 673 (May 2023), A148. DOI: 10.1051/0004-6361/202245776. URL: https://doi.org/10.1051%2F0004-6361%2F202245776.

[51] E. van der Swaluw et al. "Pulsar Wind Nebulae in Supernova Remnants. Spherically Symmetric Hydrodynamical Simulations". *Astronomy and Astrophysics* 380 (Dec. 2001), pp. 309–317. ISSN: 0004-6361. DOI: 10.1051/0004-6361:20011437.

URL: https://ui.adsabs.harvard.edu/abs/2001A&A...380..309V (visited on 07/02/2023).

[52] Bryan M. Gaensler and Patrick O. Slane. "The Evolution and Structure of Pulsar Wind Nebulae". ARA&A 44.1 (Sept. 2006), pp. 17–47. DOI: 10.1146/annurev.astro.44.051905.092528. arXiv: astro-ph/0601081 [astro-ph].

[53] A. A. Abdo et al. "Milagro Observations of Multi-TeV Emission from Galactic Sources in the Fermi Bright Source List". ApJ 700.2 (Aug. 2009), pp. L127–L131. DOI: 10.1088/0004-637X/700/2/L127. arXiv: 0904.1018 [astro-ph.HE].

[54] A. U. Abeysekara et al. "The 2HWC HAWC Observatory Gamma-Ray Catalog". *The Astrophysical Journal* 843.1 (June 2017), p. 40. DOI: 10.3847/1538-4357/aa7556. URL: https://doi.org/10.3847%5C%20%5C%2F1538-4357%5C%20%5C%2Faa7556.

[55] Tim Linden et al. "Using HAWC to Discover Invisible Pulsars". *Physical Review D* 96.10 (Nov. 2017), p. 103016. ISSN: 2470-0010, 2470-0029. DOI: 10.1103/PhysRevD.96.103016. URL: https://link.aps.org/doi/10.1103/PhysRevD.96.103016 (visited on 06/11/2023).

[56] Zhen Cao et al. *The Large High Altitude Air Shower Observatory (LHAASO) Science Book (2021 Edition)*. 2022. arXiv: 1905.02773 [astro-ph.HE].

[57] A. U. Abeysekara et al. "Extended gamma-ray sources around pulsars constrain the origin of the positron flux at Earth". *Science* 358.6365 (Nov. 2017), pp. 911–914. DOI: 10.1126/science.aan4880. URL: https://doi.org/10.1126%2Fscience.aan4880.

[58] Carles Badenes, Dan Maoz, and Bruce T. Draine. "On the size distribution of supernova remnants in the Magellanic Clouds". *Monthly Notices of the Royal Astronomical Society* 407.2 (June 2010), pp. 1301–1313. DOI: 10.1111/j.1365-2966.2010.17023.x. URL: https://doi.org/10.1111%2Fj.1365-2966.2010.17023.x.

[59] Takahiro Sudoh, Tim Linden, and John F. Beacom. “TeV halos are everywhere: Prospects for new discoveries”. *Phys. Rev. D* 100 (4 Aug. 2019), p. 043016. DOI: 10.1103/PhysRevD.100.043016. URL: https://link.aps.org/doi/10.1103/PhysRevD.100.043016.

[60] Zhen Cao et al. *The First LHAASO Catalog of Gamma-Ray Sources*. May 2023. arXiv: 2305.17030 [astro-ph, physics:hep-ph]. URL: http://arxiv.org/abs/2305.17030 (visited on 06/09/2023).

[61] J. N. Capdevielle et al. *The Karlsruhe extensive air shower simulation code CORSIKA*. 1992.

[62] G. Sinnis. “Air shower detectors in gamma-ray astronomy”. *New Journal of Physics* 11.5, 055007 (May 2009), p. 055007. DOI: 10.1088/1367-2630/11/5/055007.

[63] W. Galbraith and J. V. Jelley. “Light Pulses from the Night Sky associated with Cosmic Rays”. Nature 171.4347 (Feb. 1953), pp. 349–350. DOI: 10.1038/171349a0.

[64] J. Michael Davies and E. S. Cotton. “Design of the quartermaster solar furnace”. *Solar Energy* 1 (1957), pp. 16–22.

[65] A. McCann et al. “A new mirror alignment system for the VERITAS telescopes”. *Astroparticle Physics* 32.6 (2010), pp. 325–329. ISSN: 0927-6505. DOI: https://doi.org/10.1016/j.astropartphys.2009.10.001. URL: https://www.sciencedirect.com/science/article/pii/S0927650509001455.

[66] T. Nagai et al. “Focal Plane Instrumentation of VERITAS”. *International Cosmic Ray Conference*. Vol. 3. International Cosmic Ray Conference. Jan. 2008, pp. 1437–1440.

[67] Alexander K. Konopelko. “Design studies for the future 50 GeV arrays of imaging air Čerenkov telescopes”. *Astroparticle Physics* 11.1-2 (June 1999), pp. 263–266. DOI: 10.1016/s0927-6505(99)00062-6. URL: https://doi.org/10.1016%2Fs0927-6505%2899%2900062-6.

[68] Jeremy S. Perkins, Gernot Maier, and The VERITAS Collaboration. *VERITAS Telescope 1 Relocation: Details and Improvements*. Dec. 2009. arXiv: 0912.3841 [astro-ph]. URL: http://arxiv.org/abs/0912.3841 (visited on 07/18/2023).

[69] Jamie Holder. *Atmospheric Cherenkov Gamma-ray Telescopes*. Oct. 2015. arXiv: 1510.05675 [astro-ph]. URL: http://arxiv.org/abs/1510.05675 (visited on 07/17/2023).

[70] T. -P. Li and Y. -Q. Ma. "Analysis Methods for Results in Gamma-Ray Astronomy." *The Astrophysical Journal* 272 (Sept. 1983), pp. 317–324. ISSN: 0004-637X. DOI: 10.1086/161295. URL: https://ui.adsabs.harvard.edu/abs/1983ApJ...272..317L (visited on 07/30/2023).

[71] Nahee Park. *Performance of the VERITAS Experiment*. Oct. 2015. arXiv: 1508.07070 [astro-ph]. URL: http://arxiv.org/abs/1508.07070 (visited on 06/11/2023).

[72] Michael S. Bessell. "Standard Photometric Systems". *Annual Review of Astronomy and Astrophysics* 43.1 (2005), pp. 293–336. DOI: 10.1146/annurev.astro.41.082801.100251. eprint: https://doi.org/10.1146/annurev.astro.41.082801.100251. URL: https://doi.org/10.1146/annurev.astro.41.082801.100251.

[73] A.G. Lyne, R.S. Pritchard, and F. Graham Smith. "23 years of Crab pulsar rotational history." MNRAS 265 (Dec. 1993), pp. 1003–1012. DOI: 10.1093/mnras/265.4.1003.

[74] Gaia Collaboration et al. "The Gaia mission". A&A 595, A1 (Nov. 2016), A1. DOI: 10.1051/0004-6361/201629272. arXiv: 1609.04153 [astro-ph.IM].

[75] Gaia Collaboration et al. "Gaia Early Data Release 3. Summary of the contents and survey properties". A&A 649, A1 (May 2021), A1. DOI: 10.1051/0004-6361/202039657. arXiv: 2012.01533 [astro-ph.GA].

[76] Gernot Maier and Jamie Holder. *Eventdisplay: An Analysis and Reconstruction Package for Ground-based Gamma-ray Astronomy*. 2017. arXiv: 1708.04048 [astro-ph.IM].

[77] P. Cogan. *VEGAS, the VERITAS Gamma-ray Analysis Suite*. 2007. arXiv: 0709.4233 [astro-ph].

[78] A. M. Hillas. "Cerenkov Light Images of EAS Produced by Primary Gamma Rays and by Nuclei". *19th International Cosmic Ray Conference (ICRC19), Volume 3*. Vol. 3. International Cosmic Ray Conference. Aug. 1985, p. 445.

[79] R. T. Edwards, G. B. Hobbs, and R. N. Manchester. "tempo2, a new pulsar timing package – II. The timing model and precision estimates". *Monthly Notices of the Royal Astronomical Society* 372.4 (Oct. 2006), pp. 1549–1574. ISSN: 0035-8711. DOI: 10.1111/j.1365-2966.2006.10870.x. eprint: https://academic.oup.com/mnras/article-pdf/372/4/1549/4012423/mnras0372-1549.pdf. URL: https://doi.org/10.1111/j.1365-2966.2006.10870.x.

[80] O. C. de Jager and I. Büsching. "The H-test Probability Distribution Revisited: Improved Sensitivity". *Astronomy and Astrophysics* 517 (July 2010), p. L9. ISSN: 0004-6361, 1432-0746. DOI: 10.1051/0004-6361/201014362. arXiv: 1005.4867 [astro-ph]. URL: http://arxiv.org/abs/1005.4867 (visited on 06/09/2023).

[81] Pauli Virtanen et al. "SciPy 1.0: Fundamental Algorithms for Scientific Computing in Python". *Nature Methods* 17 (2020), pp. 261–272. DOI: 10.1038/s41592-019-0686-2.

[82] Astropy Collaboration et al. "Astropy: A community Python package for astronomy". A&A 558, A33 (Oct. 2013), A33. DOI: 10.1051/0004-6361/201322068. arXiv: 1307.6212 [astro-ph.IM].

[83] Astropy Collaboration et al. "The Astropy Project: Building an Open-science Project and Status of the v2.0 Core Package". AJ 156.3, 123 (Sept. 2018), p. 123. DOI: 10.3847/1538-3881/aabc4f. arXiv: 1801.02634 [astro-ph.IM].

[84] Astropy Collaboration et al. “The Astropy Project: Sustaining and Growing a Community-oriented Open-source Project and the Latest Major Release (v5.0) of the Core Package”. *apj* 935.2, 167 (Aug. 2022), p. 167. DOI: 10.3847/1538-4357/ac7c74. arXiv: 2206.14220 [astro-ph.IM].

[85] William H. Press and George B. Rybicki. “Fast Algorithm for Spectral Analysis of Unevenly Sampled Data”. ApJ 338 (Mar. 1989), p. 277. DOI: 10.1086/167197.

[86] N. R. Lomb. “Least-Squares Frequency Analysis of Unequally Spaced Data”. Ap&SS 39.2 (Feb. 1976), pp. 447–462. DOI: 10.1007/BF00648343.

[87] J. D. Scargle. “Studies in astronomical time series analysis. II. Statistical aspects of spectral analysis of unevenly spaced data.” ApJ 263 (Dec. 1982), pp. 835–853. DOI: 10.1086/160554.

[88] G. L. Israel and L. Stella. “A New Technique for the Detection of Periodic Signals in “Colored” Power Spectra”. ApJ 468 (Sept. 1996), p. 369. DOI: 10.1086/177697. arXiv: astro-ph/9603038 [astro-ph].

[89] B. A. Vaughan et al. “Searches for Millisecond Pulsations in Low-Mass X-Ray Binaries. II.” ApJ 435 (Nov. 1994), p. 362. DOI: 10.1086/174818.

[90] M. Cadelano et al. “Discovery of Three New Millisecond Pulsars in Terzan 5”. ApJ 855.2, 125 (Mar. 2018), p. 125. DOI: 10.3847/1538-4357/aaac2a. arXiv: 1801.09929 [astro-ph.HE].

[91] S. Zharikov, Yu Shibanov, and V. Komarova. *Radiation Efficiencies of the Pulsars Detected in the Optical Range*. Jan. 2005. arXiv: astro-ph/0410152. URL: http://arxiv.org/abs/astro-ph/0410152 (visited on 07/26/2023).

[92] S. Vidrih, A. Cadez, and A. Carraminana. “A stroboscopic method for phase resolved pulsar observations”. *Pulsars, AXPs and SGRs Observed with BeppoSAX and Other Observatories*. Ed. by G. Cusumano, E. Massaro, and T. Mineo. July 2003, pp. 84–90. DOI: 10.48550/arXiv.astro-ph/0402041. arXiv: astro-ph/0402041 [astro-ph].

[93] A. A. Abdo et al. “The Second Fermi Large Area Telescope Catalog of Gamma-Ray Pulsars”. ApJS 208.2, 17 (Oct. 2013), p. 17. DOI: 10.1088/0067-0049/208/2/17. arXiv: 1305.4385 [astro-ph.HE].

[94] *40 YEARS OF PULSARS: Millisecond Pulsars, Magnetars and More*. Vol. 983. American Institute of Physics Conference Series. Feb. 2008.

[95] S. Johnston and R. W. Romani. “Giant Pulses - A Brief Review”. *Young Neutron Stars and Their Environments*. Ed. by Fernando Camilo and Bryan M. Gaensler. Vol. 218. Jan. 2004, p. 315.

[96] David H. Staelin and Edward C. Reifenstein. “Pulsating Radio Sources near the Crab Nebula”. *Science* 162.3861 (Dec. 1968), pp. 1481–1483. ISSN: 0036-8075, 1095-9203. DOI: 10.1126/science.162.3861.1481. URL: https://www.science.org/doi/10.1126/science.162.3861.1481 (visited on 06/27/2023).

[97] A. Shearer et al. “Enhanced Optical Emission During Crab Giant Radio Pulses”. *Science* 301.5632 (July 2003), pp. 493–495. DOI: 10.1126/science.1084919. arXiv: astro-ph/0308271 [astro-ph].

[98] I Cognard et al. “Giant radio pulses from a millisecond pulsar”. *The Astrophysical Journal* 457.2 (1996), p. L81.

[99] Roger W Romani and Simon Johnston. “Giant pulses from the millisecond pulsar B1821–24”. *The Astrophysical Journal* 557.2 (2001), p. L93.

[100] Bhal Chandra Joshi et al. “Giant pulses in millisecond pulsars”. *Young Neutron Stars and Their Environments*. Vol. 218. 2004, p. 319.

[101] Simon Johnston and Roger W Romani. “Giant pulses from PSR B0540–69 in the large magellanic cloud”. *The Astrophysical Journal* 590.2 (2003), p. L95.

[102] T. Mineo et al. *Pulse shape and spectrum of PSR J0218+4232 observed with BeppoSAX*. 2000. arXiv: astro-ph/0001355 [astro-ph].

[103] Minjun Kim and Hongjun An. "X-ray Properties of the Pulsar PSR J0205+6449 in 3C 58". *Journal of Korean Astronomical Society* 54 (Feb. 2021), pp. 1–8. DOI: 10.5303/JKAS.2021.54.1.1.

[104] P. Moran et al. "Optical observations of PSR J0205+6449 - the next optical pulsar?" *Monthly Notices of the Royal Astronomical Society* 436.1 (Sept. 2013), pp. 401–412. DOI: 10.1093/mnras/stt1573. URL: https://doi.org/10.1093%2Fmnras%2Fstt1573.

[105] J. P. Halpern et al. "PSR J2229+6114: Discovery of an Energetic Young Pulsar in the Error Box of the EGRET Source 3EG J2227+6122". ApJ 552.2 (May 2001), pp. L125–L128. DOI: 10.1086/320347. arXiv: astro-ph/0104109 [astro-ph].

[106] Zhen Cao et al. "Ultrahigh-energy photons up to 1.4 petaelectronvolts from 12 γ-ray Galactic sources". Nature 594.7861 (June 2021), pp. 33–36. DOI: 10.1038/s41586-021-03498-z.

[107] J. W. T. Hessels et al. "Observations of PSR J2021+3651 and its X-Ray Pulsar Wind Nebula G75.2+0.1". ApJ 612.1 (Sept. 2004), pp. 389–397. DOI: 10.1086/422408. arXiv: astro-ph/0403632 [astro-ph].

[108] A. Shearer et al. "Possible pulsed optical emission from Geminga". A&A 335 (July 1998), pp. L21–L24. DOI: 10.48550/arXiv.astro-ph/9802225. arXiv: astro-ph/9802225 [astro-ph].

[109] Kaya Mori et al. "A broadband X-ray study of the Geminga pulsar with NuSTAR and XMM-Newton". *The Astrophysical Journal* 793.2 (Sept. 2014), p. 88. DOI: 10.1088/0004-637x/793/2/88. URL: https://doi.org/10.1088%2F0004-637x%2F793%2F2%2F88.

[110] F. Ambrosino et al. "Optical pulsations from a transitional millisecond pulsar". *Nature Astronomy* 1.12 (Oct. 2017), pp. 854–858. DOI: 10.1038/s41550-017-0266-2. URL: https://doi.org/10.1038%2Fs41550-017-0266-2.

[111] Thanh Nguyen. *Updated Results from VERITAS on the Crab Pulsar*. Aug. 2015. arXiv: 1508.07268 [astro-ph]. URL: http://arxiv.org/abs/1508.07268 (visited on 07/20/2023).

[112] T. Nguyen and VERITAS Collaboration. "Updated results from VERITAS on the Crab pulsar". *34th International Cosmic Ray Conference (ICRC2015)*. Vol. 34. International Cosmic Ray Conference. July 2015, 828, p. 828. DOI: 10.22323/1.236.0828. arXiv: 1508.07268 [astro-ph.HE].

[113] F. P. Nasuti et al. "Spectrophotometry of the Crab pulsar." A&A 314 (Oct. 1996), pp. 849–852.

[114] J. Aleksić et al. "OBSERVATIONS OF THE CRAB PULSAR BETWEEN 25 AND 100 GeV WITH THE MAGIC I TELESCOPE". *The Astrophysical Journal* 742.1 (Nov. 2011), p. 43. DOI: 10.1088/0004-637x/742/1/43. URL: https://doi.org/10.1088%2F0004-637x%2F742%2F1%2F43.

[115] C. Germanà et al. "Aqueye optical observations of the Crab Nebula pulsar". *Astronomy and Astrophysics* 548 (Nov. 2012), A47. DOI: 10.1051/0004-6361/201118754. URL: https://doi.org/10.1051%2F0004-6361%2F201118754.

[116] David M. Winker et al. "Overview of the CALIPSO Mission and CALIOP Data Processing Algorithms". *Journal of Atmospheric and Oceanic Technology* 26.11 (2009), pp. 2310–2323. DOI: https://doi.org/10.1175/2009JTECHA1281.1. URL: https://journals.ametsoc.org/view/journals/atot/26/11/2009jtecha1281_1.xml.

[117] Daniel Foreman-Mackey et al. "emcee: The MCMC Hammer". PASP 125.925 (Mar. 2013), p. 306. DOI: 10.1086/670067. arXiv: 1202.3665 [astro-ph.IM].

[118] D. C. Backer et al. "A millisecond pulsar". Nature 300.5893 (Dec. 1982), pp. 615–618. DOI: 10.1038/300615a0.

[119] Dan Hooper and Tim Linden. "Evidence of TeV Halos Around Millisecond Pulsars". *Physical Review D* 105.10 (May 2022), p. 103013. ISSN: 2470-0010, 2470-0029. DOI: 10.1103/PhysRevD.105.103013. arXiv: 2104.00014 [astro-ph, physics:hep-ph]. URL: http://arxiv.org/abs/2104.00014 (visited on 06/09/2023).

[120] A. Albert et al. "3HWC: The Third HAWC Catalog of Very-high-energy Gamma-Ray Sources". ApJ 905.1, 76 (Dec. 2020), p. 76. DOI: 10.3847/1538-4357/abc2d8. arXiv: 2007.08582 [astro-ph.HE].

[121] G. Maier et al. *Performance of the Cherenkov Telescope Array*. 2017. arXiv: 1709.01381 [astro-ph.IM].

[122] Daniel Mazin et al. "Status and results of the prototype LST of CTA". *Proceedings of 37th International Cosmic Ray Conference — PoS(ICRC2021)*. Sissa Medialab, July 2021. DOI: 10.22323/1.395.0872. URL: https://doi.org/10.22323%2F1.395.0872.

Appendix A

Appendix

A.1 Cumulative Significance Plots

A.1.1 Crab Scaling (Eq. 4.2)

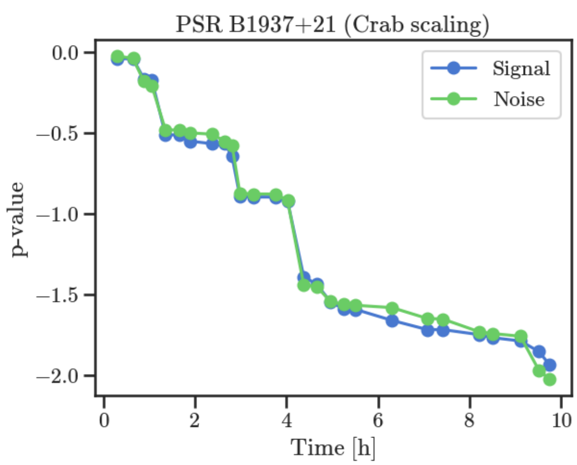

Figure A.1: Cumulative significance of PSR B1937+21.

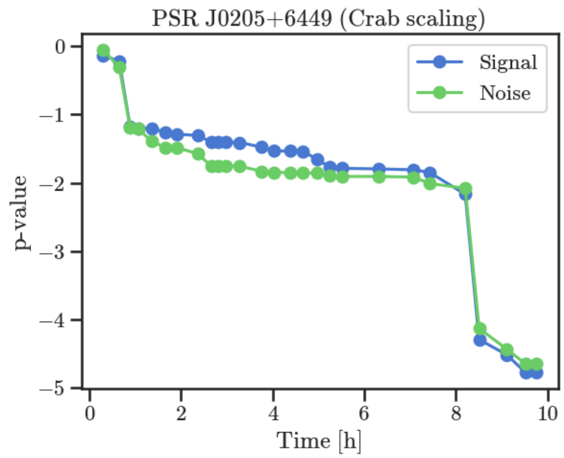

Figure A.2: Cumulative significance of PSR J0205+6449.

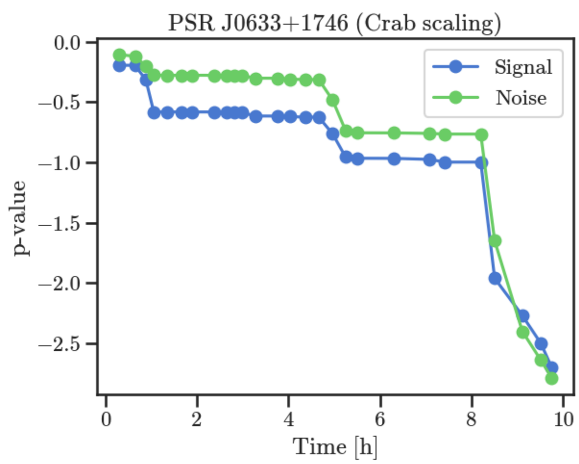

Figure A.3: Cumulative significance of PSR J0633+1746.

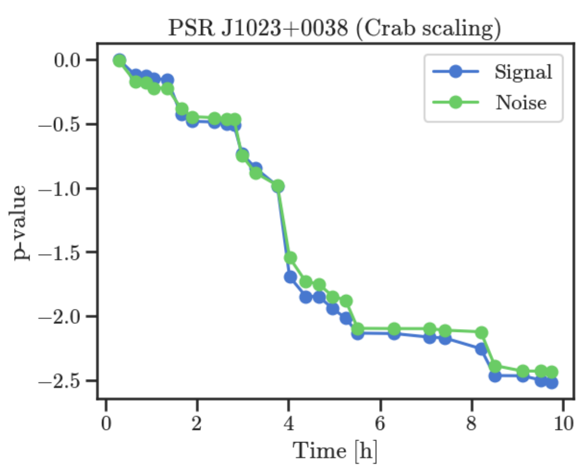

Figure A.4: Cumulative significance of PSR J0633+1746.

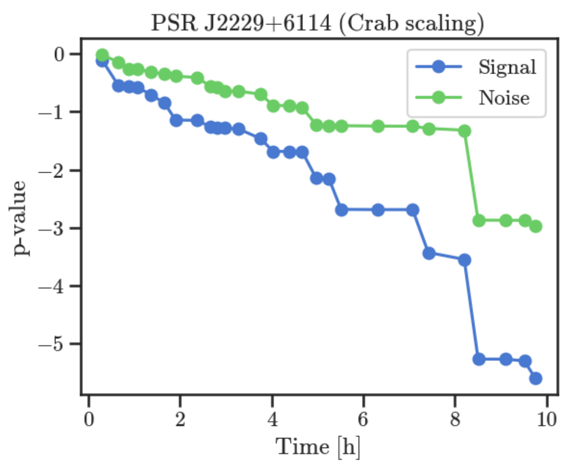

Figure A.5: Cumulative significance of PSR J2229+6114.

A.1.2 X-ray scaling (Eq. 4.5)

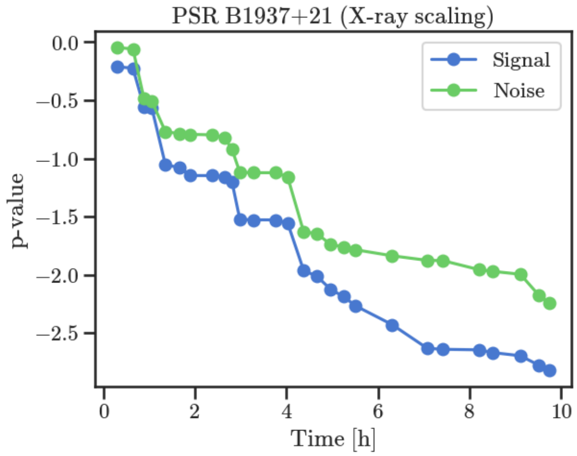

Figure A.6: Cumulative significance of PSR B1937+21.

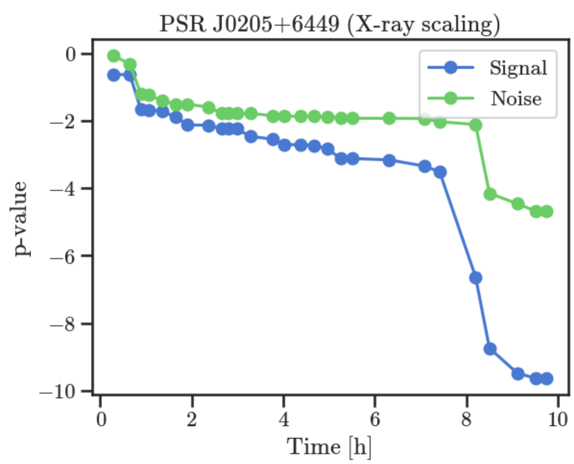

Figure A.7: Cumulative significance of J0205+6449.

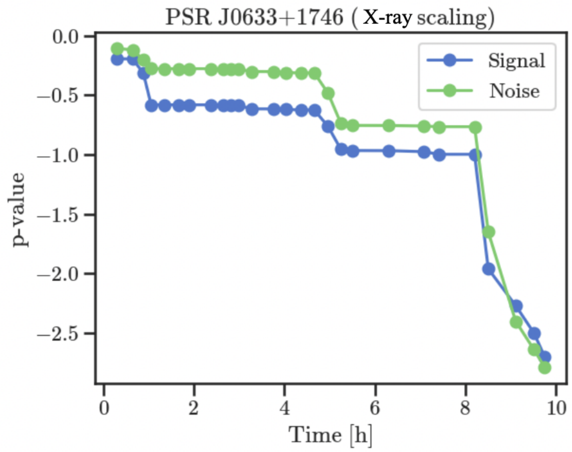

Figure A.8: Cumulative significance of PSR J0633+1746.

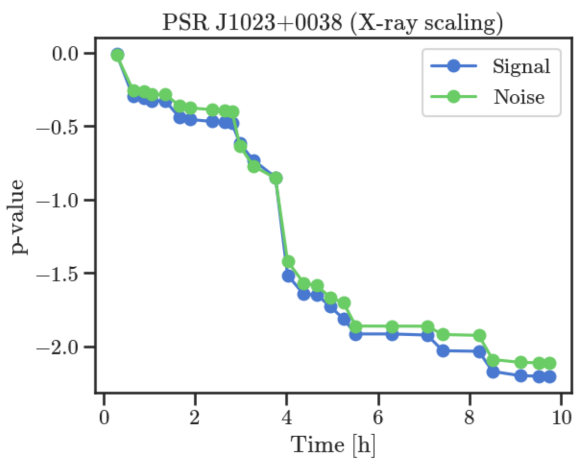

Figure A.9: Cumulative significance of PSR J1023+0038.

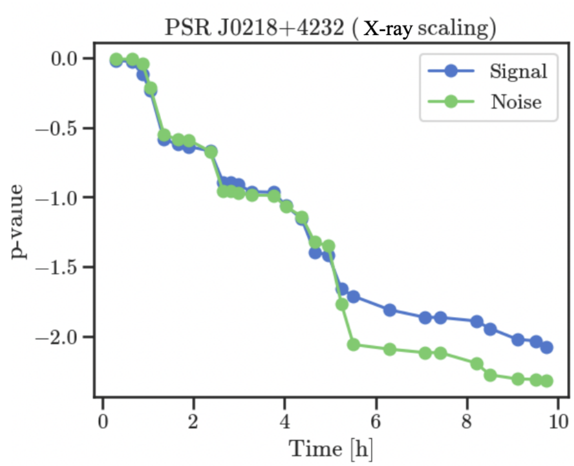

Figure A.10: Cumulative significance of PSR J0218+4232.

A.2 Extrapolated Significance Plots

A.2.1 Crab Scaling (Eq. 4.2)

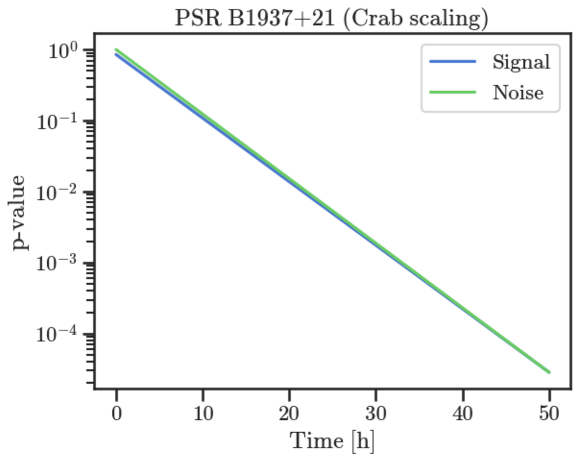

Figure A.11: Extrapolated 50h significance of PSR B1937+21.

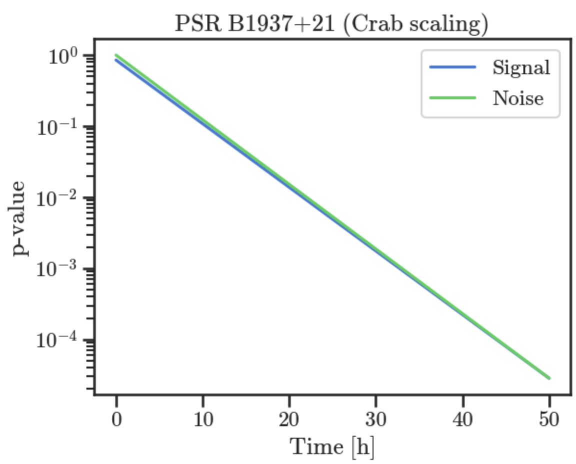

Figure A.12: Extrapolated 50h significance of PSR B1937+21.

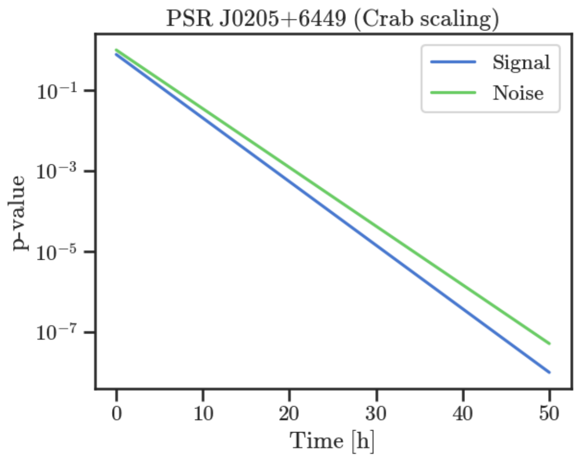

Figure A.13: Extrapolated 50h significance of PSR J0205+6449.

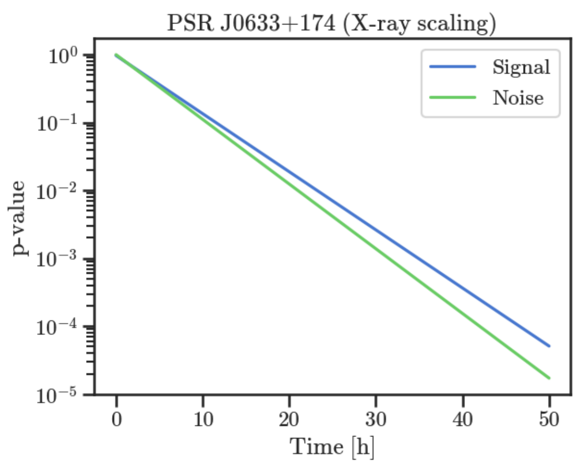

Figure A.14: Extrapolated 50h significance of PSR J0633+1746.

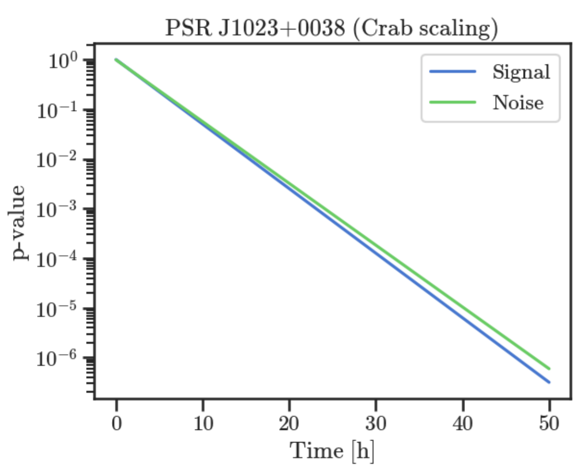

Figure A.15: Extrapolated 50h significance of PSR J1023+0038.

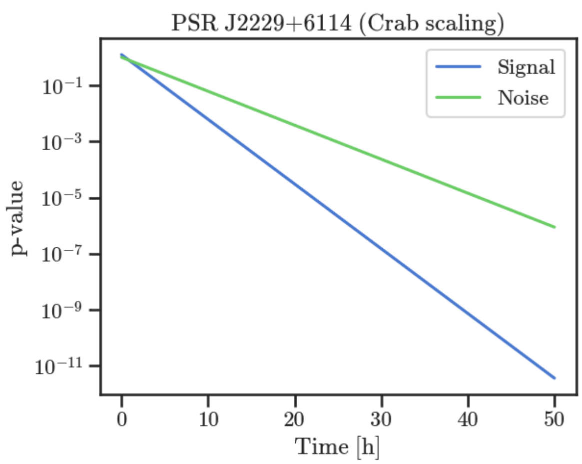

Figure A.16: Extrapolated 50h significance of PSR J2229+6114.

A.2.2 X-ray scaling (Eq. 4.5)

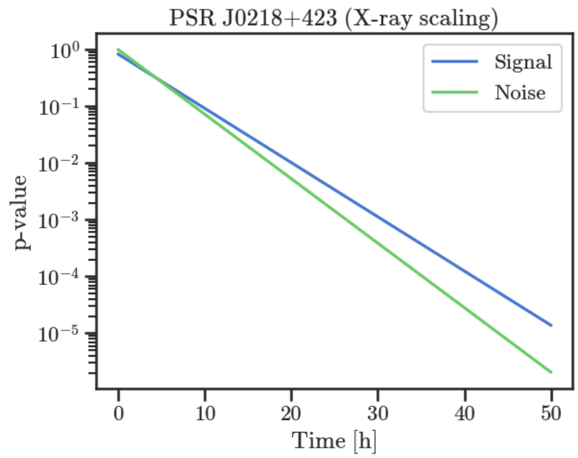

Figure A.17: Extrapolated 50h significance of PSR J0218+4232.

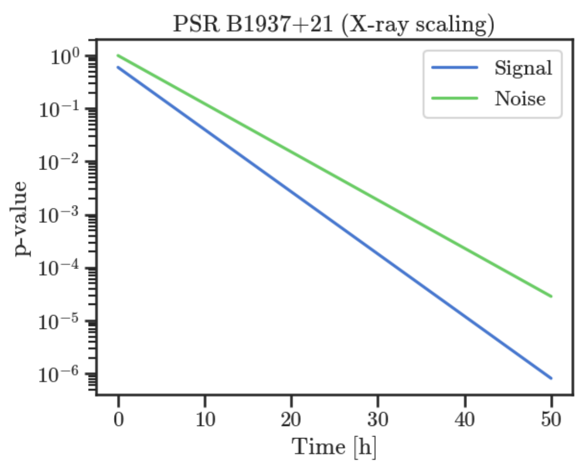

Figure A.18: Extrapolated 50h significance of PSR B1937+21.

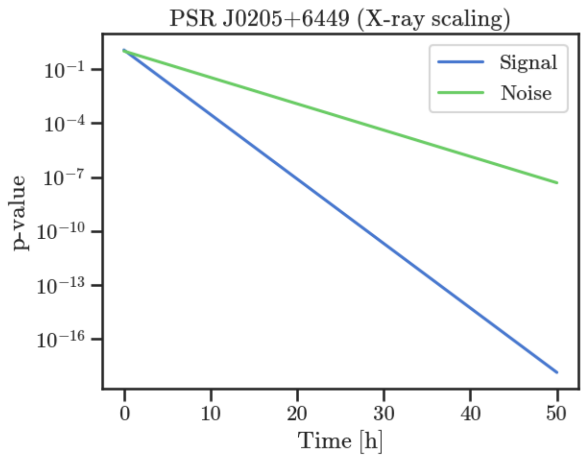

Figure A.19: Extrapolated 50h significance of PSR J0205+6449.

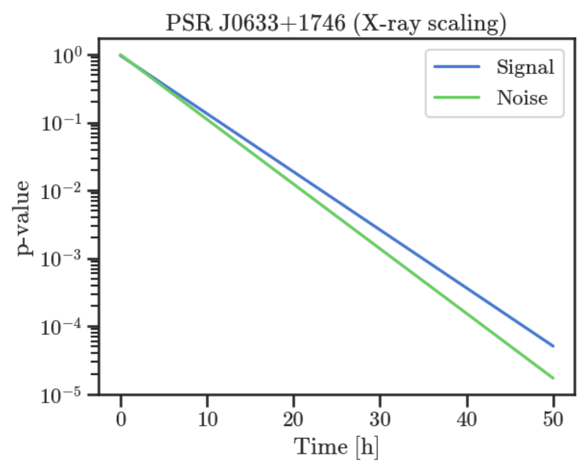

Figure A.20: Extrapolated 50h significance of PSR J0633+1746.

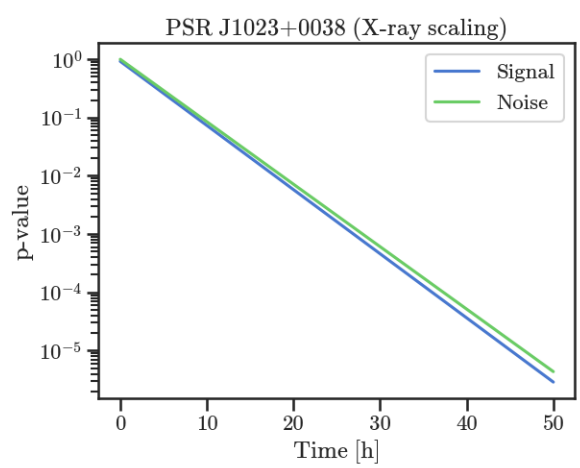

Figure A.21: Extrapolated 50h significance of PSR J1023+0038.

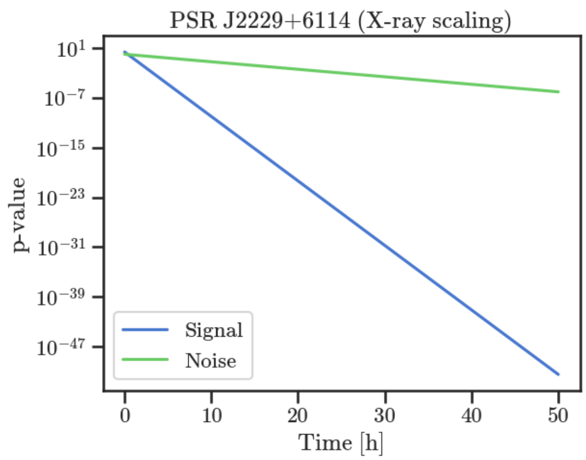

Figure A.22: Extrapolated 50h significance of PSR J2229+6114.

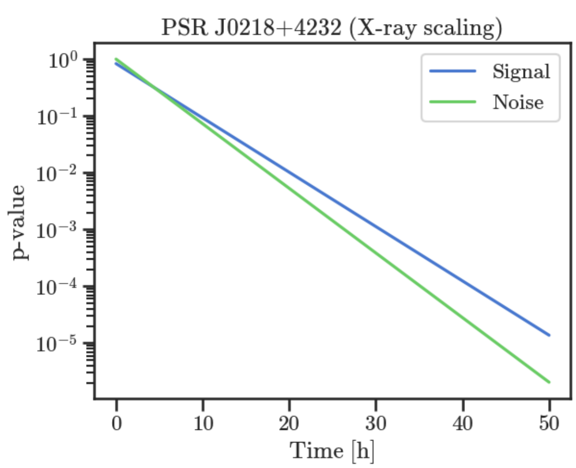

Figure A.23: Extrapolated 50h significance of PSR J0218+4232.